OSCAR D. ACOSTA LOPERA

HYDRODYNAMIC ANALYSIS OF INLAND VESSEL SELF-PROPULSION FOR CARGO TRANSPORT FOR NAVIGABILITY IN THE MAGDALENA RIVER

São Paulo
2019

OSCAR D. ACOSTA LOPERA

HYDRODYNAMIC ANALYSIS OF INLAND VESSEL SELF-PROPULSION FOR CARGO TRANSPORT FOR NAVIGABILITY IN THE MAGDALENA RIVER

Master thesis presented to the Polytechnic School of the University of São Paulo for the degree of Master of Science.

São Paulo
2019

OSCAR D. ACOSTA LOPERA

HYDRODYNAMIC ANALYSIS OF INLAND VESSEL SELF-PROPULSION FOR CARGO TRANSPORT FOR NAVIGABILITY IN THE MAGDALENA RIVER

Master thesis presented to the Polytechnic School of the University of São Paulo for the degree of Master of Science.

Research area:

Naval and Oceanic Engineering

Advisor:

Prof. Ph.D. Kazuo Nishimoto

São Paulo
2019

Autorizo a reprodução e divulgação total ou parcial deste trabalho, por qualquer meio convencional ou eletrônico, para fins de estudo e pesquisa, desde que citada a fonte.

Este exemplar foi revisado e corrigido em relação à versão original, sob responsabilidade única do autor e com a anuência de seu orientador.

São Paulo, 27 de junho de 2019

Assinatura do autor: ____________________

Assinatura do orientador: ____________________

Catalogação-na-publicação

Acosta Lopera, Oscar D.
Hydrodynamic Analysis of Inland Vessel Self-Propulsion for Cargo Transport for Navigability in The Magdalena River / O. D. Acosta Lopera -- versão corr. -- São Paulo, 2019.
134 p.

Dissertação (Mestrado) - Escola Politécnica da Universidade de São Paulo. Departamento de Engenharia Naval e Oceânica.

1.Fluvial Transport 2.Shallow water 3.Inland vessel 4.CFD 5.Magdalena river I.Universidade de São Paulo. Escola Politécnica. Departamento de Engenharia Naval e Oceânica II.t.

Dedicated to Rose Costa

ACKNOWLEDGMENTS

Acknowledgments to Technological Research Institute of the Sate of São Paulo (IPT, acronym in Portuguese) and Carlo Padovezi for send me the experimental results of the 2700 TDW inland vessel made in the 1970s. Also, to the professor Kazuo Nishimoto, general coordinator of the Numerical Offshore Tank (TPN, acronym in Portuguese) for let me use the software *STAR-CCM+* and the cluster; and for the opportunity in work as a MSc. candidate at the Polytechnic School (EP, acronym in Portuguese) of the University of São Paulo (USP). Acknowledgments to Benedito Moraes (TPN, USP) for share me the clusters' properties. Acknowledgments to the Library of Congress of the United States for send me some bibliographical resources. Acknowledgments to Guilherme Feitosa (Argonautica) and the professor Claudio Mueller (USP) for solve me the difficulties and doubts that I had during the development of my project.

Acknowledgments to COTECMAR for believe me and support on this project. Acknowledgments to Jairo H. Cabrera Tovar (my maste, UTB) for teach me with all knowledge of the naval engineer and recommend me for the opportunity in study at the EP of the USP.

Personally, acknowledgments to my family, specially to my aunt Rosario. And finally, I thanks to my friends in São Paulo, specially to Cristiana to check my English redaction on this work.

"Why do we fall? So that we can learn to pick ourselves back up"
"Our greatest glory is not in ever falling, but in rising every time we fall"

-- Bruce Wayne

RESUMO

É apresentado um estudo para determinar a resistência de uma barcaça empregada no transporte de carga que poderia operar no setor baixo do rio Magdalena. Os efeitos hidrodinâmicos de um navio em águas rasas são muito diferentes, comparados a esses efeitos em águas com profundidade infinita.

A análise hidrodinâmica é realizada numericamente usando a Dinâmica dos Fluidos Computacional (CFD, acrônimo em inglês). A solução das equações de Navier-Stokes (NS) junto com a decomposição do Reynolds (RANS, acrônimo em inglês) é aplicada para simular os efeitos viscosos e de pressão em torno de um tanque e de uma embarcação em um tanque confinado que é caracterizado pelos efeitos do fundo e das paredes. Para efeitos de turbulência, o modelo realizado k-ε é usado. O movimento da embarcação do rio provoca elevações da superfície livre que são capturadas usando o método do Volume de Fluido (VOF, acrônimo em inglês). Para a discretização do domínio de fluxo, o Método dos Volumes Finitos (FVM, acrônimo em inglês) é utilizado. O movimento dos fluidos é atualizado para cada intervalo de tempo o que permite o cálculo da resistência atuando no casco.

Os resultados da simulação numérica são comparados com dados experimentais obtidos pelo Instituto de Pesquisas Tecnológicas do Estado de São Paulo (IPT), juntamente com os métodos empíricos existentes para esse tipo de casos.

Palavras-Chave: Águas rasas, Barcaça, CFD, FVM, Modelo de turbulência k-ε, Resistencia, RANS, Rio Magdalena, VOF.

ABSTRACT

The subject of this study is the determination of the resistance of an inland vessel engaged in cargo transport in the lower course of the Magdalena River, considering that the hydrodynamic effects in shallow water navigation are very different compared to the effects in deep water navigation.

The hydrodynamic analysis is realized numerically using Computational Fluid Dynamics (CFD). The Reynolds-Averaging Navier-Stokes equation (RANS) solver is applied to simulate viscous and pressure effects around a tank and a hull in confined tank considering the wall bottom and side effects in shallow water navigation. For turbulence effects, realizable k-ε model is used. The motion of the vessel causes elevations of the free surface, in which, is captured using the Volume of Fluid method (VOF). For discretization of flow domain, the Finite Volume Method (FVM) is applied. The motion of the fluids is updated for each time step that allows the calculation of the resistance acting on the hull.

The numerical simulation results are compared with experimental data obtained by the Technological Research Institute of the State of São Paulo (IPT, acronym in Portuguese) together with the existing empirical methods for this type of cases.

Keywords: CFD, Free surface flow, FVM, Inland vessel, k-ε turbulence model, Magdalena River, RANS, Resistance, Restricted waterways, VOF.

LIST OF FIGURES

LIST OF TABLES

LIST OF SYMBOLS

Latin symbols

Symbol	Term
$\mathbf{A}$	Surface area vector
$\mathbf{A}_f$	Area of the cell face
A_c	Sectional area of the channel or river
A_{ims}	Immersed midship area of the ship
A_0	Function (equation 3.9)
A_1	Function (equation 3.10)
$\mathbf{a}$	Any point on the free surface
B	Beam of the vessel
B_c	Width of the channel or river
B_1	Function (equation 3.13)
B_2	Function (equation 3.14)
B_3	Function (equation 3.15)
$\mathbf{b}$	Position of vector of the face centroid
C_a	Correlation allowance coefficient
C_f	Frictional resistance coefficient
C_o	Courant number
C_r	Residuary resistance coefficient
C_t	Total resistance coefficient
C_1	Function (equation 4.40)
$C_{1\varepsilon}$	k-ε model constant
C_μ	k-ε model constant
c	Critical velocity
d_m	Dimensional length of the model
d_p	Dimensional length of the prototype
E	Center of the coordinates adjacent to east cell in a control volume
E	Empirical constant
E_r	Relative error
E_1	Function (equation 3.8)
e	Point of the east center face of a control volume
e_a^{21}	Approximate relative error for medium-fine grid mesh used for GCI
e_a^{32}	Approximate relative error for coarse-medium grid mesh used for GCI
e_{ext}^{21}	Extrapolate relative error used for for medium-fine grid mesh GCI
e_{ext}^{32}	Extrapolate relative error used for for coarse-medium grid mesh GCI
F_b	Body force
F_{CFD}	Force of the numerical results
F_i	Components of the force vector
F_m	Force of the experimental test results
F_s	Surface force
Fr_h	Depth Froude number
Fr_L	Length Froude number

Symbol	**Term**
G	Function (equation 3.12)
GCI^{21}_{fine}	Fine-grid convergence index equation
g	Gravity
$\overrightarrow{g}$	Gravity vector
H	Function (equation 3.16)
h	Local depth
$\mathbf{I}$	Identity matrix
I	Turbulence intensity
K	Function (equation 3.17)
k	Turbulent Kinetic Energy
k_{in}	Turbulent Kinetic Energy at inlet boundary condition
k_{out}	Turbulent Kinetic Energy at outlet boundary condition
k_{sym}	Turbulent Kinetic Energy at symmetry boundary condition
k_{wall}	Turbulent Kinetic Energy at wall boundary condition
L_{WL}	Length of the vessel in waterline
L_{mod}	Length of the inland vessel model
M	Function (equation 3.18)
$\dot{m}$	Mass flow rate
N	Center of the coordinates adjacent to north cell in a control volume
N_i	Mesh number
N_{faces}	Number of faces enclosing the bcell
N_{fluids}	Number of fluids
N_1	Function (equation 3.11)
$\mathbf{n}$	Normal vector
n	Point of the north center face of a control volume
n_j	Components of the normal vector
O	Center of the cell in a control volume
P	Mean pressure
$\overline{P}$	Time averaged mean pressure
P_k	Generation of TKE
$P_{k-\text{wall}}$	Generation of TKE on the wall boundary condition
p	Pressure
p_{in}	Pressure on inlet boundary condition
p_{out}	Pressure on outlet boundary condition
p_0	Pressure with the gradient due to gravitational force
p^*	Balanced pressure
p'	Fluctuating pressure
$\overline{p'}$	Time averaged fluctuating pressure
q	Designation of the fluid for α
q_s	Wetted girth of the hull
R_f	Frictional resistance
R_p	Pressure resistance
R_r	Residuary resistance
R_t	Total resistance
Re	Reynolds number
Re_L	Reynolds number of the inland vessel model
Re_t	Turbulent Reynolds number

Symbol	Term
Rw	Wave-making resistance
Rw_d	Wave-making resistance in deep water
Rw_h	Wave-making resistance in depth water
r_h	Hydraulic radius
r_k	Refinement ratio used for GCI
S	Center of the coordinates adjacent to south cell in a control volume
S_1	Function (equation 4.40)
S_{ij}	Strain-rate tensor
S_k	User-defined source term
S_{mat}	Material surface
S_{ws}	Wetted surface area the of the vessel
S_ε	User-defined source term
S_φ	Source of φ
s	Point of the south center face of a control volume
T	Draft of the vessel
T_s	Characteristic time scale
t	Time
u_Q^+	Dimensionless velocity from the centroid of the wall-adjacent cell to the wall B
u_Q^*	Dimensionless velocity for k-ε turbulence model
U_i	Mean velocity
U_Q	Mean velocity of the fluid at the wall-adjacent cell centroid Q
$\mathbf{U}_{\text{in}}$	Mean velocity vector at inlet boundary condition
$\mathbf{U}_{\text{out}}$	Mean velocity vector at outlet boundary condition
$\mathbf{U}_{\text{sym}}$	Mean velocity vector at symmetry boundary condition
$\mathbf{U}_{\text{wall}}$	Mean velocity vector at wall boundary condition
$\overline{U_i}$	Time averaged mean velocity
$\mathbf{u}$	Flow velocity in vector notation
$\mathbf{u}_f$	Flow velocity vector field through the face cell
u_i	Flow velocity in tensor notation
u'_i	Fluctuating velocity
$\overline{u'_i}$	Time averaged fluctuating velocity
u_τ	Friction or shear velocity
V	Volume
$\dot{V}$	Volume flow rate
V_q	Volume of the designed fluid
W	Center of the coordinates adjacent to west cell in a control volume
w	Point of the west center face of a control volume
$\mathbf{x}$	Position vector in tensor notation
x_i	Position vector in vector notation
y	Distance of the boundary thickness
$y+$	Dimensionless distance on the wall
y_Q	Distance from the centroid of the wall-adjacent cell to the wall B
y_Q^+	Dimensionless distance from the centroid of the wall-adjacent cell to the wall B
y_Q^*	Dimensionless distance from the centroid of the wall-adjacent cell to the wall B for k-ε turbulence model

Greek symbols

Symbol	Term
α	Phase of the fluid used for VOF
α^*	Coefficient determined by Karpov (1946)
α^{**}	Coefficient determined by Karpov (1946)
β	Midship section area coefficient of the vessel
$\mathit{\Gamma}_\varphi$	Diffusion coefficient for φ
Δx	Length interval
Δt	Time step
δ	Kronecker delta
δC	Velocity between υ_∞ and υ_I
δC_r	Residuary resistance coefficient correction
$\delta\upsilon$	Velocity loss
$\delta\upsilon_p$	Velocity between υ_h and υ_I
∇	Nabla operator
$\nabla\cdot$	Divergence
∇^2	Laplace operator
ε	Dissipation rate
ε_{in}	Dissipation rate at inlet boundary condition
ε_{out}	Dissipation rate at outlet boundary condition
ε_{sym}	Dissipation rate at symmetry boundary condition
$\varepsilon_{\text{wall}}$	Dissipation rate at wall boundary condition
ε_Q	Dissipation rate at centroid wall-adjacent Q at wall boundary condition
η	Function (equation 4.40)
θ	Wave propagation angle
ι_{21}	Solution changes for medium-fine meshes applied to CGI
ι_{32}	Solution changes for coarse-medium meshes applied to CGI
κ	von Kármán constant
Λ	Displacement of the vessel
λ	Wave length
μ	Dynamic (shear) viscosity
μ_t	Dynamic turbulent viscosity
ν	Kinematic viscosity
ρ	Density
ρ_0	Reference density
$-\rho\overline{u_i u_j}$	Reynolds stress tensor
σ	Quantity (normal) stress
σ_k	k-ε model constant
σ_ε	k-ε model constant
τ_{ij}	Quantity (shear) stress
τ_{wall}	Quantity (shear) stress at the wall
Υ	Apparent order used for GCI
υ	Velocity of the vessel
υ_1	Effective velocity 1
υ_2	Effective velocity 2

Symbol	Term
υ_∞	Velocity of the vessel in deep water
υ_h	Velocity of vessel in shallow or depth water
υ_I	Intermediate velocity of vessel
Φ	Prismatic coefficient of the vessel
ϕ_1	Solution for fine mesh applied in GCI
ϕ_2	Solution for medium mesh applied in GCI
ϕ_3	Solution for coarse mesh applied in GCI
ϕ_{ext}	Extrapolated value used for GCI
φ	Scalar quantity
φ_f	Value of scalar quantity convected through face

Abbreviations

Acronym	Name
AIAA	American Institute of Aeronautics and Astronautics
ANSYS	Analysis System
ASME	American Society of Mechanical Engineers
BSL	Baseline for k-ω
CAD	Computer-Aided Design
CD-adapco	Computational Dynamics-Analysis & Design Application Company Ltd.
CFD	Computational Fluid Dynamics
CNR (in French)	Rhone National Company
Cormagdalena (in Spanish)	Magdalena Great River Corporation
DTMB	David Taylor Model Basin
DTU (in Danish)	Technical University of Denmark
EDUSP (in Portuguese)	Publisher of the University of São Paulo
EP (in Portuguese)	The Polytechnic School
FDM	Finite Difference Method
FEM	Finite Element Method
FVM	Finite Volume Method
GCI	Grid Convergence Index
GDP	Gross Domestic Product
HRN	High Reynolds Number
ICCM	International Conference on Computational Methods
IHTC	International Heat Transfer Conference
IITK	Indian Institute of Technology Kanpur
IPT (in Portuguese)	Technological Research Institute of the State of São Paulo
ITTC	International Towing Tank Conference
LRN	Low Reynolds Number
MAC	Marker-and-cell method
MASHCON (In German)	International Conference on Ship Maneuvering in Shallow and Confined Water with Special Focus on Ship Bottom Interaction
MATLAB	Matrix Laboratory

Acronym	**Name**
NS	Navier-Stokes
PDE	Partial Differential Equations
PIANC	Permanent International Association of Navigation Congresses
RANS or RANSE	Reynolds Averaging Navier-Stokes equation
RE	Richardson Extrapolation
RNG	Re-Normalization Group method for k-ε
SIMPLE	Semi-Implicit Method for Pressure Linked Equations
SNAME	Society of Naval Architects and Marine Engineers
SST	Shear-Stress Transport for k-ω
TDR	Turbulent Dissipation Rate
TKE	Turbulence Kinetic Energy
TPN (in Portuguese)	Numerical Offshore Tank
USP (in Portuguese)	The University of São Paulo
UTB (in Spanish)	The Technological of Bolivar University
UTC (in French)	University of Technology of Compiègne
VOF	Volume of Fluid

CONTENTS

1 INTRODUCTION

> *"A universal constant has been the development of people, civilizations and diverse cultures around the main river, which dispenses gift and natural resources, provides identity, offering its landscape, becomes a witness to its history and is a generator of life"*, Bernal Duffo (2013).

At the time of the European conquest of the Americas, the Spanish arrived at the Colombian territory. The Magdalena river was discovered and named by Rodrigo de Bastidas at the beginning of 16th century (specifically on April 1st in 1501) and gained great importance as a main access route. During the colonization period, the river served as a single route between Santa Fé de Bogotá (actually Bogotá) and the port of Cartagena (Bernal Duffo, 2013).

During the independence period, the patriotic armies used the river to dominate the Spanish colony. Gabriel Garcia Marquez described these events in his historical novel *The General in His Labyrinth*.

As far as the logistics are concerned, the fluvial transport was used from the colonial period until the middle of 19th century for the transport of commercial products which were transported in keel-boats. In 1822, steamboats were introduced, and the harvest of tobacco in 1850s made the river transport more profitable. Nevertheless in 20th century, the commercial activities of the river for the transport of commercial goods started to decline due to the air services, the railway transport and mainly, the road transportation (Encyclopædia Britannica, 2015d).

With the aim of increasing the activities of the river, the Colombian Constitution of 1991 created the Magdalena Grand River Corporation (Cormagdalena, acronym in Spanish) and since then, the fluvial transport has been recovering due to projects developed or being developed that imply the navigability of the river that includes, the construction of ports, dredging works and the maintenance of the river. Nowadays, the cargoes are transported in convoys, each of which consists of a tugboat and a maximum of six barges organized in series and/or in parallel.

In 2017, 3.67 million tons of a large variety of goods, including hydrocarbons and dry cargoes such as coal and cement, were mobilized by the river. This signify an increase of 68.5% compared to the numbers of the previous year (Ministry of Transport - Colombia, 2018).

There are different types of inland vessel (Bureau Voorlichting Binnenvaart, n.d.): dry-cargo carriers, well barges, tank vessels, push/tugboats and ro-ro.

The Magdalena River is the most important in the country with an extension of 1,497 km and its birthplace is located in the *Páramo de las Papas* (placed in the Andes mountain range). This river is divided in three courses: upper, middle and lower (Figure 1.1), crossing 128 municipalities and 11 departments. The river receives the affluents of the San Jorge, Cesar and Cauca rivers, increasing its flow. Finally, the river mouths in the Caribbean Sea and close to Barranquilla city (ACOSTA-LOPERA; CABRERA-TOVAR, 2014; Encyclopædia Britannica, 2015d). The area under the influence of the Magdalena river is responsible for 80% of GDP of the country, 70% of the hydraulic energy, 95% of the thermoelectricity, 70% of agricultural production, 50% of freshwater fishing (Castro Pinzón, 2017).

Compared to other countries, the Netherlands is a pioneer in this type of transport, since its canal system is based on large natural rivers. For example, to transport a cargo of 16,000 tons, 660 trucks are needed for road transport, while only one inland barge can transport the total of that cargo and the Dutch operators take advantage of these numbers as the riverboats under the Dutch flag that is represented around 50% of the entire Western European fleet. Furthermore, the importance of the rivers in Netherlands is obvious as 6,000 km of a total of 24,709 km of the European waterways are Dutch, where 500 km are main routes (Bureau Voorlichting Binnenvaart, 2011; ACOSTA-LOPERA; CABRERA-TOVAR, 2014; Encyclopædia Britannica, 2015a).

The fluid mechanics allow the study of the fluids at rest (*stationary*) and, mainly, in motion (*dynamic*). The last term is called *Fluid Dynamics*. The fundamental *mathematical* equations describe the physical characteristics of the fluid motion. The solution of the math equations is converted in a high-level computer programming language into computer programs applying numerical methods and is called *computer science*. These disciplines integrate the branch of the *Computational Fluid Dynamics* (CFD), illustrated in the Figure 1.2 (TU; YEOH; LIU, 2008).

The numerical methods imply the comparison and the validation of the experimen-

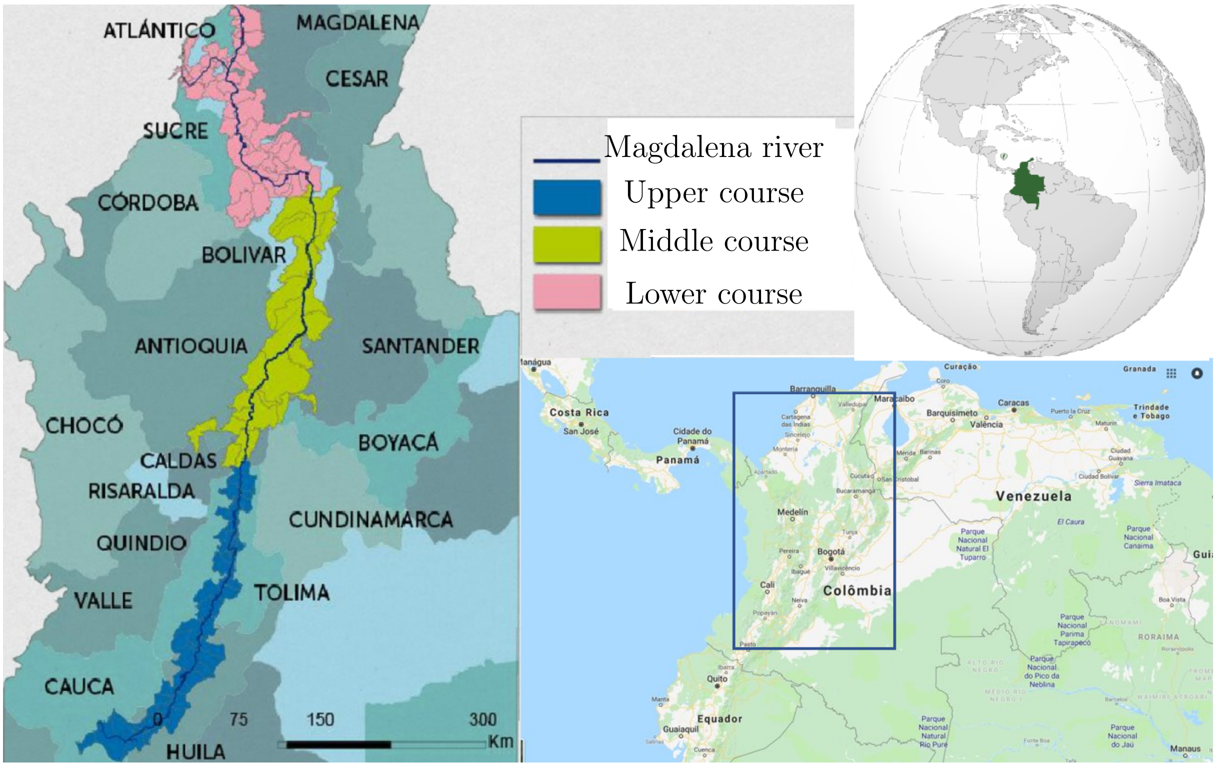

Figure 1.1: Hydrography of the Magdalena River, divided in upper (blue), middle (yellow) and lower (pink) courses. Source: Acosta-Lopera and Cabrera-Tovar (2014), Google, Wikipedia.

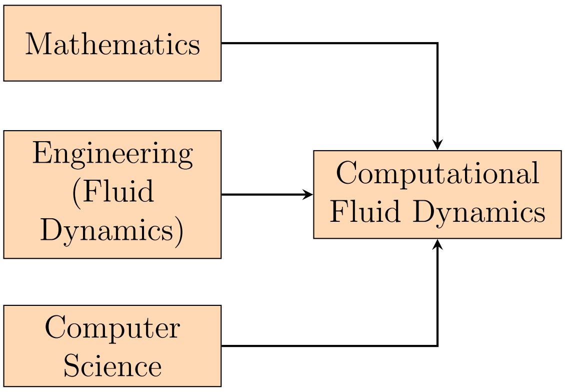

Figure 1.2: Different disciplines involved in CFD. Source: Tu, Yeoh and Liu (2008).

tal test and theoretical analysis, indicated in the Figure 1.3. The theoretical analysis allows the designer predicts the behavior for a case. The experimental test simulates the environmental and physical conditions in reduced scale. In the Table 1.1, extracted from Pletcher, Tannehill and Anderson (2013), the strategies to solve problems of fluid mechanics are compared. Over the years, the speed of computer processing has been increasing contrary to computational costs, illustrated in the Figure 1.4. This makes them more efficient, therefore, has generated interest for the application in CFD. The computer performance is measured in Gflop/s.

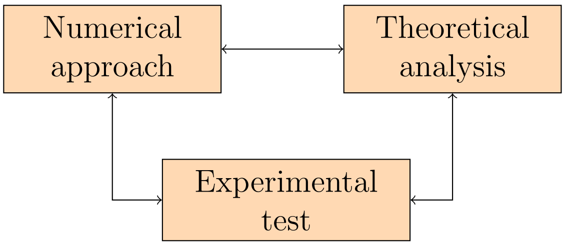

Figure 1.3: CFD complement the theoretical analysis and experimental test. Source: Tu, Yeoh and Liu (2008), Fortuna (2012).

Approach	**Advantages**	**Disadvantage**
Experimental	• Capable of being most realistic	• Equipment required • Scaling problems • Tunnel corrections • Measurement difficulties • Operating cost
Theoretical (analytic)	• Simple basic general information, which is usually in formula form	• Restricted to simple geometry and physics • Usually restricted to linear problems
Computational	• No restriction to linearity • Complicated physics can be treated • Time evolution of flow can be obtained	• Truncation errors • Boundary condition problems • Computer cost

Table 1.1: Comparison of approaches. Source: Fortuna (2012), Pletcher, Tannehill and Anderson (2013).

Despite the advantages and disadvantages offered by CFD, it still cannot resolve a lot of problems, i.e., turbulent flow cases. When the Navier-Stokes equations are used numerically, the turbulent behavior is not represented directly, therefore the need for the adoption of turbulent models from the original equations. However, there are exist turbulence models that allow resolve this type of flows.

1.1 Presentation of the problem

The need to improve efficiency of cargo transport sector had motivated the increase in the number of self-propelled vessels in the main river of the country, allowing the direct access of companies located inland to the main ports of the Colombian northern regions.

Despite the economic advantages of cargo transport by river for the national econ-

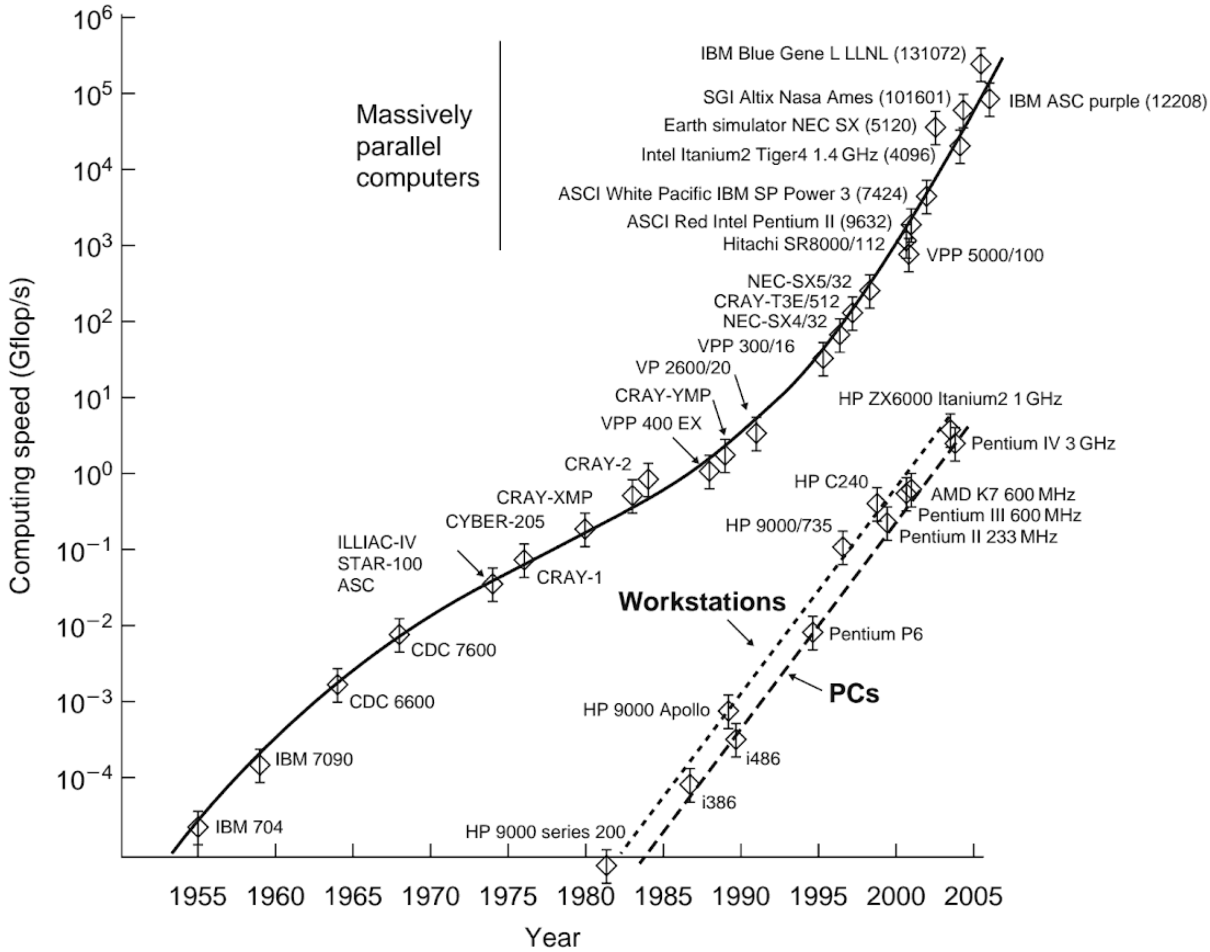

Figure 1.4: Evolution of computer performance from the 1950s. Source: Hirsch (2007).

omy, resulted from the reduction of freight rates and costs of exportation, the road transportation remains the main transport system in Colombia where factors, such as poor conservation and the weather conditions makes this transport mode very expensive and inefficient.

The elaboration of inland vessel projects ends up being a local regional or national problem since it depends on the conditions in the waterway, the route and the market in which the vessel will operate, as well as, other factors such as mission, cargo capacity and autonomy. The physical characteristics of the river and the aspects of the shallow water effects (as draft and beam restrictions, crossing ships in restricted spaces, radius of curvature of the river, locks) are important for the execution of the project. In this project, the type of inland vessel will be designed for dry-cargo carrier, well barge and tank vessel.

1.2 Objectives

The objective of this work is the study of the resistance of a 2700 TDW inland vessel self-propelled by CFD numerical simulation and the validation and comparison of the numerical results with the existing empirical formulas and the experimental test results.

The following specific objectives are proposed during development of this objective:

- Understanding of the phenomena involving fluid flow along the inland vessel hull in shallow waters;
- Modeling of the 2700 TDW inland vessel hull using the CAD software *FREE!Ship* and *Rhinoceros*;
- Evaluation of the hull resistance using empirical formulas;
- Numerical simulation of the 2700 TDW inland vessel hull using CFD software *STAR-CCM+*.
- Application of the grid convergence criteria for the choosing the number of elements that it will simulate the resistance and calculation of the properties of the inland vessel.

The study is divided in 6 chapters:

- Chapter 1 is the introduction of this study, where the presentation of the problem and the objectives are presented.
- Chapter 2 presents the state of art, including important references.
- Chapter 3 explains the empirical method for the estimation of the inland vessel resistance. For this purpose, the empirical formulations for the velocity loss calculation of the vessel in shallow water using Schlichting, Landweber, Lackenby for large rivers, as well as, the empirical formulations for middle rivers, where the effective velocities calculation applying the Karpov's diagrams and the correction of wall effect by Artjushkov are used.
- The resistance estimation applying CFD is the main topic of the chapters 4 and 5, where the equations for the numerical calculation, the procedure and the methodology, applied to inland vessels, are explained. Finally, the numerical results are compared to the experimental results for validation purposes.

- Chapter 6 presents the conclusions and the future work of the project. The next chapter, the references consulted are listed. The appendices present the calculations concerning the shallow water effects and others results, including the experimental results, and codes used in this study.

2 BIBLIOGRAPHIC REVIEW

The calculation of the resistance is based on Froude Hypothesis that is composed by frictional and residual resistances, where are expressed by the frictional and residual coefficients, wetted surface of the hull, velocity of the vessel and water density. ITTC (1957) established an equation for the frictional resistance coefficient. Guldhammer and Harvald (1974) created diagrams for the calculation of the residuary resistance coefficient. Georgakaki and Sorenson (2004) demonstrated that the resistance coefficient can be extrapolated providing reasonable results.

Considering the effects of shallow waters, Molland, Turnock and Hudson (2011) explained the wave generating phenomena for the resistance calculation. Latorre, Luthra and Tang (1982) presented the empirical methods of study for inland vessels applied to European and American vessels. ITTC (1987) considered some typical parameters to estimate the waterway restriction in shallow water. Pompée (2015) reviewed many empirical methods to determine the resistance of the ship depending on the type of vessel (pushed convoy or self-propelled), as well as, the physical conditions of a river (small, medium and large). In this study is explained only empirical formulations for medium and large rivers.

For large rivers and sea access channels, Schlichting (1934) presented the analysis of shallow water effects through experimental test and theoretical considerations, without influence of walls in a towing tank. Landweber (1939) improved this work, proposing the hydraulic radius. Lackenby (1963) simplified the semi-empirical formula of the velocity loss proposed by Schlichting.

In case of medium rivers, the effects of the shallow water are different. Karpov (1946) interpreters these phenomena with effective velocities for frictional and residual resistances that can be determined through two diagrams proposed by him. Artjushkov (1968) improved this work correcting the wall effects. Georgakaki and Sorenson (2004) demonstrated that these diagrams and the correction of the wall effects would be extrapolated, and they proposed equations for the approximation of these parameters.

For small rivers, the calculation of the inland vessel resistance is associated with the existence of a limited velocity in restricted waterways that cannot exceed, where could be caused by a steep ship resistance rise. Schijf (1949) studied this limit velocity that corresponds for lower critical velocity (also called subcritical velocity). Pompée (2015) made the analytical theories for confined waters using two methods: energy method by Schijf (1949, 1953); and quantity of movement methods by Bouwmeester *et al.* (1977) and CNR (SAVEY, 1977; TENAUD, 1977; POMMIER; SELMI, 1981). These analytical theories are complemented for the Schlichting's formulation.

The numerical calculation of the hydrodynamic flow of the inland vessel was based on references that influenced this study. From the conservation of mass to the conservation of momentum, the Navier-Stokes (NS) equations are the basis of the description of fluid motion. Euler (1755) initiated this work for incompressible fluids and non-friction flows, Navier (1822) analyzed the friction effects for viscous fluids and Stokes (1845) improved this work completing the solution.

Reynolds (1895) introduced the time-averaging of the flow for turbulent effects, defining the decomposition of a mean and fluctuating parts of a variable. This is applied to the NS equations and is called Reynolds-Averaging Navier-Stokes equations (RANS). The choice of the turbulence model is necessary. Launder and Spalding (1972) were the first to introduce the standard k-ε model. This model was refined and is called RNG (Re-Normalization Group methods) k-ε model, and it was developed by Yakhot *et al.* (1992). Later, Shih *et al.* (1995) improved the turbulence model and is called Realizable k-ε. Wilcox (1988) published another turbulent model denominated standard k-ω. To improve k-ω model, Menter (1993) developed the baseline (BSL, also called BSL k-ω model) which was later refined for the transport of the turbulence shear stress and is called Shear Stress Transport (SST) k-ω model.

Noh and Woodward (1976), and Hirt and Nichols (1981) developed the Volume of Fluid method (VOF) to track and locate the free-surface. This method is based on Marker-and-cell method (MAC).

The interpolation of the convection term is used in the transport equation applied to Finite Volume Method (FVM). Courant, Isaacson and Rees (1952), and independently, Gentry, Martin and Daly (1966); Barakat and Clark (1966); and Runchal and Wolfshtein (1969) introduced the 1st order upwind scheme. Another type of interpolation is the 2nd order upwind scheme, started by Warming and Beam (1976), and Hodge, Stone and Miller (1979) for finite difference discretization.

Patankar and Spalding (1972) introduced the iterative method called the The Semi-Implicit Method for Pressure Linked Equations (SIMPLE) algorithm to resolve the linear pressure-velocity couple.

2.1 Important references

The following references are of high importance in this study.

2.1.1 Celik *et al.* (2008)

Their work resulted in the development of the Grid Convergence Index (GCI) that is used in the estimation and report of uncertainty results in CFD applications. The method is based on the Richardson (1910) Extrapolation (RE) and is only applied to unstructured volume domain. The authors justified that, if the user chooses to use it, this method shall not be questioned. On the other hand, if the user chooses another method, this method shall be judged in the review process. However, the authors do not desire to discourage further development of new methods. This method is simple, justified and accepted, and is used in this study for the validation of the simulation results.

2.1.2 ITTC (2014)

The ITTC creates a guideline, comprising of recommendations and practices regarding the applications of CFD methods that is divided in three steps: pre-processing, computation, and post-processing. The geometry of the hull, the volume domain and the computational grid are defined during the pre-processing step. At computational step, the governing equations to be solved are chosen. The visualization, analysis, verification and validation of the results belong to the post-processing step.

In this study, some of the values recommended in the guideline are adopted and applied to the equations. One of these recommended values is the wall $y+$, applied on the wall of the hull for the creation of the boundary layer in the grid mesh, which the ITTC provides a range of possible options, among which the user shall choose the specific for the purpose of the study. Later, the distance y of the first layer is calculated. The ITTC (1957) established the formulation for the frictional resistance coefficient that is explained in the next chapter.

According to ITTC (2014), this is important because the value of wall $y+$ should be checked *a posteriori* once the solution is obtained. In this project, the wall $y+$ is simulated for the wall hull surface and the wall bottom plane in the computational domain.

2.1.3 Ji *et al.* (2012)

Their work is the study of prediction of the relationship between the geometrical and the kinematic parameters of the convoy and the amplitude of ship generated waves in restricted waterways. The authors used numerical simulations, solving the 3-D Navier-Stokes, along with the standard k-ε for turbulent.

In this paper, the calculation of the grid size in x direction is defined and the transversal wave length λ is estimated. Once is done, the value of λ is divided by 10 points, as the authors recommend, obtaining the grid size.

2.1.4 Linde *et al.* (2017)

Their work consists in the evaluation of the ship resistance in restricted waterways with effects of ship sinkage and trim. The RANS solver coupled with a quasi-Newton approach is used to find the equilibrium position and the calculation of the ship sinkage. The numerical simulation results are validated with towing tank tests and some empirical models.

In this study, the GCI method for grid convergence will be used with a constant refinement ratio

$$r_k = \sqrt{2}. \tag{2.1}$$

2.1.5 Liu *et al.* (2017)

The authors evaluated the inland vessel resistance in confined waters. The effect of squat is analyzed. They used the RANS equations to simulate the viscous flow around the hull in a confined tank characterized by shallow sea bottom and close side walls.

In this study, computational domain is adopted, as illustrated in the Figure 2.1. Dimensions extend by $1.5L_{\mathrm{WL}}$ from the bow to the inlet plane, $3.5L_{\mathrm{WL}}$ from stern to the outlet plane and $0.33L_{\mathrm{WL}}$ from the free surface to the top plane. Additionally, the meshing volume is configured and modified, as shown in Figure 2.2. The grid mesh in the vicinity of the free surface, hull, the tank bottom and the banks are refined. The prism layer is used at the bottom boundary condition, with wall $y+$ larger than 30; at the hull surface, wall $y+$ is smaller than 1 in order to obtain a more precise flow field simulation near the vessel.

Some configurations of the boundary conditions are adopted. The velocity inlet is set on the inlet and top plane. The pressure outlet is set on the outlet plane. The symmetry condition is set on the symmetry plane. The wall condition is set on the rest of the planes, including the hull.

For the estimation of the numerical error and uncertainty about the results following the grid discretization, the GCI is only applied to grid convergence with a constant refinement ration defined in the equation (2.1).

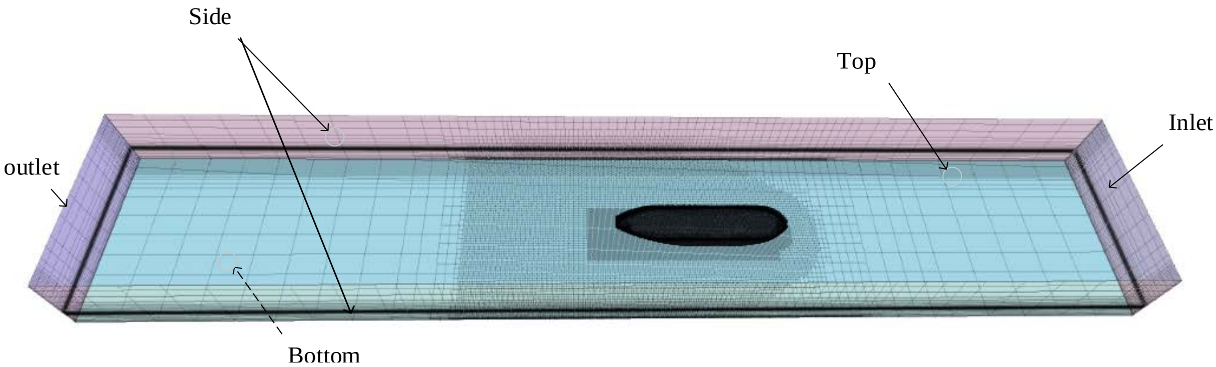

Figure 2.1: Overview of computational domain. Source: Liu *et al.* (2017).

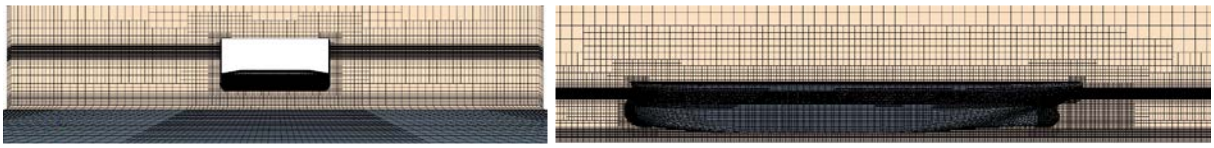

Figure 2.2: Grid structure around ship and bottom in shallow waters. Cross section at mid-ship (left) and longitudinal section at symmetry (right). Source: Liu *et al.* (2017).

3 FUNDAMENTALS ON SHIP RESISTANCE

The vessel resistance is a force acting on the vessel during navigation at a given velocity. The direction of this force is opposite to the direction of the motion. The total resistance can be obtained through theoretical, experimental and computational calculations. This chapter will define the basic components of the resistance. Following, the resistance calculation methods will be described. Later, the shallow water effects will be described considering that the resistance in depth water is different to the resistance in deep water. Finally, the existing empirical methods will be contextualized.

3.1 Components of resistance

The total resistance is divided in basic components (shown in the Figures 3.1 and 3.2) (HARVALD, 1983; MOLLAND; TURNOCK; HUDSON, 2011):

- Frictional resistance: frictional forces between water and hull surface due to tangential shear forces in direction of motion.
- Pressure resistance: pressure force of water (normal forces) acting in the direction of motion.
- Viscous resistance: is associated with the energy expended due to viscous effects.
- Wave-making resistance: is associated with the energy generated by gravity waves during navigation.
- Viscous pressure resistance: is obtained by the integration of the components of the normal stresses acting on the hull due to viscosity and turbulence.

The following list contains additional resistance components:

- Residuary resistance: Considering the Froude's approach, the residuary resistance can be obtained by subtracting the skin friction resistance from the total resistance.

- Wave-pattern resistance: is the resistance (deduced from measurements of wave elevations) where the wave pattern at a point remote from the vessel or model, is related, through a linearized theory, to the ship's or model's subsurface velocity field and, therefore, the momentum of the fluid. This resistance does not include wave-breaking resistance.
- Wave-breaking resistance: is associated with the breakdown of the vessel bow wave.
- Spray resistance: is associated with the energy loss resulting from the spray generation.
- Air resistance: is the resistance caused by the incident of wind/air on the vessel during navigation.
- Steering resistance: is the resistance caused by the rudder.

These specific components are shown in the Figure 3.3, where is represented in total resistance coefficient C_t giving as function of length Froude number Fr_L.

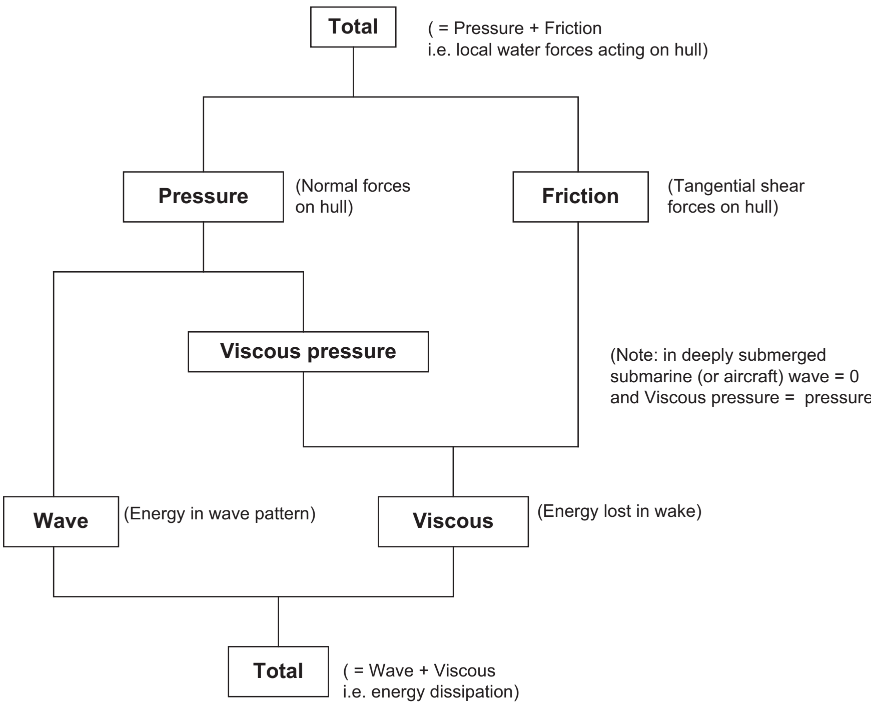

Figure 3.1: Basic resistance components. Source: Molland, Turnock and Hudson (2011).

According to Froude hypothesis, the total resistance is represented by the following formula

$$R_t = R_r + R_f = \frac{1}{2}\rho S_{ws} v^2 C_t, \tag{3.1}$$

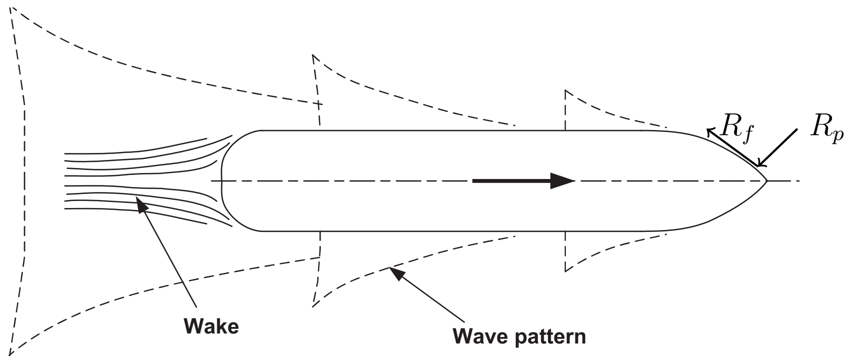

Figure 3.2: Frictional (R_f) and pressure (R_p) forces; wave pattern and wake. Source: Molland, Turnock and Hudson (2011).

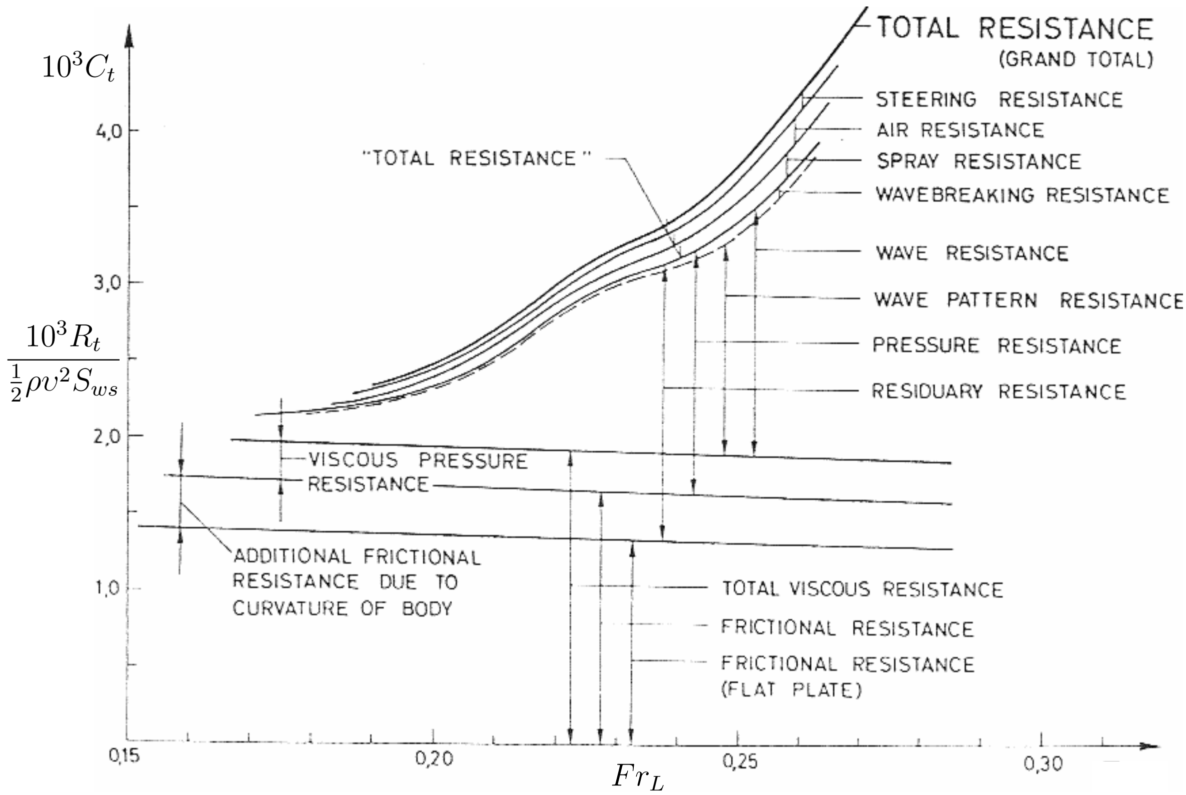

Figure 3.3: Specific components of resistance. Source: Harvald (1983).

where R_r is the residuary resistance, R_f is the frictional resistance, ρ is the density of water, S_{ws} is the wetted surface area of the vessel, v is the velocity of the vessel, and C_t is the total resistance coefficient. C_t is defined as

$$C_t = C_r + C_f, \tag{3.2}$$

where C_f and C_r are the frictional and the residuary resistance coefficients.

The International Towing Tank Conference (ITTC) studied proposals in order to determine the frictional resistance coefficient (HARVALD, 1983). ITTC (1957) proposed the *Model-ship correlation line* providing great accuracy. This coefficient is formulated as

$$C_f = \frac{0.075}{[\log_{10}(Re) - 2]^2}, \tag{3.3}$$

where Re is the Reynolds number.

Reynolds (1883) studied the characterization of the fluid motion in which used flow criteria that indicate whether the flow is laminar, turbulent or at transition stage (Encyclopædia Britannica, 2015f). The Reynolds number is given by

$$Re = \frac{L_{\mathrm{WL}} \upsilon}{\nu}, \tag{3.4}$$

where L_{WL} is the length of the vessel in waterline and ν is kinematic viscosity of water, represented as

$$\nu = \frac{\mu}{\rho}, \tag{3.5}$$

where μ is the dynamic viscosity.

The residuary resistance coefficient is calculated according to Guldhammer's and Harvald's method (1974)

$$C_r = f\left(Fr_L, \frac{L_{\mathrm{WL}}}{\Lambda^{\frac{1}{3}}}, \Phi\right), \qquad \text{if } \frac{B}{T} = 2.5, \tag{3.6}$$

where Fr_L is the length Froude number, Λ is the vessel's displacement, Φ is the prismatic coefficient of the vessel, B is the vessel's beam, and T is the vessel's draft. This coefficient can be determined by nine diagrams (see the Figures from A.1 to A.9) for L_{WL}/Λ ratios ranging from 4 to 8 at intervals of 0.5. Additionally, each diagram provides the mean curves of C_r for Φ between 0.5 and 8.0. The values of Fr_L are between 0.15 and 0.45. The diagrams refer to a B/T ratio equal to 2.5 and were obtained through experimental tests corresponding to ship models.

Georgakaki and Sorenson (2004) mentioned that the Guldhammer's and Harvald's curves can extrapolate the values of C_r. In case of Fr_L lower than 0.15, is equal to the C_r value for Fr_L equal to 0.15. The formulation involved is

$$10^3 C_r = E_1 + G + H + K, \tag{3.7}$$

where

$$E_1 = \left(A_0 + 1.5Fr_L^{1.8} + A_1 + Fr_L^{N_1}\right)\left[0.98 + \frac{2.5}{(M-2)^4}\right] + (M-5)^4(Fr_L - 0.1)^4, \tag{3.8}$$

$$A_0 = 1.35 - 0.23M + 0.012M^2, \tag{3.9}$$

$$A_1 = 0.0011M^{9.1}, \tag{3.10}$$

$$N_1 = 2M - 3.7, \tag{3.11}$$

$$G = \frac{B_1 B_2}{B_3}, \tag{3.12}$$

$$B_1 = 7 - 0.09M^2, \tag{3.13}$$

$$B_2 = (5\Phi - 2.5)^2, \tag{3.14}$$

$$B_3 = [600(Fr_L - 0.315)^2 + 1]^{1.5}, \tag{3.15}$$

$$H = \exp\{80[Fr_L - (0.04 + 0.59\Phi)] - [0.015(M - 5)]\}, \tag{3.16}$$

$$K = 180Fr_L^{3.7}\exp(20\Phi - 16), \tag{3.17}$$

$$M = \frac{L}{\Lambda^{\frac{1}{3}}}. \tag{3.18}$$

The equation (3.7) is applicable to self-propelled vessels and convoys but does not applied to pushed convoys.

The Froude number Fr is the dimensionless quantity that indicates the influence of gravity on fluid motion (Encyclopædia Britannica, 2015c). In marine hydrodynamic applications, this is important to calculate the ship resistance using length Froude number. For shallow waters, is applied the depth Froude number that will be explained in the next subsection. The length Froude number is determined by

$$Fr_L = \frac{v}{\sqrt{gL_{\mathrm{WL}}}}, \tag{3.19}$$

where g is the gravitational acceleration. The prismatic coefficient is given by

$$\Phi = \frac{\Lambda}{L_{\mathrm{WL}}BT\beta}, \tag{3.20}$$

where β is the midship section area coefficient of the vessel, represented by

$$\beta = \frac{A_{ims}}{BT}, \tag{3.21}$$

where A_{ims} is the immersed midship area of the vessel.

The correction of the residuary resistance coefficient for vessels with beam to draft ratio of value higher or lower than 2.5 is determined by

$$10^3 C_r = 10^3 C_{r_{\frac{B}{T}=2.5}} + 0.16\left(\frac{B}{T} - 2.5\right). \tag{3.22}$$

3.2 Shallow water effects

The performance of a ship engaged in sea transport is different to the performance of an inland vessel due to aspects such as cruising velocities, maneuverability, stability and river's/channel's geographic morphology and infrastructure. The term "shallow water" refers to the boundaries close to the ship in vertical and horizontal direction.

The principal effects of shallow waters are (MOLLAND; TURNOCK; HUDSON, 2011):

- Effective increase in velocity and backflow;
- Decrease in pressure under the hull;
- Significant changes in sinkage and trim;
- Increases in skin friction drag and wave resistance.

Shallow water effects are characterized by depth Froude number, related to the velocity of the vessel υ_∞ and the local depth of the river h, obtained by

$$Fr_h = \frac{\upsilon_\infty}{\sqrt{gh}}. \tag{3.23}$$

The vessel produces system waves which travel with velocities that depends on the water depth h and the wave length λ. In deep water, when h/λ ratio is large, the wave velocity is defined as

$$c = \sqrt{\frac{g\lambda}{2\pi}} \qquad \text{if } \frac{h}{\lambda} \geq \frac{1}{20}. \tag{3.24}$$

In shallow water, when the value of this relationship is small,

$$c = \sqrt{gh} \qquad \text{if } \frac{h}{\lambda} < \frac{1}{20}. \tag{3.25}$$

The waves travel at the same velocity c as the velocity of the ship. In this case, c is known as the critical velocity (MOLLAND; TURNOCK; HUDSON, 2011).

In the Figure 3.4, shows the wave patterns. The propagation of the transversal waves system and divergent waves system occurs away from the vessel for subcritical values ($Fr_h < 1$), producing an angle of 35°. At critical velocity ($Fr_h = 1$) the wave angle is perpendicular to the track of ship, generating an angle of 0°. At supercritical velocities ($Fr_h > 1$), there is no transversal waves and the divergent waves produce wave with a propagation angle

$$\theta = \cos^{-1}\left(\frac{1}{Fr_h}\right), \tag{3.26}$$

because a gravity wave cannot travel at $c > \sqrt{gh}$. These observations can be visualized in the Figure 3.5, and are the result of the experimental test according to Molland, Wilson and Taunton (2004).

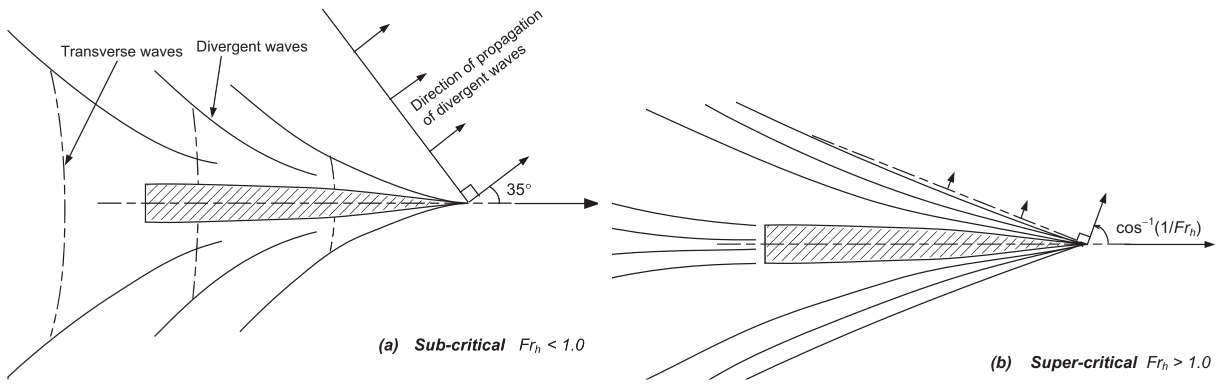

(a) Subcritical ($Fr_h < 1$) (b) Supercritical ($Fr_h > 1$)

Figure 3.4: Subcritical and supercritical wave patterns. Source: Molland, Turnock and Hudson (2011).

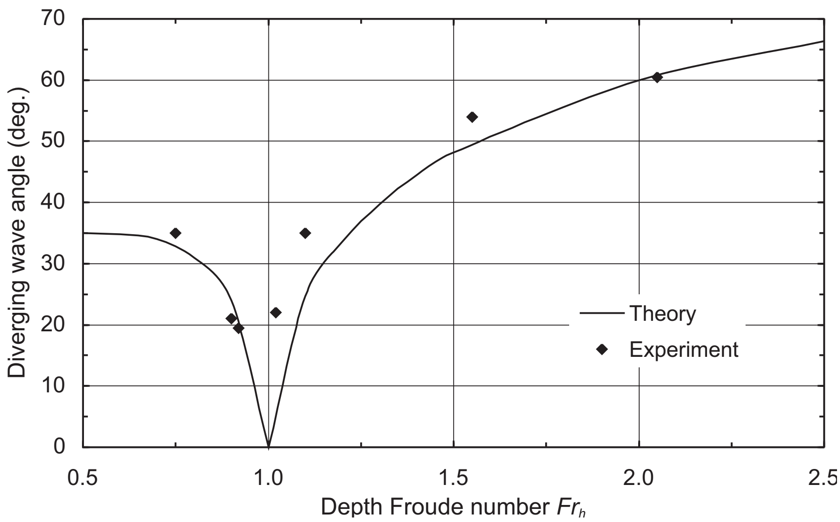

Figure 3.5: Changes of divergent wave angle in function of depth Froude number. Source: Molland, Wilson and Taunton (2004); Molland, Turnock and Hudson (2011).

Molland, Turnock and Hudson (2011) show the performance of the resistance, described in the Figure 3.6, displaying great variation of the resistance in shallow water. When the velocity is greater than critical, the value of R_t in shallow waters reduces again and and becomes a little lower than the R_t in deep water navigation. The ratio of shallow to deep water wave-making resistances Rw_h/Rw_D is illustrated in the Figure 3.7, where the maximum value is 4.0, typically, when Fr_h is approximately 1.0 (in general in the range of 0.96 to 0.98) implying the decrease of the propeller efficiency. These effects (described in the Figure 3.8) show a lower value of h/L_{WL} ratio and Rw peaks with a high value. The ratio marked as ∞ is for deep water. The value of 0.75 for the h/L_{WL} ratio corresponds to the critical velocity.

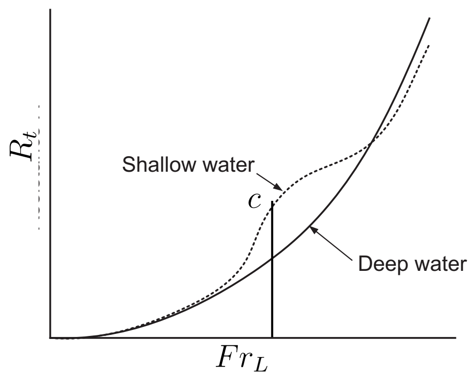

Figure 3.6: Influence of shallow water on the resistance curve. Source: Molland, Turnock and Hudson (2011).

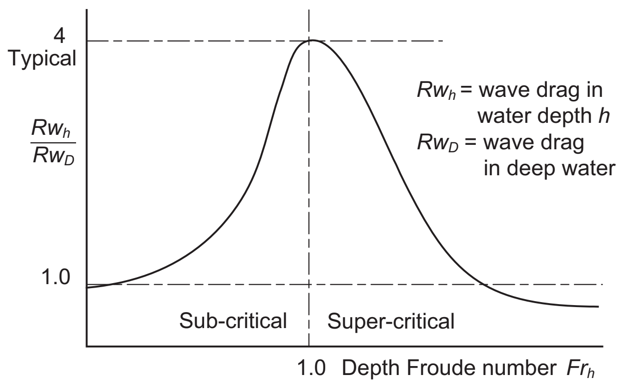

Figure 3.7: Amplification of wave-making resistance. Source: Molland, Turnock and Hudson (2011).

In the Figure 3.9 shows the distribution of the pressure and the velocity of a fluid around a symmetric body. The flow is slower at the bow and the stern of the ship, and faster at midship. Before the flow touches the hull, the velocity is constant and no pressure. When the flow is in contact in the bow and the stern, its velocity is zero and its pressure is high. At the middle of the body, the velocity of the flow is higher, and its pressure is lower according to Bernoulli's principle. The boundary layer of a body increases significantly the viscous resistance. The pressure and the velocity distribution can be altered due to vortex formation that occurs close to the hull surface (BERTRAM, 2000).

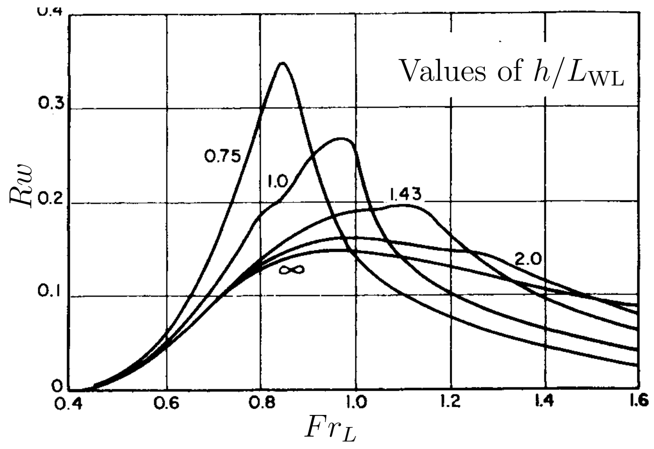

Figure 3.8: Effect of shallow water on wave-making resistance. Source: Lewis (1988).

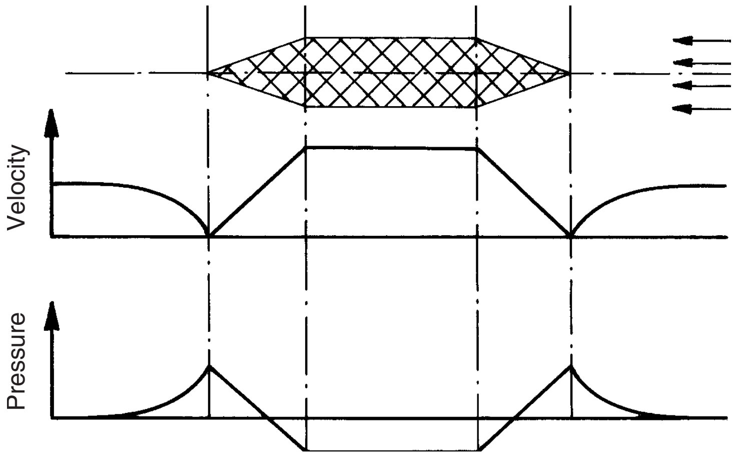

Figure 3.9: Distribution of the velocity and the pressure of a fluid around a symmetry body. Source: Bertram (2000).

It is highly important to define whether the vessel's velocity, during navigation in certain local depths, is super-critical, sub-critical or critical, as illustrated in the Figure 3.10.

According to ITTC (1987), some typical parameters and their values must be considered so as to estimate the river restrictions, e.g.,

- The depth Froude number Fr_h influences on wave resistance ($Fr_h > 0.7$);
- The water-depth to draught ratio h/T influences the flow around the hull, independent of the Fr_h value (if $h/T < 4$);
- For river width to vessel's beam ratio B_c/B, the flow around the hull changes (if $B_c/B < 4$);
- The relationship between the river section area and the immerse midship section

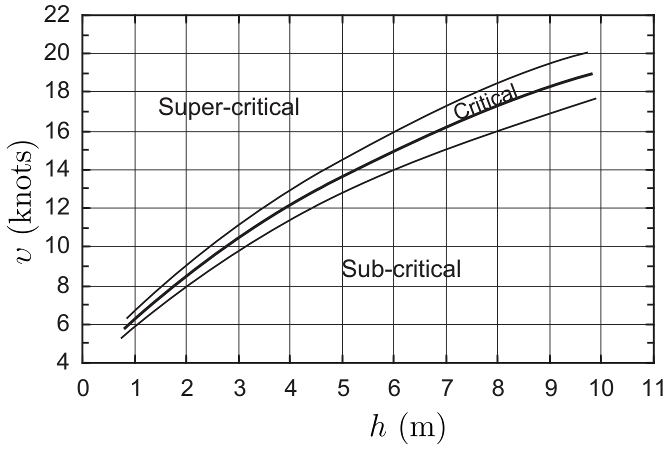

Figure 3.10: Sub-critical and super-critical operating regions. Source: Molland, Turnock and Hudson (2011).

area A_c/A_{ims} is the beginning of the restriction waterway (if $A_c/A_{ims} < 15$).

Pompée (2015) established models to estimate the inland vessel's resistance, depending on the type of vessels (self-propelled or pushed convoys) and the characteristics of the river as shown in the Figure 3.11. The traditional shallow water methods for large rivers (as Danube) are based on velocities of Schlichting (1934), Landweber (1939) and Lackenby (1963). The diagrams by Karpov (1946) and the correction of the wall effect by Artjushkov (1968) for middle rivers (as Rhine and Rhone) are used.

3.2.1 Large rivers

Schlichting (1934) carried out the analysis of shallow water effects based on theoretical considerations and model experiments. In model tests, the author only took into account the reduction of the water depth and did not consider the increasing influence of the banks (tank width) in a towing tank.

In the Figure 3.12 is shown the frictional R_f and total R_t resistance curves in deep and shallow water to a base of velocity. The ship generates a wave pattern giving a wave length λ for velocity υ_∞ in deep water

$$\upsilon_\infty^2 = \frac{g\lambda}{2\pi}. \tag{3.27}$$

The same wave length λ would be generated at some lower or intermediate velocity υ_I in a specific water depth h, and is expressed as

$$\upsilon_I^2 = \frac{g\lambda}{2\pi}\tanh\left(\frac{2\pi h}{\lambda}\right). \tag{3.28}$$

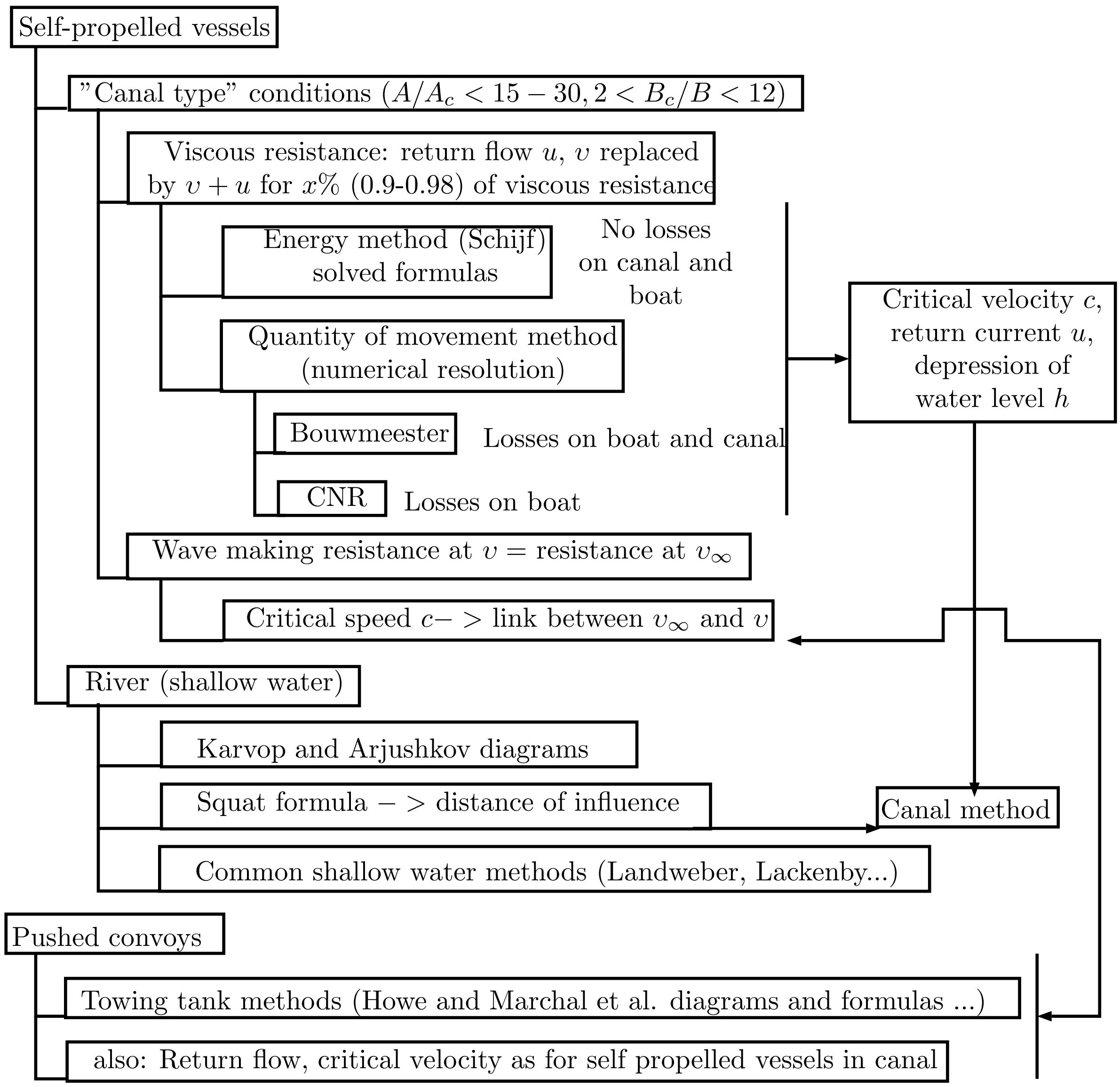

Figure 3.11: Models available depending on the situation and the vessel. Source: Pompée (2015).

The ratio between these two velocities is

$$\frac{v_I}{v_\infty} = \sqrt{\tanh\left(\frac{gh}{v_\infty^2}\right)} = \sqrt{\tanh\left[\left(\frac{\sqrt{gh}}{v_\infty}\right)^2\right]} = \sqrt{\tanh\left(\frac{2\pi h}{\lambda}\right)}. \tag{3.29}$$

and is plotted a curve to a base of $v_\infty/\sqrt{gh}$ in the Figure 3.13. The values less of 0.4, the shallow water effect on the wake-making resistance Rw is unimportant. The difference between these velocities is (Figure 3.12)

$$v_\infty - v_I = \delta C, \tag{3.30}$$

and the Schlichting's assumption is that the wave-making resistance Rw in shallow waters at velocity v_I (line BF) would be the same as that velocity v_∞ in deep water (line AE). In the point B is located the total resistance at velocity v_I adding Rw in deep water and R_f in depth water. The line AB is parallel to EF (LEWIS, 1988).

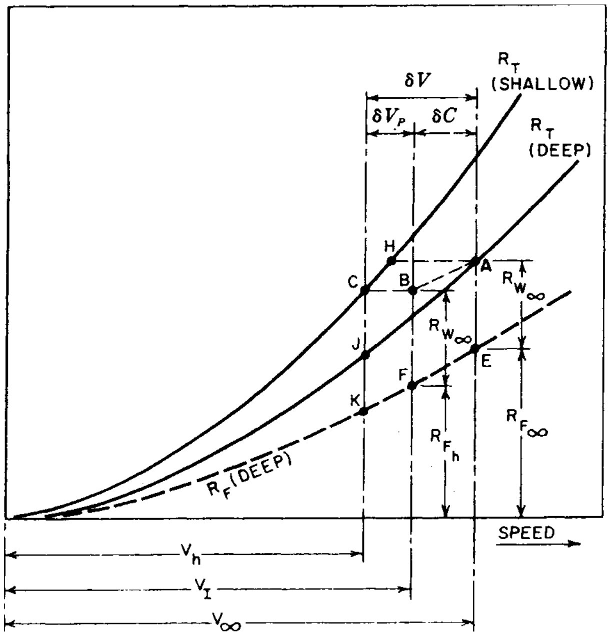

Figure 3.12: Determination of shallow water resistance by Schlichting's method. Source: Lewis (1988).

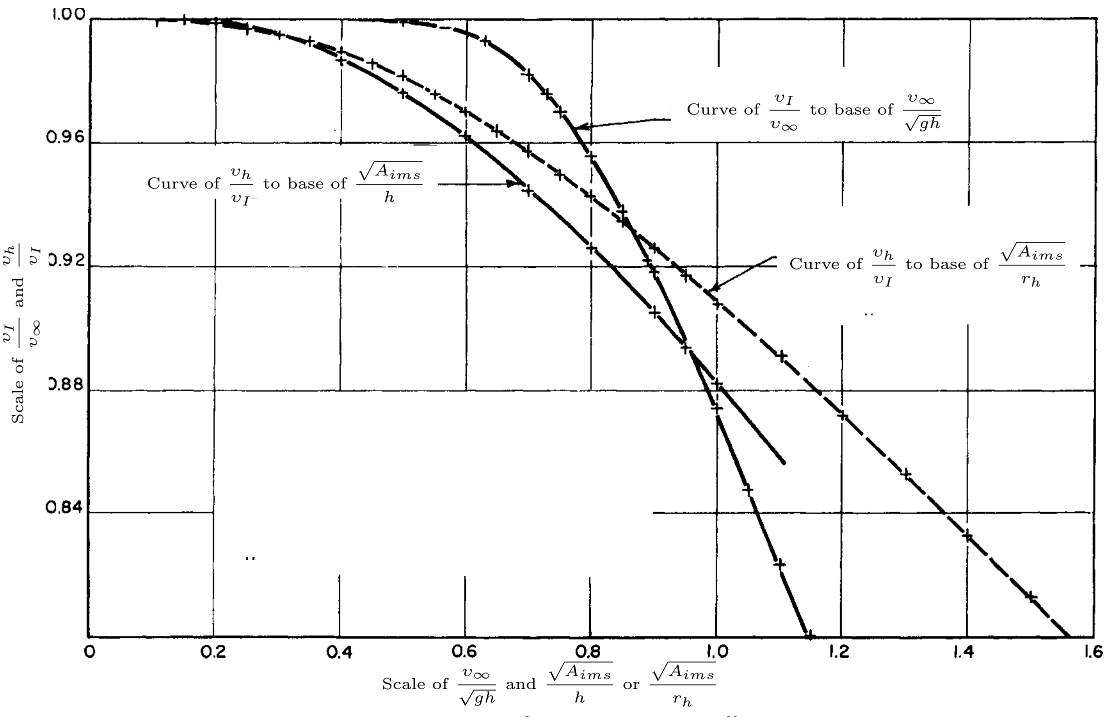

Figure 3.13: Curves of velocity ratios for the calculation of the resistance in shallow water. Source: Lewis (1988).

The increase in potential or displacement flow around the hull due to the restriction of area by the proximity of the bottom generate a further loss in velocity δv_p, giving

$$v_h = v_I - \delta v_p. \tag{3.31}$$

Later, Schlichting investigated this reduction of the velocity of the vessel in shallow waters, and found that the factor to control further loss in velocity was the ratio

$$\frac{\sqrt{A_{ims}}}{h}. \tag{3.32}$$

In the Figure 3.13 is plotted the curves of v_h/v_I in function of the equation 3.32. In the Figure 3.12, the distance of δv_p is parallel to the line BC, and the point C is the curve of total resistance in shallow waters at velocity v_h.

The total velocity loss is determined as

$$\delta v = \delta C - \delta v_p, \tag{3.33}$$

which can be expressed in percentage terms

$$\frac{\delta v}{v_\infty} \times 100 = \frac{v_\infty - v_h}{v_\infty} \times 100 = f\left(\frac{v_\infty^2}{gh}, \frac{\sqrt{A_{ms}}}{h}\right). \tag{3.34}$$

The above are given in contour form, illustrated in the Figure 3.14.

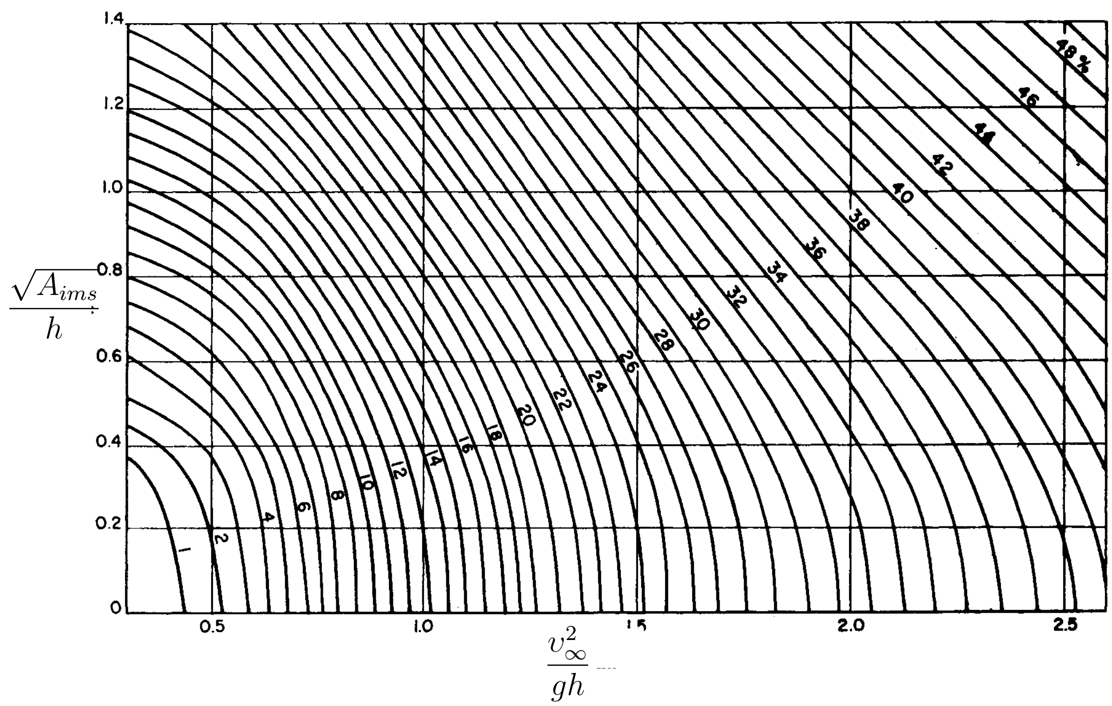

Figure 3.14: Schlichting's chart for calculate the loss in velocity of the vessel. Source: Lewis (1988).

Landweber (1939) analysed the Schlichting's method for the prediction of the resistance shallow water in case of restricted channels. He proposed a hydraulic radius that can be determined by the ratio of the cross-section area of the channel to the wetted perimeter (Figure 3.15)

$$r_h = \begin{cases} \dfrac{B_c h}{B_c + 2h} & \text{(a) for rectangular channel of } B_c \text{ and } h, \\ h & \text{(b) when } b \text{ becomes very large,} \\ \dfrac{B_c h - A_{ims}}{B_c + 2h + q_s} & \text{(c) model is in a rectangular channel.} \end{cases} \tag{3.35}$$

where B_c is the width of the channel and q_s is the wetted girth of the hull that is determined as:

$$q_s = B + 2T. \tag{3.36}$$

Introducing B_c in the equation (3.32), h is replaced by r_h, and is expressed as

$$\frac{\sqrt{A_{ims}}}{r_h}. \tag{3.37}$$

Lackenby (1963) presented a semi-empirical formula as a complement to Schlichting's method

$$\frac{dv}{v_\infty} \times 100 = \left[0.1242\left(\frac{A_{ims}}{h^2} - 0.05\right) + 1 - \sqrt{\tanh\left(\frac{gh}{v_\infty^2}\right)}\right] \times 100 \quad \text{if } \frac{A_{ims}}{h^2} > 0.05, \tag{3.38}$$

which is given in contour form illustrated in the Figure 3.16. He observed some points of interest. In the area ABCD there is no shallow water effect. In BEFC, there is a "back-flow" effect. In DCHJ there is wave-retardation. In CFGH back-flow and wave-retardation are significant.

The methods for large rives must be limited to the range of the diagram shown in the Figure 3.13, i.e.

$$\frac{v_\infty}{\sqrt{gh}} \leq 1.14846, \qquad \frac{\sqrt{A_{ims}}}{h} \leq 1.3, \qquad \frac{\sqrt{A_{ims}}}{r_h} \leq 1.558. \tag{3.39}$$

3.2.2 Medium rivers

According to Karpov (1946), the vessel resistance in shallow water divided into the frictional and residuary resistance as a function of, instead of cruising velocity, the two

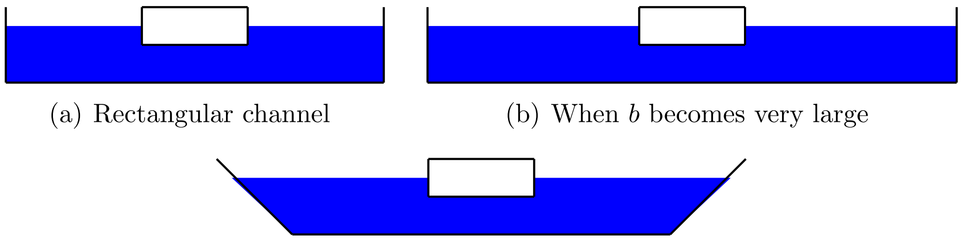

(a) Rectangular channel (b) When b becomes very large

(c) When the model is in a rectangular channel

Figure 3.15: Different cross-section of the channels for Landweber's method. Source: Author.

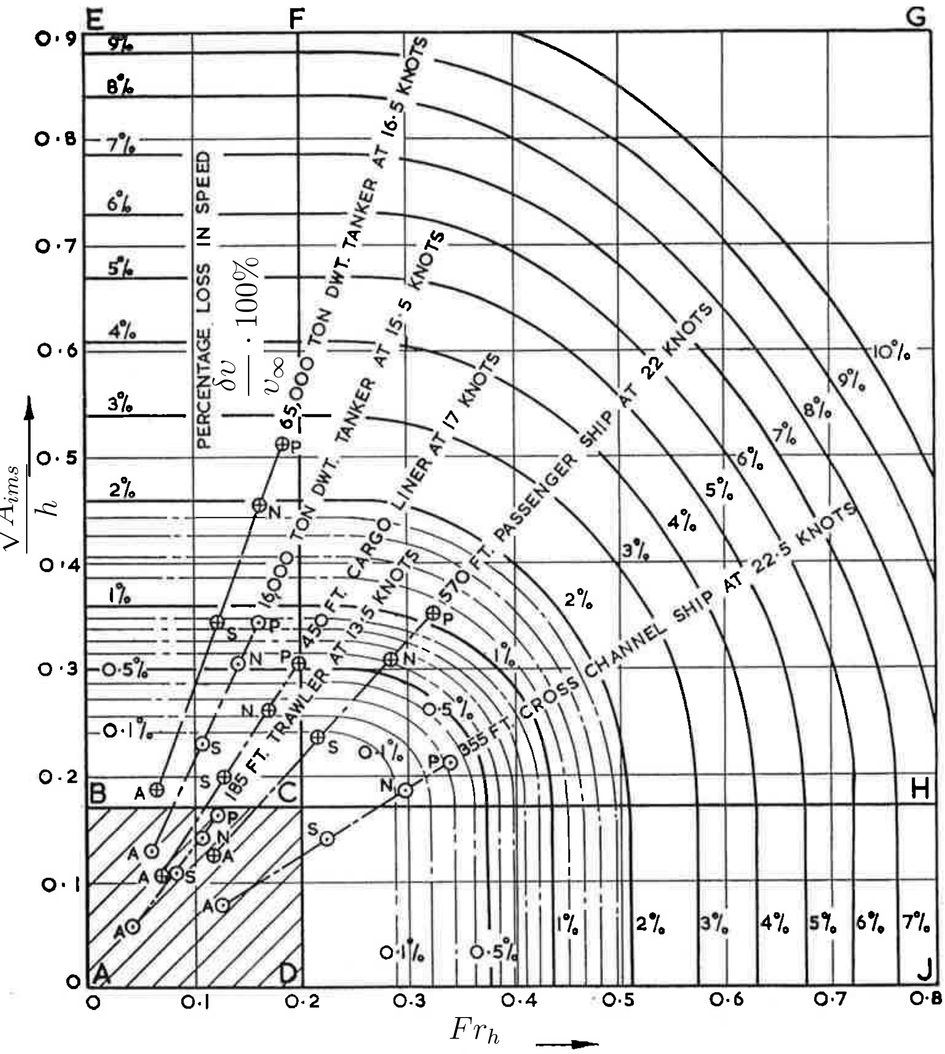

Figure 3.16: Loss in velocity in shallow water. Source: Lackenby (1963).

different velocities velocities v_1 and v_2 operating in waterways with a local depth h

$$R_t(v_\infty) = \frac{1}{2}\rho S_{ws}\left[(C_f + C_a)v_1^2 + C_r v_2^2\right], \tag{3.40}$$

where C_a is the correlation allowance that is used for the calculation of the total resistance of the vessel in full scale, otherwise, is zero. The effective velocities v_1 and v_2 are expressed as

$$v_1 = \frac{v_\infty}{\alpha^*}, \qquad\qquad v_2 = \frac{v_\infty}{\alpha^{**}}, \tag{3.41}$$

where α^* and α^{**} are coefficients that can be determined from the diagrams shown in the Figure 3.17. These values depend on the h/T ratio curves and Fr_h.

The correlation allowance is applied to the correction of the vessel's frictional coefficient. The value varies depending on the ship length and, rarely, the displacement. According to Harvald (1983) this coefficient has been fixed at 0.0004. This variable is not applied in this study because only the model scale of the vessel is calculated.

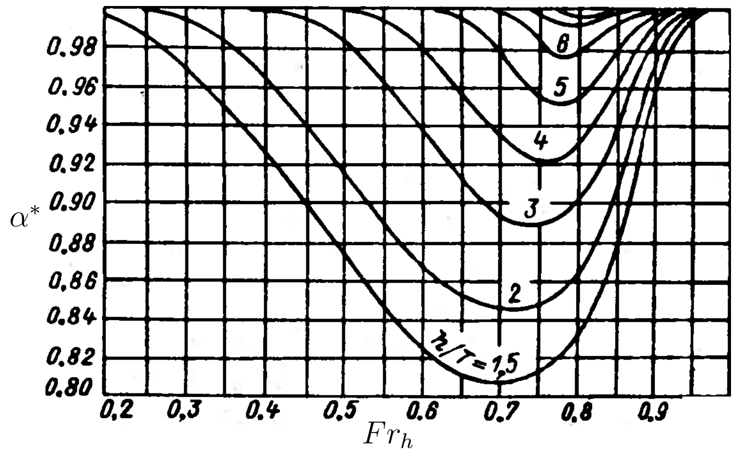

(a) α^*

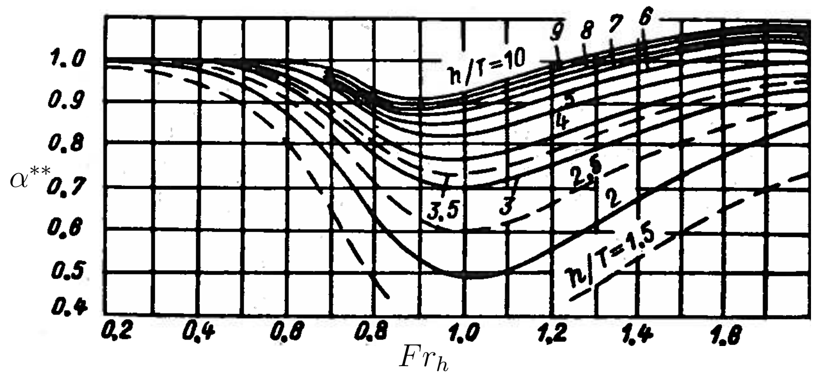

(b) α^{**}

Figure 3.17: Karpov's diagrams for the determination of the coefficients α^* and α^{**}. Source: Latorre, Luthra and Tang (1982).

Artjushkov (1968) improved the Karpov's analysis by including a correction for the width effect on the residuary resistance coefficient, this correction composed of two terms, the first, is the residuary resistance coefficient correction ΔC_r; and second, the velocity ratio v'/v_∞. This terms are determined in the Tables 3.1 and 3.2.

The total resistance in shallow waters determined by Karpov and Artjushkov is calculated as

$$R_t(\upsilon_\infty) = \frac{1}{2}\rho S_{ws}\left\{[C_f + C_a]\,\upsilon_1^2 + \left[C_r\left(\frac{\upsilon}{\upsilon'}\right)^2 + \Delta C_r\right]\upsilon_2^2\right\}. \tag{3.42}$$

Finally, Georgakaki and Sorenson proposed the equations for the approximation of the variables α^*, α^{**}, ΔC_r and $\upsilon'/\upsilon_\infty$, and these are shown in the Table A.1. Also, they recommend limit the diagrams and the tables above within the parameters, i.e.,

$$1.5 \le \frac{h}{T} \le 10.0, \qquad Fr_h \le 0.6 \text{ to } 0.7, \qquad 0.04 \le \frac{B}{B_c} \le 0.30. \tag{3.43}$$

	B/B_c						
h/T	0.040	0.080	0.120	0.160	0.200	0.250	0.300
1.500	0.040	0.097	0.161	0.247	0.348	0.482	-
2.000	0.034	0.081	0.137	0.203	0.279	0.386	0.570
2.500	0.028	0.067	0.112	0.162	0.218	0.300	0.418
3.000	0.023	0.054	0.089	0.127	0.166	0.225	0.302
3.500	0.018	0.041	0.068	0.096	0.125	0.168	0.223
4.000	0.013	0.030	0.050	0.072	0.094	0.126	0.172
5.000	0.008	0.016	0.028	0.042	0.057	0.082	0.115
6.000	0.005	0.011	0.020	0.032	0.043	0.062	0.089
8.000	0.003	0.007	0.011	0.019	0.028	0.045	0.066
10.000	0.003	0.007	0.011	0.018	0.026	0.038	0.055

Table 3.1: Residuary resistance coefficient corrections ΔC_r for different channels by Artjushkov. Source: Artjushkov (1968), Latorre, Luthra and Tang (1982).

	B/B_c						
h/T	0.040	0.080	0.120	0.106	0.200	0.250	0.300
1.500	0.968	0.933	0.894	0.849	0.795	0.699	-
2.000	0.978	0.950	0.921	0.886	0.843	0.780	0.685
2.500	0.982	0.962	0.938	0.913	0.885	0.846	0.796
3.000	0.986	0.970	0.952	0.934	0.915	0.889	0.859
3.500	0.989	0.977	0.965	0.952	0.938	0.918	0.895
4.000	0.992	0.983	0.974	0.946	0.953	0.937	0.916
5.000	0.996	0.990	0.983	0.976	0.968	0.957	0.941
6.000	0.997	0.993	0.989	0.983	0.977	0.967	0.954
8.000	0.999	0.996	0.994	0.989	0.985	0.977	0.965
10.000	0.999	0.996	0.994	0.990	0.987	0.980	0.971

Table 3.2: Velocity relations $\upsilon'/\upsilon_\infty$ for a model in different channels by Artjushkov. Source: Artjushkov (1968), Latorre, Luthra and Tang (1982).

3.3 Empirical procedure

This chapter is summarized with a flowchart in two parts. In the Figure 3.18 shows the empirical part in case of inland vessel accomplish inside of the parameters represented in the equation (3.39). Otherwise, in the Figure 3.19 describes the Karpov's and Artjushkov's methods if the inland ship accomplish within the parameters, shown in the equation (3.43).

3.4 Hypothesis

The empirical methods for the calculation of the vessel's resistance, used in this paper, are based on models applicable to middle rivers for shallow water navigation. The hypotheses are numerated as follows:

- The inland vessel is self-propelled;
- The type of waterway is a middle river;
- There is a restriction of the river width.

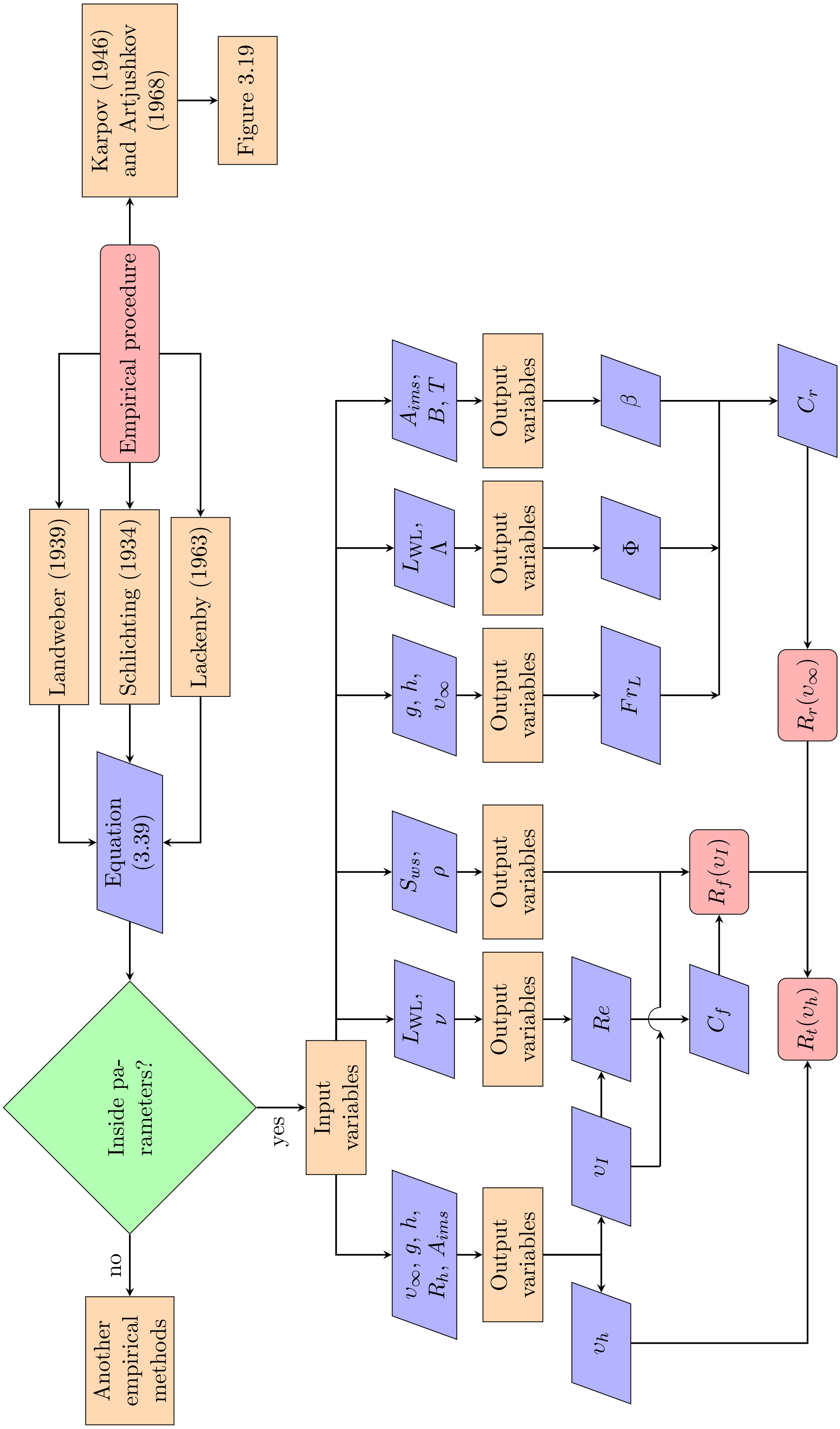

Figure 3.18: Empirical procedure (part 1). Source: Author.

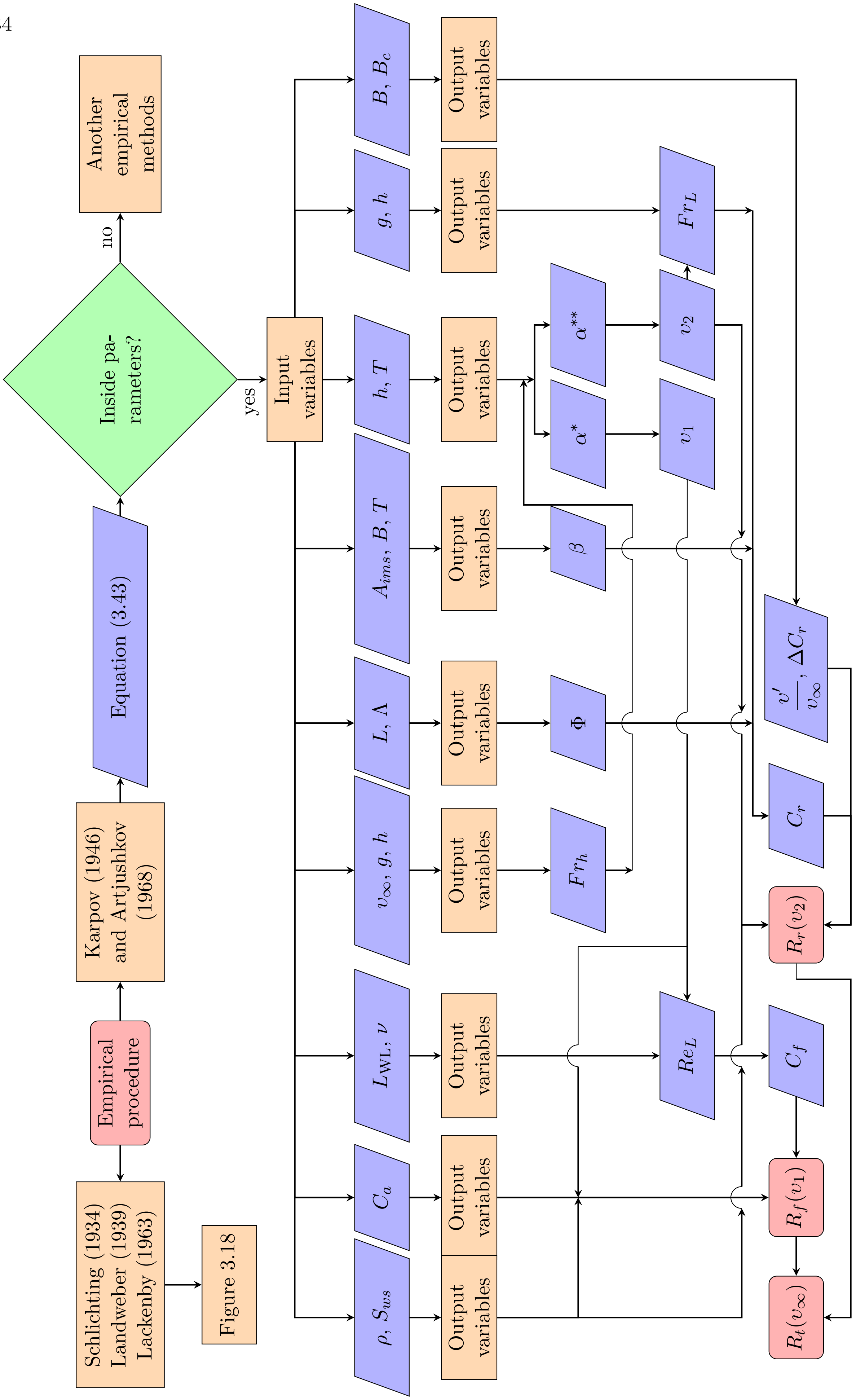

Figure 3.19: Empirical procedure (part 2). Source: Author.

4 NUMERICAL SIMULATION BY CFD

This chapter provides a systematic review of the main fundamentals regarding the Computational Fluid Dynamics (CFD). For this purpose, the equations that govern the motions of the fluids are presented. First, the Navier-Stokes (NS) equation is used to obtain the Reynolds-Averaging Navier-Stokes (RANS) equation by means of Reynolds decomposition. The Realizable k-ε turbulence model and the Finite Volume Method (FVM) are applied in order to simulate the turbulent flow and in order to calculate values at specific points/small areas in a cell or element of a mesh, respectively. For tracking and locating the free surface between air and water, the Volume of Fluid (VOF) method is used. Additionally, the implementation of the boundary conditions is explained.

4.1 Hypotheses

The computational methods, used in this paper, are based on the RANS equations in three dimensions applying the realizable k-ε turbulence model. For the solution of the problem, the following hypotheses are adopted:

- The fluids (air and water) are incompressible and Newtonian;
- The flows are three-dimensional and non-stationary;
- The surface tension between air and water is ignored;
- The calculation of the inland vessel's sinkage and trim will not be applied.

4.2 Conservation of mass

Is the principle in which the mass of an object, set of objects or any closed system does not remains unchanged over time. Its equation is represented mathematically by the following equation

$$\frac{\partial}{\partial t}\int_V \rho dV = -\int_A \rho \mathbf{u}\cdot\mathbf{n}dA, \tag{4.1}$$

where A is the closed surface area that encloses a volume V (fixed in the space), $\mathbf{u}$ is the flow velocity vector and $\mathbf{n}$ is the normal vector. The left term is the rate of change of mass and the right term is the net inflow of mass (BATCHELOR, 1967). The equation must be written as[1],

$$\int_V \left[\frac{\partial \rho}{\partial t} + \nabla\cdot(\rho\mathbf{u})\right] dV = 0, \tag{4.2}$$

and the integrand is identically zero everywhere in the fluid. This relation is valid for any volume domain. Thus,

$$\frac{\partial \rho}{\partial t} + \nabla\cdot(\rho\mathbf{u}) = 0, \tag{4.3}$$

where ρ is the fluid density, t is time and $\nabla\cdot$ is the divergence operator.

The equation above is called *equation of continuity* and is one of the fundamental equations of the fluid mechanics. In Cartesian coordinates, is expressed as

$$\frac{\partial \rho}{\partial t} + \frac{\partial}{\partial x_i}(\rho u_i) = 0, \qquad i = 1, 2, 3, \tag{4.4}$$

where x_i are components of Cartesian coordinates and u_i are components of velocity vector. If the fluid is considered incompressible, the equation is reduced to a simpler condition

$$\nabla\cdot\mathbf{u} = 0, \tag{4.5}$$

in Cartesian coordinates,

$$\frac{\partial u_i}{\partial x_i} = 0. \tag{4.6}$$

4.3 Conservation of momentum

Is associated with Newton's second law where, in a closed system, the total momentum is constant. For fluids, where the material surface S_{mat} encloses the volume, the momentum is estimated by

$$\int_V \rho\mathbf{u}dV, \tag{4.7}$$

and its rate of change is

[1] Using the divergence theorem, the net inflow of mass is expressed by

$$-\int_A \rho\mathbf{u}\cdot\mathbf{n}dA = -\int_V \nabla\cdot(\rho\mathbf{u})dV$$

$$\frac{d}{dt}\int_V \rho\mathbf{u}dV = \int_V \frac{D\mathbf{u}}{Dt}\rho dV = \int_V \rho F_i dV + \int_{S_{\text{mat}}} \tau_{ij}n_j dS_{\text{mat}},$$
$$= \int_V \rho F_i dV + \int_V \frac{\partial \tau_{ij}}{\partial x_j}dV, \tag{4.8}$$

where n_j are components of the normal vector to the surface. The integrand is identically zero everywhere in the fluid. Hence[2]

$$\rho\frac{D\mathbf{u}}{Dt} = \rho F_i + \frac{\partial \tau_{ij}}{\partial x_j}, \tag{4.9}$$

$$\frac{\partial}{\partial t}(\rho\mathbf{u}) + \rho(\mathbf{u}\cdot\nabla\mathbf{u}) = F_b + F_s, \tag{4.10}$$

where F_b are the body forces, F_s are the surface forces and ∇ is the nabla operator.

The body forces are those that are applied to the entire mass of the fluid element, such as the gravity force. These forces are expressed as

$$F_b = \rho F_i = \rho g, \tag{4.11}$$

where F_i are components of the force vector and g is the vector acceleration of gravity. The surface forces are those that act across the surface, shown in the Figure 4.1, and are given by

$$F_s = \frac{\partial \tau_{ij}}{\partial x_j} = \nabla\cdot\tau_{ij}, \tag{4.12}$$

where τ_{ij} are components of the tensor stress.

Replacing the equations (4.11) and (4.12) into the equation (4.9), the Newton's second law for fluids now becomes (WHITE, 1991)

$$\rho\frac{\partial\mathbf{u}}{\partial t} + \rho(\mathbf{u}\cdot\nabla\mathbf{u}) = \rho g + \nabla\cdot\tau_{ij}, \tag{4.13}$$

in Cartesian coordinates,

$$\frac{\partial}{\partial t}(\rho u_i) + \frac{\partial}{\partial x_j}(\rho u_i u_j) = \rho g + \frac{\partial \tau_{ij}}{\partial x_j}. \tag{4.14}$$

[2] The left term is expressed in material derivative as

$$\frac{D\mathbf{u}}{Dt} \equiv \frac{\partial\mathbf{u}}{\partial t} + \mathbf{u}\cdot\nabla\mathbf{u}.$$

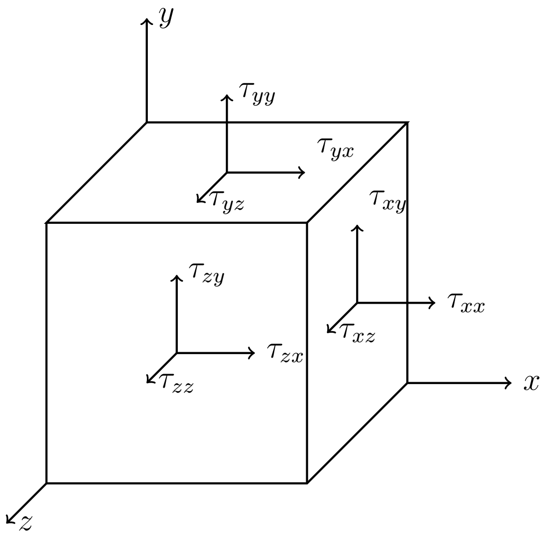

Figure 4.1: Notation for stresses. Source: White (1991).

4.3.1 Newtonian fluid

Newtonian fluids are characterized by a constant viscosity, independently of time and shear stresses (Encyclopædia Britannica, 2015b). Moreover, the shear and strain rates are linearly related in these cases. On the other hand, non-Newtonian fluids do not follow Newtonian's law of viscosity. As a matter of fact, their viscosity is dependent of shear rate and/or shear rate viscosity. In the Figure 4.2 shows the characteristics of τ, described above, for Newtonian and non-Newtonian fluids.

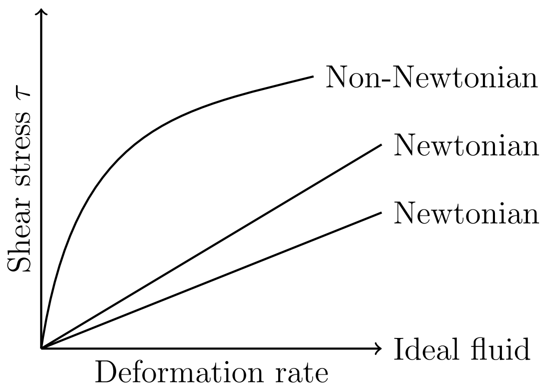

Figure 4.2: Behavior of shear stress for Newtonian and non-Newtonian fluids according to deformation rate. Source: Fortuna (2012).

Mathematically, Sir Isaac Newton proposes a simple relation

$$\tau_{ij} = \mu \frac{du_i}{dx_j} \qquad \text{if } i \neq j, \tag{4.15}$$

where μ is the dynamic (shear) viscosity of the fluid and $\frac{du_i}{dx_j}$ is the velocity gradient perpendicular to the direction to the plane. This equation stands for an incompressible Newtonian fluid.

The constitutive relation of the shear stresses with the pressure p and the viscous friction in Newtonian fluid, is prescribed as[3]

$$\tau_{ij} = -p\delta_{ij} + \mu\left[\nabla\mathbf{u} + (\nabla\mathbf{u})^T - \frac{2}{3}\delta_{ij}(\nabla\cdot\mathbf{u})\mathbf{I}\right], \qquad \text{if } i = j \qquad \tau_{ii} = \sigma_{ii} \tag{4.16}$$

in Cartesian coordinates

$$\tau_{ij} = -p\delta_{ij} + \mu\left(\frac{\partial u_i}{\partial x_j} + \frac{\partial u_j}{\partial x_i} - \frac{2}{3}\delta_{ij}\frac{\partial u_i}{\partial x_i}\right), \qquad \text{if } i = j \qquad \tau_{ii} = \sigma_{ii} \tag{4.17}$$

where δ_{ij} is the Kronecker delta, $\mathbf{I}$ is the identity matrix, and σ_{ii} is the normal stress. The equation is the result of deformation law and it was introduced by Stokes (1845)[4].

4.3.2 The Navier-Stokes equation

The Navier-Stokes (NS) equation is a partial differential equation that describes the motion of the viscous fluid. Euler was the first to describe the ideal equation for incompressible and frictionless fluids. His works was devised in 17th century and published in 1755. Navier (1822) introduced the friction (element viscosity) for more realistic problems of viscous fluids. Stokes (1845) improved on this work although the complete solutions were obtained only for the case of simple two-dimensional flows (Encyclopædia Britannica, 2015e).

Substituting the equation (4.16) into the equation (4.13),

$$\rho\frac{\partial\mathbf{u}}{\partial t} + \rho(\mathbf{u}\cdot\nabla\mathbf{u}) = \rho g - \nabla p + \nabla\cdot\left\{\mu\left[\nabla\mathbf{u} + (\nabla\mathbf{u})^T - \frac{2}{3}\delta_{ij}(\nabla\cdot\mathbf{u})\mathbf{I}\right]\right\}. \tag{4.18}$$

The equation (4.18) is simplified by means of balancing the pressure gradient ∇p^* and gravitational forces g (STULL, 2000; FIELDING, 2005). Defining

$$\nabla p^* = \nabla p - \nabla p_0, \qquad \frac{1}{\rho}\nabla p_0 = g, \tag{4.19}$$

the following is obtained by

$$\rho\frac{\partial\mathbf{u}}{\partial t} + \rho(\mathbf{u}\cdot\nabla\mathbf{u}) = -\nabla p^* + \nabla\cdot\left\{\mu\left[\nabla\mathbf{u} + (\nabla\mathbf{u})^T - \frac{2}{3}\delta_{ij}(\nabla\cdot\mathbf{u})\mathbf{I}\right]\right\}, \tag{4.20}$$

[3]Only in this case, T is the transpose.

[4]For more details about the constitutive relation, see *Deformation Law for a Newtonian Fluid* in White (1991), pp. 65-68.

in Cartesian coordinates,

$$\frac{\partial}{\partial t}(\rho u_i) + \frac{\partial}{\partial x_j}(\rho u_i u_j) = -\frac{\partial p^*}{\partial x_i} + \frac{\partial}{\partial x_j}\left[\mu\left(\frac{\partial u_i}{\partial x_j} + \frac{\partial u_j}{\partial x_i} - \frac{2}{3}\delta_{ij}\frac{\partial u_i}{\partial x_i}\right)\right]. \tag{4.21}$$

If the fluid is incompressible, the equation is reduced in simple terms,

$$\rho\frac{\partial \mathbf{u}}{\partial t} + \rho(\mathbf{u}\cdot\nabla\mathbf{u}) = -\nabla p^* + \mu\nabla^2\mathbf{u}, \tag{4.22}$$

in Cartesian coordinates,

$$\frac{\partial}{\partial t}(\rho u_i) + \frac{\partial}{\partial x_j}(\rho u_i u_j) = -\frac{\partial p^*}{\partial x_i} + \mu\left(\frac{\partial^2 u_i}{\partial x_i^2}\right), \tag{4.23}$$

where ∇^2 is the Laplace operator.

4.4 Reynolds-Averaging

In Reynolds averaging or Reynolds decomposition, introduced in 1895, a quantity is decomposed into a mean (ensemble-averaged or time-averaged) and a fluctuating parts. Consider a stationary turbulent flow. For the velocity components is decomposed by

$$u_i(\mathbf{x}, t) = U_i(\mathbf{x}) + u_i'(\mathbf{x}, t), \tag{4.24}$$

where $U_i(\mathbf{x})$ is the mean velocity, $u_i'(\mathbf{x}, t)$ is the fluctuating velocity and $\mathbf{x}$ is the position vector in vector notation.

The mean velocity is defined by

$$U_i(\mathbf{x}) = \lim_{T_s\to\infty}\frac{1}{T_s}\int_t^{t+T_s} u_i(\mathbf{x}, t)dt, \tag{4.25}$$

where T_s is a long time to relevant period of the fluctuations in u_i. The equation (4.25) is again the same time-averaged value,

$$\overline{U_i}(\mathbf{x}) = \lim_{T_s\to\infty}\frac{1}{T_s}\int_t^{t+T_s} U_i(\mathbf{x})dt = U_i(\mathbf{x}), \tag{4.26}$$

where an overbar is shorthand for the time average. The time-averaging of the fluctuating velocity is

$$\overline{u_i'}(\mathbf{x}) = \lim_{T_s\to\infty}\frac{1}{T_s}\int_t^{t+T_s} \left[u_i(\mathbf{x}, t) - U_i(\mathbf{x})\right] dt = U_i(\mathbf{x}) - \overline{U_i}(\mathbf{x}) = 0. \tag{4.27}$$

This behavior is illustrated in the Figure 4.3 (WILCOX, 1998).

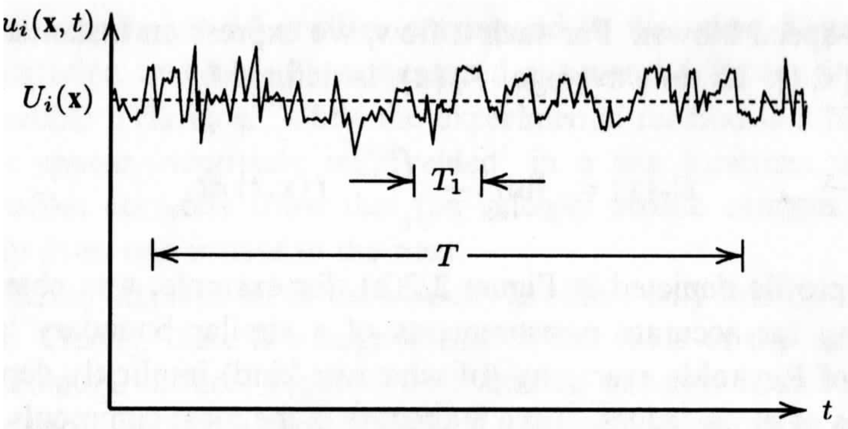

Figure 4.3: Time-averaging for stationary turbulence. Source: Wilcox (1998).

4.5 Reynolds-Averaged Navier-Stokes equation

Aiming at the description of the turbulent flow motions, the Reynolds decomposition is introduced to be applied in the NS equation. First, the velocity components and the pressure are time-averaged,

$$u_i = U_i + u_i', \qquad u_j = U_j + u_j', \qquad p^* = P + p', \tag{4.28}$$

and are replaced in the equation (4.21), expressed by

$$\begin{aligned}&\frac{\partial}{\partial t}\left[\rho(U_i + u_i')\right] + \frac{\partial}{\partial x_j}\left[\rho(U_i + u_i')(U_j + u_j')\right] = \\ &-\frac{\partial}{\partial x_j}(P + p') + \frac{\partial}{\partial x_j}\left\{\mu\left[\frac{\partial}{\partial x_j}(U_i + u_i') + \frac{\partial}{\partial x_i}(U_j + u_j') - \frac{2}{3}\delta_{ij}\frac{\partial}{\partial x_i}(U_i + u_i')\right]\right\}.\end{aligned} \tag{4.29}$$

Time-averaging again the NS equation

$$\begin{aligned}&\frac{\partial}{\partial t}\left[\rho\overline{(U_i + u_i')}\right] + \frac{\partial}{\partial x_j}\left[\rho\overline{(U_i + u_i')(U_j + u_j')}\right] = \\ &-\frac{\partial}{\partial x_j}\overline{(P + p')} + \frac{\partial}{\partial x_j}\left\{\mu\left[\frac{\partial}{\partial x_j}\overline{(U_i + u_i')} + \frac{\partial}{\partial x_i}\overline{(U_j + u_j')} - \frac{2}{3}\delta_{ij}\frac{\partial}{\partial x_i}\overline{(U_i + u_i')}\right]\right\}.\end{aligned} \tag{4.30}$$

In the previous section it was explained that the fluctuating quantity with overbar is equal to zero. The following rules of averaging are determined by

$$\overline{U_i + u_i'} = \overline{U_i} + \overline{u_i'}, \tag{4.31}$$

$$\overline{P + p'} = \overline{P} + \overline{p'}, \tag{4.32}$$

$$\overline{U_i u_i'} = 0, \tag{4.33}$$

$$\overline{u_i u_j} = \overline{(U_i + u_i')(U_j + u_j')} = U_i U_j + \overline{u_i' u_j'}, \tag{4.34}$$

and are applied in the equation (4.30). Hence,

$$\frac{\partial}{\partial t}(\rho U_i) + \frac{\partial}{\partial x_j}(\rho U_i U_j) = -\frac{\partial P}{\partial x_j} + \frac{\partial}{\partial x_j}\left[\mu\left(\frac{\partial U_i}{\partial x_j} + \frac{\partial U_j}{\partial x_i} - \frac{2}{3}\delta_{ij}\frac{\partial U_i}{\partial x_i}\right)\right] + \frac{\partial}{\partial x_j}(-\rho\overline{u_i' u_j'}). \tag{4.35}$$

The equation is usually referred to as the Reynolds-Averaged Navier-Stokes equation (RANS or RANSE).

The term $-\rho\overline{u_i' u_j'}$ is the Reynolds stress tensor and must be modeled. The Boussinesq hypothesis is the method employed to relate the Reynolds stresses to the mean velocity gradients,

$$-\rho\overline{u_i' u_j'} = \mu_t\left(\frac{\partial U_i}{\partial x_j} + \frac{\partial U_j}{\partial x_i}\right) - \frac{2}{3}\left(\rho k + \mu_t\frac{\partial U_i}{\partial x_i}\right)\delta_{ij}, \tag{4.36}$$

where μ_t is the dynamic turbulent viscosity and k is the Turbulent Kinetic Energy (TKE).

The equation (4.36) is replaced in the equation (4.35) which, finally, is expressed by

$$\frac{\partial}{\partial t}(\rho U_i) + \frac{\partial}{\partial x_j}(\rho U_i U_j) = -\frac{\partial P}{\partial x_j} + \frac{\partial}{\partial x_j}\left[(\mu + \mu_t)\left(\frac{\partial U_i}{\partial x_j} + \frac{\partial U_j}{\partial x_i} - \frac{2}{3}\delta_{ij}\frac{\partial U_i}{\partial x_i}\right)\right] - \frac{2}{3}\frac{\partial}{\partial x_j}(\rho k). \tag{4.37}$$

4.6 Turbulence modeling

There are several approaches that allow the estimation of these effects. Spalart-Allmaras, k-ε and k-ω are common models that employ the Boussinesq hypothesis. In this study, the realizable k-ε turbulence model is adopted.

4.6.1 Realizable k-ε model

Is a two-equation turbulence model widely adopted. Initially is developed by Launder and Spalding (1972) in standard form and is based on the model transport equations for TKE and the dissipation rate ε. Later, Yakhot *et al.* (1992) refined this model (called RNG k-ε). Finally, this model was improved by Shih *et al.* (1995), called Realizable k-ε, and is described by

$$\frac{\partial}{\partial t}(\rho k) + \frac{\partial}{\partial x_j}(\rho k U_j) = \frac{\partial}{\partial x_j}\left[\left(\mu + \frac{\mu_t}{\sigma_k}\right)\frac{\partial k}{\partial x_j}\right] + P_k + P_b - \rho\varepsilon - Y_M + S_k, \tag{4.38}$$

$$\frac{\partial}{\partial t}(\rho \varepsilon) + \frac{\partial}{\partial x_j}(\rho \varepsilon U_j) = \frac{\partial}{\partial x_j}\left[\left(\mu + \frac{\mu_t}{\sigma_\varepsilon}\right)\frac{\partial \varepsilon}{\partial x_j}\right] + \rho C_1 S\varepsilon - \rho C_2\frac{\varepsilon^2}{k + \sqrt{\nu\epsilon}} + C_{1\varepsilon}\frac{\varepsilon}{k}C_{3\varepsilon}P_b + S_\varepsilon \tag{4.39}$$

where

$$C_1 = \max\left[0.43, \frac{\eta}{\eta+5}\right], \qquad \eta = S_1\frac{k}{\varepsilon}, \qquad S_1 = \sqrt{2S_{ij}S_{ij}}. \tag{4.40}$$

P_k represents the generation of TKE due to the mean velocity gradients,Y_M represents the contribution of the fluctuating dilatation in compressible turbulence to the overall dissipation rate, S_k and S_ε are user-defined source terms. P_k and μ_t are given by

$$\mu_t = \rho C_\mu \frac{k^2}{\varepsilon}, \tag{4.41}$$

$$P_k = -\rho\overline{u_i'u_j'}\frac{\partial U_j}{\partial x_i}. \tag{4.42}$$

The physic interpretation of C_μ, Y_M and the constant $C_{3\varepsilon}$ are given in Shih *et al.* (1995) and ANSYS (2017). The model constants $C_{1\varepsilon}$, C_2, σ_k and σ_ε have the following default values: $C_{1\varepsilon} = 1.44$, $C_2 = 1.9$, $\sigma_k = 1.0$ and $\sigma_\varepsilon = 1.2$.

4.7 Volume of Fluid method

The Volume of Fluid (VOF) is a method that can model immiscible[5] fluids for tracking and locating the free surface. Initially, the method was developed by Noh and Woodward (1976) and later by Hirt and Nichols (1981).

In the Figure 4.4a shows an example of a interface between two fluids with an actual shape and the Figure 4.4b is illustrated an approximation to the reconstruction of interface of the fluids in a grid mesh of a computational domain. Each cell indicates the fill rate of a fluid (material 1). The volume fraction of a fluid q is denoted by α_q and is defined as

$$\alpha_q = \frac{V_q}{V} \tag{4.43}$$

where V_q is the volume of a fluid in the cell and V is the volume of the cell. The volume fractions of two fluids in a cell must sum up to one

$$\sum_{q=1}^{N_{\text{fluids}}} \alpha_q = 1 \tag{4.44}$$

where N_{fluids} is the total number of fluids.

For each cell of the volume fraction follows three conditions:

- $\alpha_q = 0$, the cell is empty (of the q^{th} fluid);

[5] Incapable of mixing or attaining homogeneity (Merriam-Webster, 2004).

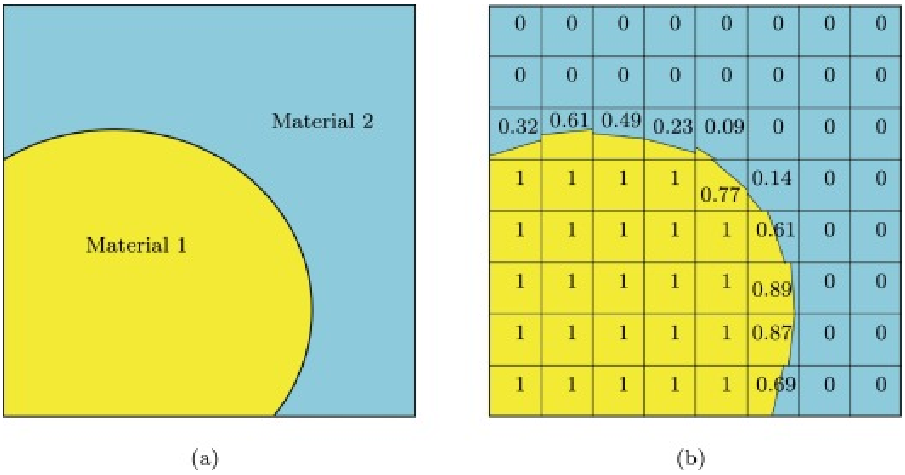

Figure 4.4: An example of VOF method, where shows the interface between two fluids (a) and is the approximation of the fluid interface in a grid mesh of a computational domain (b). Source: Pathak and Raessi (2016).

- $\alpha_q = 1$, the cell is full (of the q^{th} fluid);
- $0 < \alpha_q < 1$ The cell contains the interface between the q^{th} fluid and the other fluid.

The density and viscosity applying VOF method for each cell can be computed as

$$\rho = \sum_{q=1}^{2} \alpha_q \rho_q \tag{4.45}$$

$$\mu = \sum_{q=1}^{2} \alpha_q \mu_q \tag{4.46}$$

4.8 Implementation of boundary conditions

Generally, all CFD problems define initial boundary conditions of a computational domain (Figure 4.5). The most common boundary conditions are: inlet, outlet, wall, and symmetry (VERSTEEG; MALALASEKERA, 2007).

4.8.1 Inlet boundary condition

The total pressure at inlet boundary conditions is given by

$$p_{\text{in}} = \frac{1}{2}\mathbf{U}_{\text{in}}^2 + (\rho - \rho_0)|\overrightarrow{g}|[\widehat{g} \cdot (\mathbf{b} - \mathbf{a})] \tag{4.47}$$

where $\mathbf{a}$ is any point on the free surface and $\mathbf{b}$ is the position vectors in the center of the surface of an element, $\mathbf{U}_{\text{in}}^2$ is a mean velocity vector at inlet boundary condition, $|\overrightarrow{g}|$ is

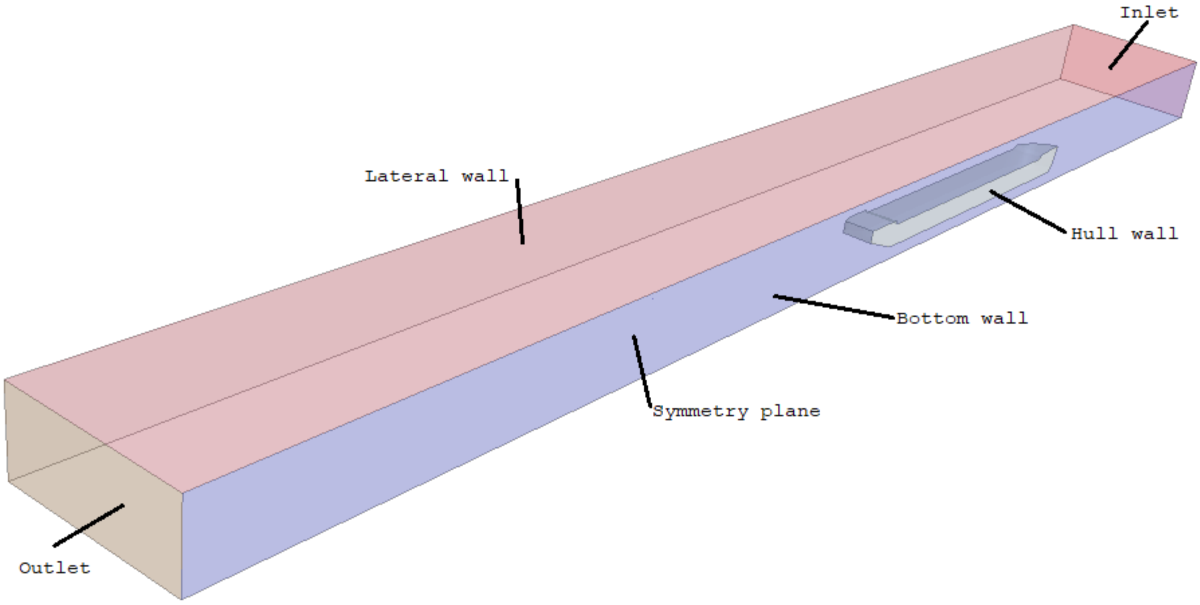

Figure 4.5: Boundary domain to imposes the boundary conditions in a control-volume. Source: Author.

the gravity magnitude, $\widehat{g}$ is the unity vector of gravity, and ρ_0 is the reference density.

The approximation of the TKE and ε at inlet are represented by (VERSTEEG; MALALASEKERA, 2007; ANSYS, 2017)

$$k_{\text{in}} = \frac{3}{2}(\mathbf{U}_{\text{in}} I)^2, \tag{4.48}$$

$$\varepsilon_{\text{in}} = C_\mu \frac{\rho k^2}{\mu} \left(\frac{\mu_t}{\mu} \right)^{-1}, \tag{4.49}$$

where C_μ is an empirical constant specified in the turbulence model (determined in the section 4.6). I is the turbulence intensity, defined as the ratio of the velocity fluctuations u_i' to the mean flow velocity U_i, represented by

$$I \equiv \frac{u_i'}{U_i}. \tag{4.50}$$

The turbulent viscosity ratio $\frac{\mu_t}{\mu}$ is directly proportional to the turbulent Reynolds number

$$Re_t \equiv \frac{k^2}{\varepsilon \nu}, \tag{4.51}$$

and the turbulence parameters are: $1 < \frac{\mu_t}{\mu} < 10$.

4.8.2 Outlet boundary condition

The pressure at outlet boundary condition is taken equal to the static or atmospheric pressure

$$p_{\text{out}} = (\rho - \rho_0)|\overrightarrow{g}|(\widehat{g} \cdot (\mathbf{b} - \mathbf{a})). \tag{4.52}$$

The flow often reaches a fully developed state in the flow direction if the outlet of the computational domain is chosen far from geometric disturbance. Thus, we can put an exit surface assuming the gradients of all variables are equal to zero in the flow direction (LAUNDER; SPALDING, 1972; VERSTEEG; MALALASEKERA, 2007; DEWAN, 2011; JI, 2013). Thus,

$$\frac{\partial U_{\text{out}}}{\partial n} = 0, \qquad \frac{\partial k_{\text{out}}}{\partial n} = 0, \qquad \frac{\partial \varepsilon_{\text{out}}}{\partial n} = 0, \tag{4.53}$$

where U_{out}, k_{out} and ε_{out} are variables at outlet flow and n is the normal vector of the surface.

4.8.3 Wall boundary condition

The region near to the wall can be modeled by means of the near-wall treatment. This approach does not include the wall, where the no-slip condition is adopted, which can lead to unsatisfactory results for the k-ε turbulence model.

The no-slip condition implies that the velocity components and the gradients of the pressure, TKE and ε are equal to zero

$$U_{\text{wall}} \cdot \mathbf{n} = 0, \qquad \frac{\partial P_{\text{wall}}}{\partial \mathbf{n}} = 0, \qquad \frac{\partial k_{\text{wall}}}{\partial \mathbf{n}} = 0, \tag{4.54}$$

where $\mathbf{n}$ is the local coordinate normal to the wall. Also, the velocity fluctuation u_i' is zero. Thus, the value of TKE can be computed as (DURBIN; Pettersson Rief, 2011; JI, 2013)

$$k_{\text{wall}} = \frac{1}{2}\overline{|u_i'|^2} = 0. \tag{4.55}$$

The adoption of the k-ε turbulence model closes to the wall at High Reynolds Number (HRN). The law-of-the-wall for mean velocity and TKE on standard wall functions yields

$$u_Q^+ = \frac{U_Q}{u_\tau} = \frac{1}{\kappa}\ln(Ey_Q^+) \tag{4.56}$$

$$k_Q = \frac{u_\tau^2}{\sqrt{C_\mu}} \tag{4.57}$$

where u_Q^+ is the dimensionless velocity, y_Q^+ is the dimensionless distance from the wall (for $30 < y_Q^+ < 500$, it satisfies the equation in the logarithmic region), E is the empirical constant (wall roughness parameter), equivalent to 9.793 for smooth walls, κ is the von Kármán constant (equal to 0.4187), U_Q is the mean velocity of the fluid at the wall-adjacent cell centroid Q, y_Q is the distance from the centroid of the wall-adjacent cell to the wall $\mathbf{B}$ (Figure 4.6) and u_τ is the friction or shear velocity, represented as

$$u_\tau = \sqrt{\frac{\tau_{\text{wall}}}{\rho}} \tag{4.58}$$

where τ_{wall} is the shear stress at the wall.

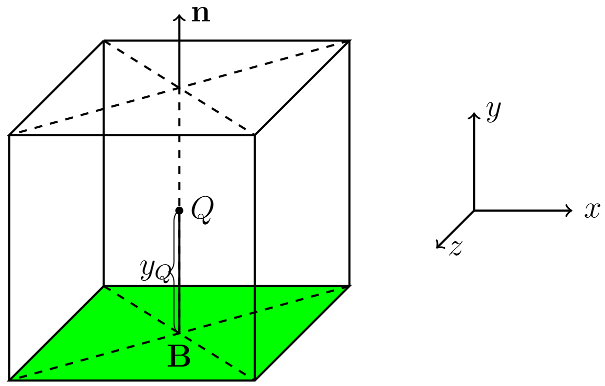

Figure 4.6: Calculation of distance y_Q between node Q and the surface on the wall $\mathbf{B}$. Source: Ji (2013).

For k-ε model, the wall function developed by Launder and Spalding (1974) is different. In order to avoid confusion in the nomenclature, the equation (4.56) according to y_Q^+ for k-ε model and its variables are represented by

$$u_Q^* = \frac{1}{\kappa}\ln(Ey_Q^*) \tag{4.59}$$

$$y_Q^* = \frac{C_\mu^{\frac{1}{4}}\sqrt{k_Q}}{\nu} \tag{4.60}$$

where ν is the kinematic viscosity of the fluid. The equations (4.56) and (4.59) (that correspond to the logarithm-law) are adopted when $\log y_Q^+$ and $\log y_Q^*$ present values larger that 11.225. Otherwise, the relationships between u_Q^+ and y_Q^+ (also u_Q^* and y_Q^*) are expressed by

$$u_Q^+ = y_Q^+ \qquad\qquad u_Q^* = y_Q^*. \tag{4.61}$$

as illustrated in the Figure 4.7, where the plot is divided in three sub-regions: viscous sub-layer ($y+ < 5$), buffer layer ($y+ < 30$), and log-law layer ($30 \leq y+ \leq 500$).

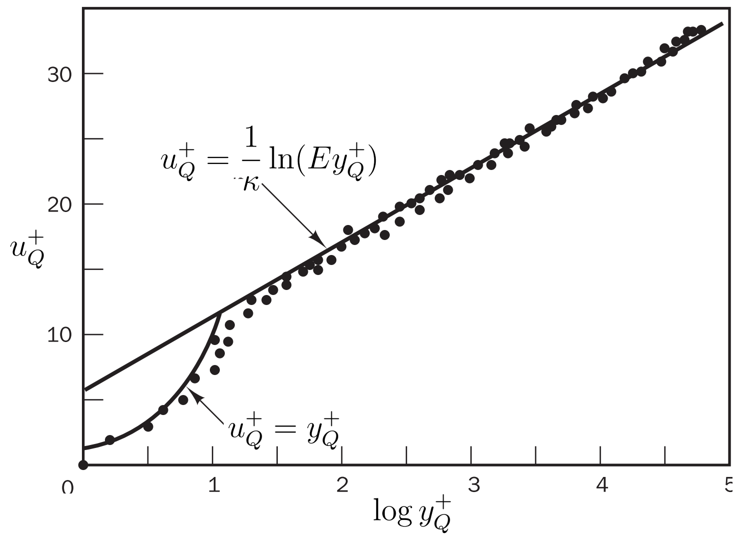

Figure 4.7: Velocity distribution near a solid wall. Source: Schlichting (1979); Versteeg and Malalasekera (2007).

The production of the kinetic energy P_k and the dissipation rate ε at the wall-adjacent cells are

$$P_k \approx \tau_{\text{wall}} \frac{\partial U}{\partial y} = \tau_{\text{wall}} \frac{\tau_{\text{wall}}}{\kappa \rho C_\mu^{\frac{1}{4}} k_Q^{\frac{1}{2}} y_Q}, \tag{4.62}$$

$$\varepsilon_Q = \frac{C_\mu^{\frac{3}{4}} k_Q^{\frac{3}{2}}}{\kappa y_Q}, \tag{4.63}$$

where τ_{wall} is the shear stress in the wall, formulated as

$$\tau_{\text{wall}} = \mu \frac{U_Q}{y_Q}. \tag{4.64}$$

At Low Reynolds Number (LRN), the equation (4.56) is not valid for $\log y_Q^+ < 11.225$ or $y_Q^+ < 30$, and the equations above mentioned for the wall boundary conditions cannot be used (VERSTEEG; MALALASEKERA, 2007).

4.8.4 Symmetry boundary condition

At this boundary condition, the gradients of all flow properties normal to the symmetry plane are taken equal to zero (DEWAN, 2011), i.e.,

$$\frac{\partial \mathbf{U}_{\text{sym}}}{\partial \mathbf{n}} = 0, \qquad \frac{\partial k_{\text{sym}}}{\partial \mathbf{n}} = 0, \qquad \frac{\partial \varepsilon_{\text{sym}}}{\partial \mathbf{n}} = 0, \tag{4.65}$$

where $\mathbf{U}_{\text{sym}}$, k_{sym} and ε_{sym} are variables located at symmetry plane.

4.9 Finite Volume Method

The Finite Volume[6] Method (FVM) is a numerical method of discretization[7] that allows solve partial differential equations (PDE) applied to conservation laws. Is similar to the Finite Element Method (FEM) or the Finite Difference Method (FDM) and uses integral formulations of conservation laws and does not require a structured grid mesh.

Consider the unsteady conservation equation for transport of a fluid property φ in a cell volume V as follows[8] (VERSTEEG; MALALASEKERA, 2007; CD-adapco, 2014)

$$\int_V \frac{\partial}{\partial t}(\rho\varphi)dV + \oint \rho\varphi\mathbf{u}\cdot d\mathbf{A} = \oint \mathit{\Gamma}_\varphi \nabla\varphi\cdot d\mathbf{A} + \int_V S_\varphi dV, \tag{4.66}$$

where $\mathbf{u}$ is the velocity vector, $\mathbf{A}$ is the surface area vector, $\mathit{\Gamma}_\varphi$ is the diffusion coefficient for φ, $\nabla\varphi$ is the gradient of φ and S_φ is the source of φ per unit volume. A practical interpretation of the equation (4.66) is provided in words (CD-adapco, 2014),

- The first term is time rate of change of fluid property φ inside the cell (transient term);
- The second term is the net rate of decrease of fluid property φ across the cell boundaries due to convection (convection term);
- The third term is the net rate of increase of fluid property φ across the cell boundaries due to diffusion (diffusion term);
- The fourth term is the generation/destruction of fluid property φ inside the cell (source term).

The Figures 4.8 and 4.9 show the position of the variables in each cell in a structured mesh in 2D. The pressure acts on the center p for each cell and the components of the velocities $u_{i,j}$ are evaluated in the center of the faces. The nomenclature is: O is the center of the cell; N, S, E, W are the center of the coordinates adjacent at north, south, east and west; n, s, e, w are points of the north, south, east and west center faces of the cell respectively.

[6] Finite volume refers to the element, cell or volume-control of a grid mesh.

[7] Set of small elements or cells.

[8] The second and third term (convection and diffusion) is rewritten as

$$\oint \rho\varphi\mathbf{u}\cdot d\mathbf{A} = \int_V \nabla\cdot(\rho\varphi\mathbf{u})dV = \int_{\mathbf{A}} \mathbf{n}\cdot(\rho\varphi\ \mathbf{u}\ )d\mathbf{A},$$

$$\oint \mathit{\Gamma}_\varphi\nabla\varphi\cdot d\mathbf{A} = \int_V \nabla\cdot(\mathit{\Gamma}_\varphi\nabla\varphi)dV = \int_{\mathbf{A}} \mathbf{n}\ \cdot(\mathit{\Gamma}_\varphi\cdot\varphi)d\mathbf{A}.$$

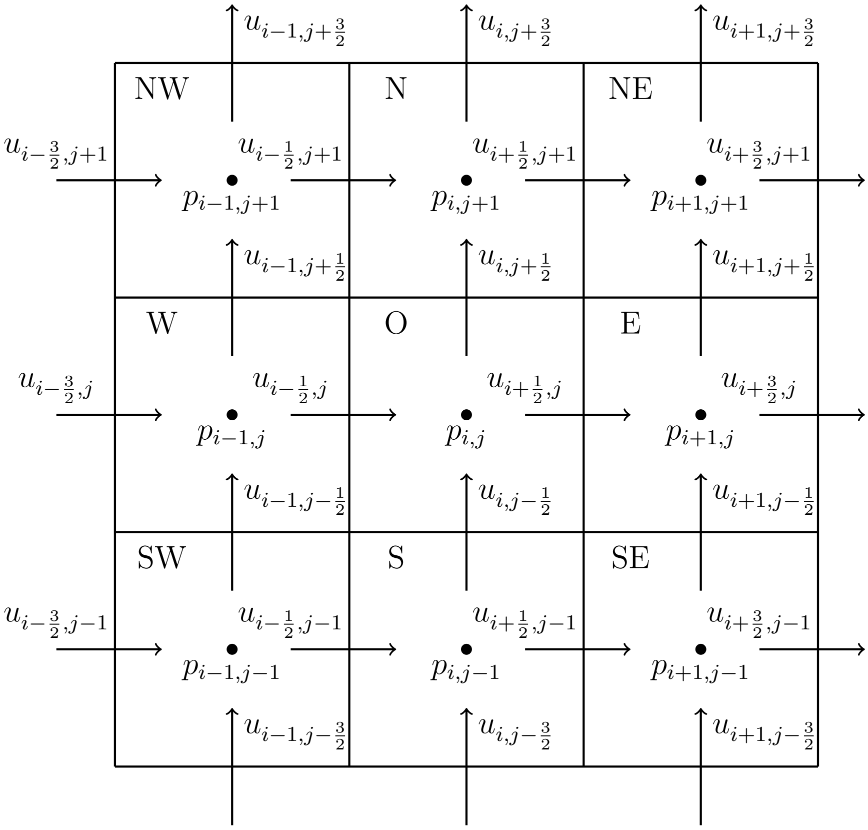

Figure 4.8: Positions of the variables for each cell in a structured mesh. Source: Author.

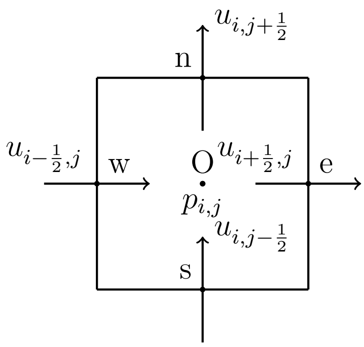

Figure 4.9: Positions of the variables of a cell in 2D. Source: Author.

In discrete form, each term of the equation (4.66) can be rewritten

$$\int_V \frac{\partial}{\partial t}(\rho\varphi)dV = \frac{\partial}{\partial t}\rho\varphi V, \tag{4.67}$$

$$\oint \rho\varphi\mathbf{u}\cdot d\mathbf{A} = \sum_f^{N_{\text{faces}}} \rho_f\mathbf{u}_f\varphi_f\cdot\mathbf{A}_f, \tag{4.68}$$

$$\oint \Gamma_\varphi\nabla\varphi\cdot d\mathbf{A} = \sum_f^{N_{\text{faces}}} \Gamma_\varphi\nabla\varphi_f\cdot\mathbf{A}_f, \tag{4.69}$$

$$\int_V S_\varphi dV = S_\varphi V. \tag{4.70}$$

Thus

$$\frac{\partial}{\partial t}\rho\varphi V + \sum_{f}^{N_{\text{faces}}} \rho_f \mathbf{u}_f \varphi_f \cdot \mathbf{A}_f = \sum_{f}^{N_{\text{faces}}} \mathit{\Gamma}_\varphi \nabla\varphi_f \cdot \mathbf{A}_f + S_\varphi V, \tag{4.71}$$

where N_{faces} is the number of faces enclosing each cell, φ_f is the value of φ convected through face f, $\rho_f \mathbf{u}_f \cdot \mathbf{A}_f$ is the mass flow through the face[9], $\mathbf{u}_f$ is the velocity vector through the face, $\mathbf{A}_f$ is the area of face f and $\nabla\varphi_f$ is the gradient of φ at face f. The terms of the transport equation are explained in the following subsections except for source term expressed in the equation (4.70) which is the simplest formulation consistent with a second-order discretization (CD-adapco, 2014).

4.9.1 Transient term

The transient term could be discretized temporally. First-order temporal discretization scheme (Euler implicit form) is used in this study. This involves the integration over a time step Δt and is given by

$$\frac{\partial}{\partial t}\rho\varphi V = \frac{(\rho\varphi V)^{n+1} - (\rho\varphi V)^n}{\Delta t}, \tag{4.72}$$

where $n+1$ is the next time level $t + \Delta t$, n is the current time level t.

4.9.2 Convection term

In this subsection, an explanation is provided regarding only one type of interpolation using spatial discretization schemes applied to the convection term. In the Figure 4.10 a one-dimensional form is illustrated. The integration of the total flux of the convection term, viewed in the equation (4.68), is rewritten as

$$\sum_{f}^{N_{\text{faces}}} \rho_f \mathbf{u}_f \varphi_f \cdot \mathbf{A}_f = \sum_{f}^{N_{\text{faces}}} (\dot{m}\varphi)_f = (\dot{m}_f\varphi)_e - (\dot{m}_f\varphi)_w. \tag{4.73}$$

4.9.2.1 2nd order upwind scheme

The scheme depends on the flow direction and is used in this study. Also, it is less dissipative but not bounded. In the Figure 4.10 shows the value φ of a fluid property

[9] The mass flow rate measures the mass of the fluid passing a point in the system per unit time. Is calculated as

$$\dot{m} = \rho\dot{V} = \rho\mathbf{u} \cdot A$$

where $\dot{V}$ is the volume flow rate.

obtained by means of a 2nd order upwind extrapolation. The estimation of φ on east face of a finite volume can be computed

$$\varphi_e \approx \begin{cases} \frac{3}{2}\varphi_O - \frac{1}{2}\varphi_W & \text{if } u > 0, \\ \frac{3}{2}\varphi_E - \frac{1}{2}\varphi_{EE} & \text{if } u \leq 0, \end{cases} \tag{4.74}$$

assuming a regular mesh (i.e. Δx is constant).

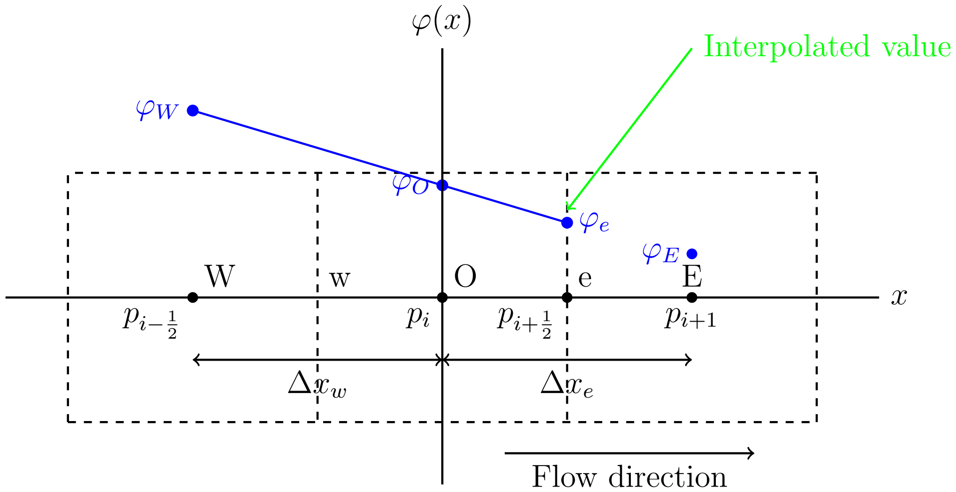

Figure 4.10: Interpolation profile of the 2nd Order Upwind Scheme. Source: Iaccarino (2004).

This discretization scheme was described initially for finite difference discretization by Warming and Beam (1976) and Hodge, Stone and Miller (1979). Later, it was implemented for finite volume by Tamamidis and Assanis (1993) as an explicit transient scheme, and by Thompson and Wilkers (1982) as a steady state implicit version (NORRIS, 2000).

4.9.3 Diffusion term

The diffusion term uses the interpolation function of central differentiating and does not cause stability problems to the simulation (MALISKA, 1995; CD-adapco, 2014; ANSYS, 2017). The integration of the total flux of diffusion, expressed in the equation (4.69), is rewritten as

$$\sum_{f}^{N_{\text{faces}}} \mathit{\Gamma}_\varphi \nabla \varphi_f \cdot \mathbf{A}_f = (\mathit{\Gamma}_\varphi A_f)_e \frac{\varphi_E - \varphi_O}{\Delta x_e} - (\mathit{\Gamma}_\varphi A_f)_w \frac{\varphi_O - \varphi_W}{\Delta x_w}. \tag{4.75}$$

In *STAR-CCM+*, the secondary gradient (or cross-diffusion) contribution is used, essential for maintaining accuracy on non-orthogonal meshes (CD-adapco, 2014).

4.10 Numerical procedure

The Semi-Implicit Method for Pressure Linked Equations (SIMPLE) is used to complement the numerical procedure that is described in the Figure 4.11. This method, developed by Patankar and Spalding (1972), is a segregated algorithm of iterative procedure for the calculation of pressure and velocity fields (VERSTEEG; MALALASEKERA, 2007). The flowchart of this procedure illustrates the following steps:

1. Read initial data;
2. Discretize and solve RANS equation using updated values of pressure to compute the intermediate velocity field;
3. Discretize and solve the pressure correction using the intermediate velocity field obtained recently;
4. Correct the pressure and the velocity field using the pressure-correction obtained in the previous step;
5. Discretize and solve scalar equation φ;
6. Return to step 2 in case of converges;
7. If the current time simulation is different to the maximum time simulation, return to step 2.

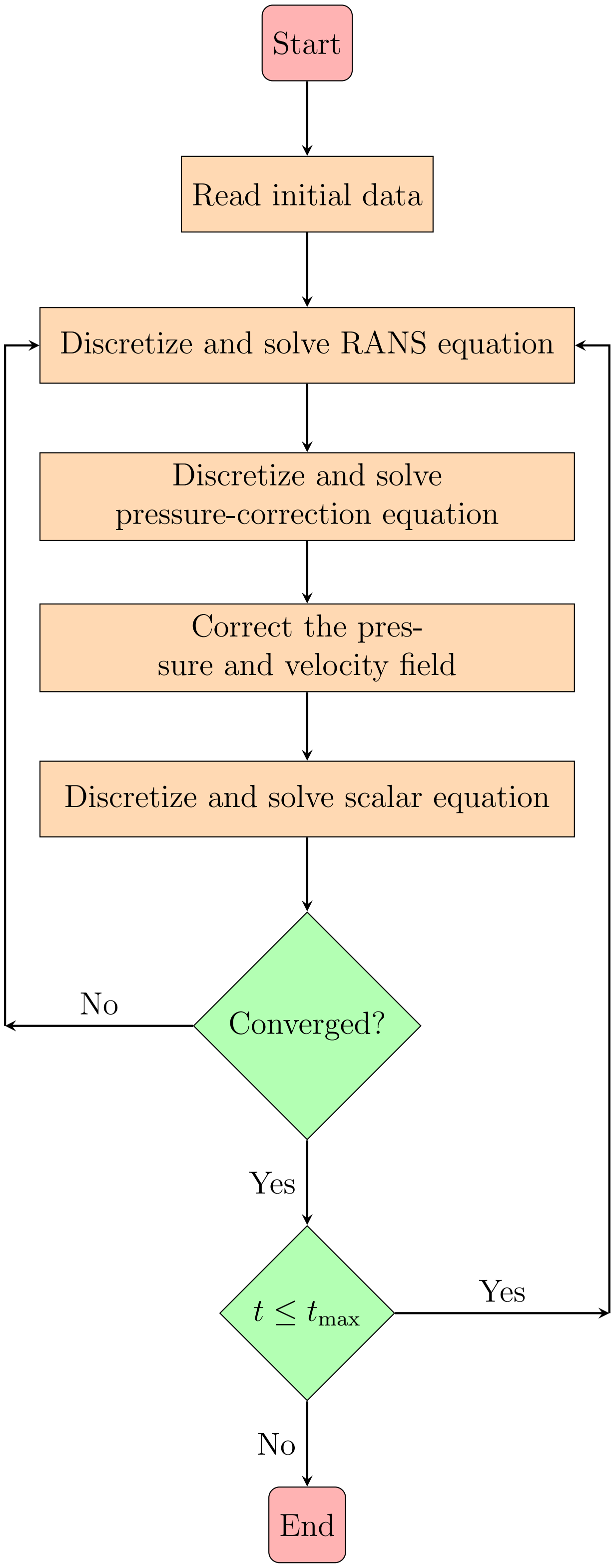

Figure 4.11: Numerical procedure in the *STAR-CCM+* solver. Source: Author.

5 APPLICATION TO THE SELF-PROPELLED INLAND VESSEL INTENDED FOR THE OPERATION IN THE MAGDALENA RIVER LOW COURSE

This chapter presents the methodology applied on the ship resistance calculation. For this purpose, a model which was tested and provided by the IPT was used. This model was digitally modeled and, subsequently, was carried out a comparative analysis based on the original IPT model and the CAD modeled hull. In this study, the mesh applied for the geometry, the boundary conditions and the solver parameters, as well as the results are presented and visualized.

5.1 Methodology

In the method, the market in which the vessel will operate, the physical restrictions of the river and the data obtained from existing inland vessels are considered. Once the hull design is chosen, the hull resistance is calculated by three ways. The first is the experimental test evaluated in the towing tank on IPT. The second is the empirical procedure (explained in the chapter 3) and is accomplished inside the parameters. The third is the procedure using CFD (Figure 5.1). The mesh is generated with the design of the geometry domain. Later, initial physical conditions are configured. Before running the solution (explained in the chapter 4), the time step and the maximum simulation time must be determined. After that, the results are analyzed and the experimental results are compared to the empirical results. The above are described in the Figure 5.2.

5.2 Experimental test in model scale

Consists of placing the model in a towing tank with a carriage that travels along the basin. The Figure 5.3 shows an example of a test of an inland vessel in shallow water

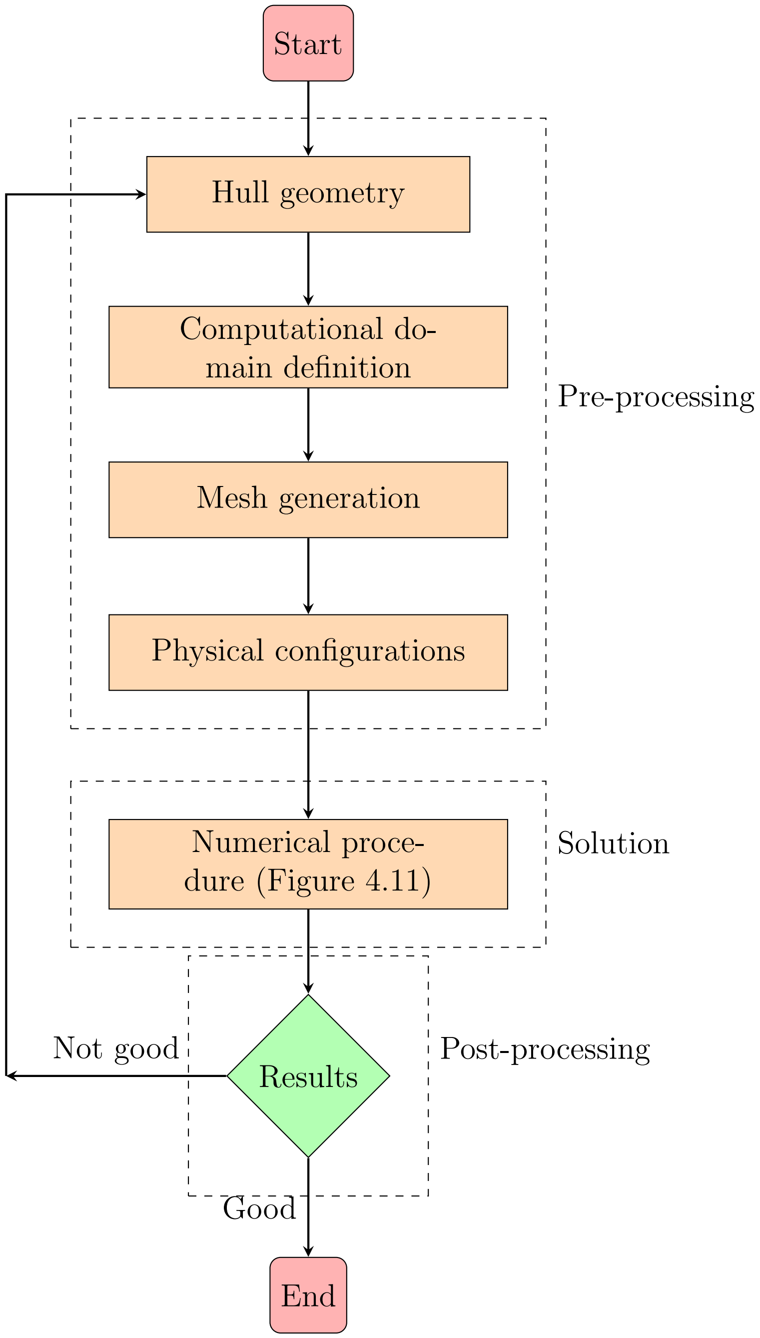

Figure 5.1: CFD procedure. Source: Author.

condition realized at Ghent University.

The geometrical and physical properties must be extrapolated to real scale. The way to do that is the similitude analysis that is composed by three aspects: geometric, kinematic and dynamic.

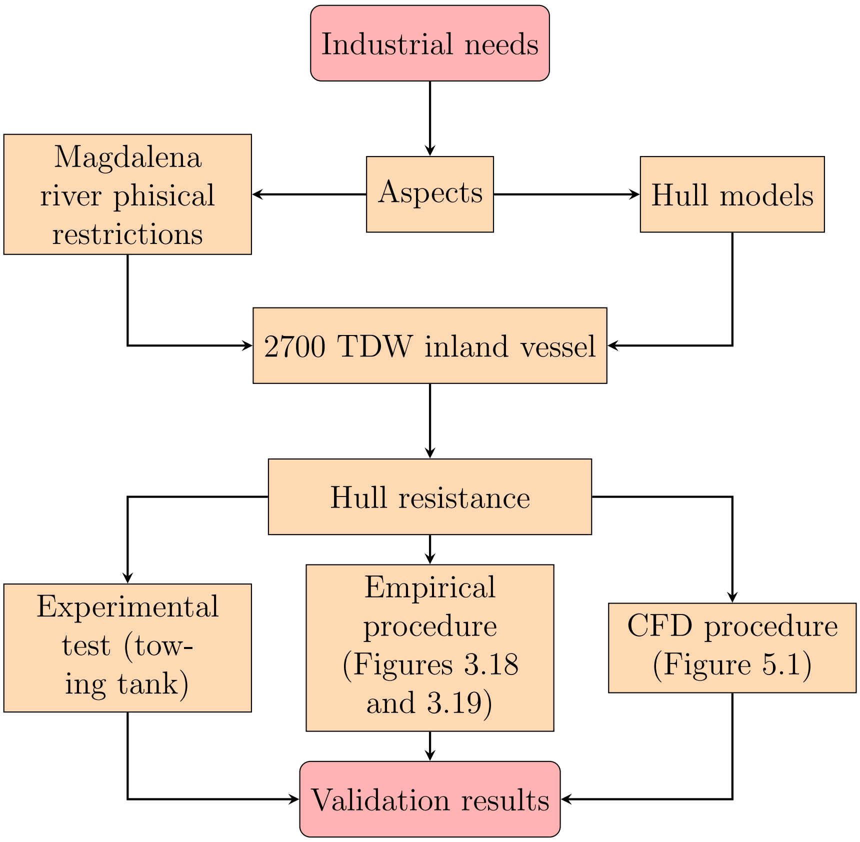

Figure 5.2: General methodology. Source: Author.

(a) General view of the towing tank

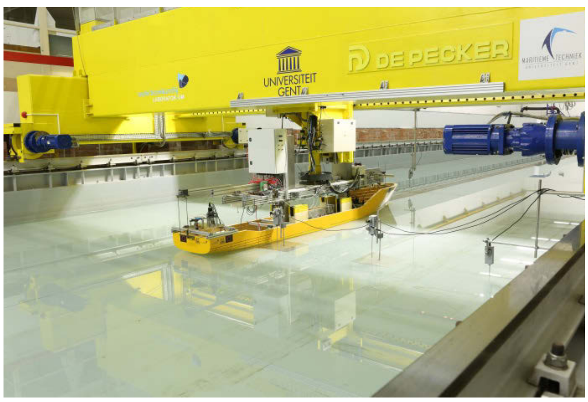

(b) General layout

Figure 5.3: Resistance test in shallow water condition at Ghent University. Source: Delefortrie, Geerts and Vantorre (2016).

5.2.1 Geometric similarity

Consists of two objects (model and prototype) of different dimensions which are similar as these have the same scale ratio. This type of similarity is applied to objects with area and volume, such as a wing shown in the Figure 5.4. The scale ratio is defined as,

$$\Xi = \frac{d_p}{d_m}, \qquad \Xi^2 = \frac{d_p^2}{d_m^2}, \qquad \Xi^3 = \frac{d_p^3}{d_m^3}, \tag{5.1}$$

where d_p and d_m are the dimensional lengths of the prototype and the model respectively.

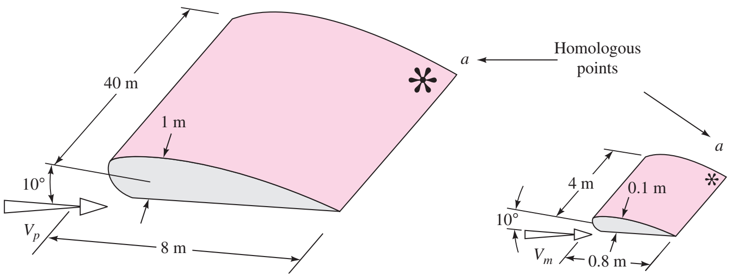

Figure 5.4: Example of geometric similarity in model testing. Left, prototype; right, scale model. Source: White (2011).

5.2.2 Kinematic similarity

The velocity of the flow at any point in the model must have the same direction as the velocity of the flow in the prototype. It means, the motions of the systems must be similar as illustrated in the Figure 5.5.

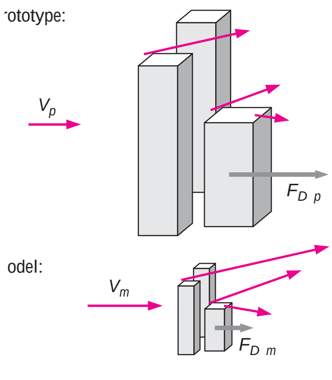

Figure 5.5: Example of kinematic similarity in model testing. Top, prototype; bottom, scale model. Source: Çengel and Cimbala (2006).

5.2.3 Dynamic similarity

The force and pressure coefficients of the model and prototype should be identical. It implies that the dimensionless parameters, such as Reynolds and Froude numbers, must be equal.

If the values of the Reynolds number are equal for different characteristic lengths of the prototype and the model, the velocity of the model will be high and, as a result, the evaluation in the towing tank will be impossible. On the other hand, the Froude number similarity could be used because the velocity of the model must be less than the velocity of the prototype. In the Figure 5.6 shows an experiment, where the prototype and model are identical homogeneous force.

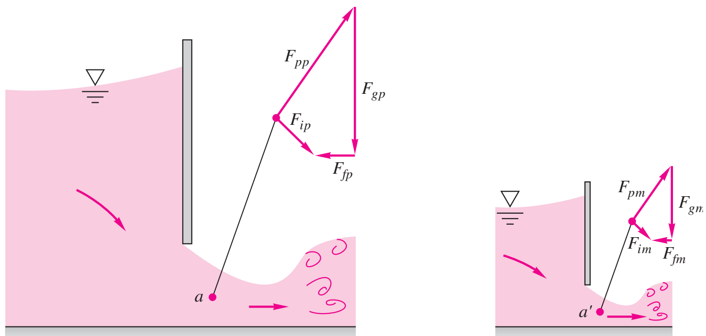

Figure 5.6: Example of dynamic similarity in model testing. Left, prototype; right, scale model. Source: White (2011).

5.3 Hull modeling

The hull geometry can be described through lines-plan. This plan is composed by the sheer profile (in perspective view which is divided in sections); the body plan (that shows the half symmetrical sections in the fore and aft); and the half-breadth plan (top view) which displays the half symmetrical sections (port and starboard side) at each waterline (levels of hull draft). In the Figure 5.7 illustrates an example of a lines-plan.

The offsets are the representation of the lines plan in numbers organized in tables (that provide the coordinates of the points the sum of which results in the formation of the hull's lines). The original hull model designed by IPT is composed by 137 sheers and 7 waterlines, described in the Figures B.1 and B.2. These offsets are adapted digitally, using the portable software FREE!ship (ENGELAND, 2006). This program uses a simple modeling, creating interpolation points for lines and the generation of surfaces, observed in Figure 5.8. Also, it was possible the analysis of the lines-plan that is generated digitally (Figure 5.9) and is compared with the original lines-plan of the hull, including their dimensions (Table 5.1).

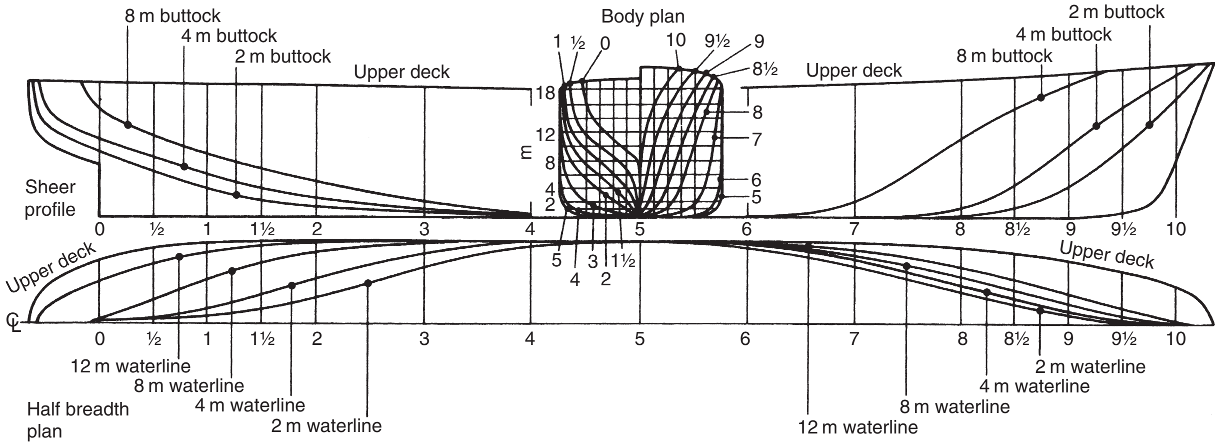

Figure 5.7: Example of a lines-plan. Source: Tupper (2004).

Variable	Model IPT	Model author	Difference (%)
L_{WL} (m)	4.193	4.203	-0.238
B (m)	0.725	0.725	0.000
T (m)	0.160	0.160	0.000
S_{ws} (m^2)	3.911	4.076	-4.048
Λ (m^3)	0.445	0.438	1.598

Table 5.1: Comparison of model hulls. Source: Author.

5.4 Geometry and mesh

Is important to define the volume of the computational domain for the simulation of inland vessel's resistance. The boundary condition of the symmetry is considered for the reduction of the computational process.

The size of the computational domain volume is one of the aspects that influence the simulation solution and the user defines the limits. If the computational domain is small, the flow is not represented and the simulation diverges. On the other hand, if the domain is larger, the simulation is consuming time and needs more power process without implying significantly better results.

In the Figure 5.10 shows the boundary conditions of the computational domain considered in this study and is similar to those used by Liu *et al.* (2017). The length is almost 4 times the L_{WL}, and the width of the IPT towing tank. The height is 0.8 m, where 0.3 m corresponds to the water depth. The geometry of this domain is described in the Table 5.2.

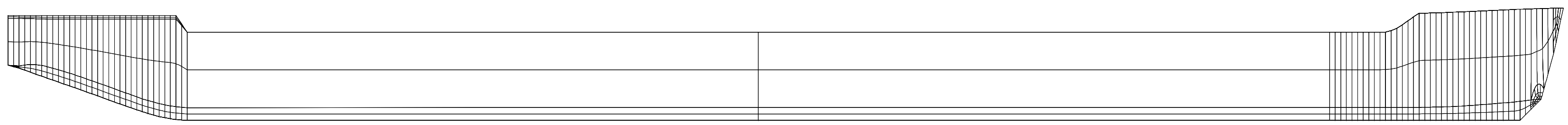

Figure 5.8: 2700 TDW hull modeled by author. Source: Author.

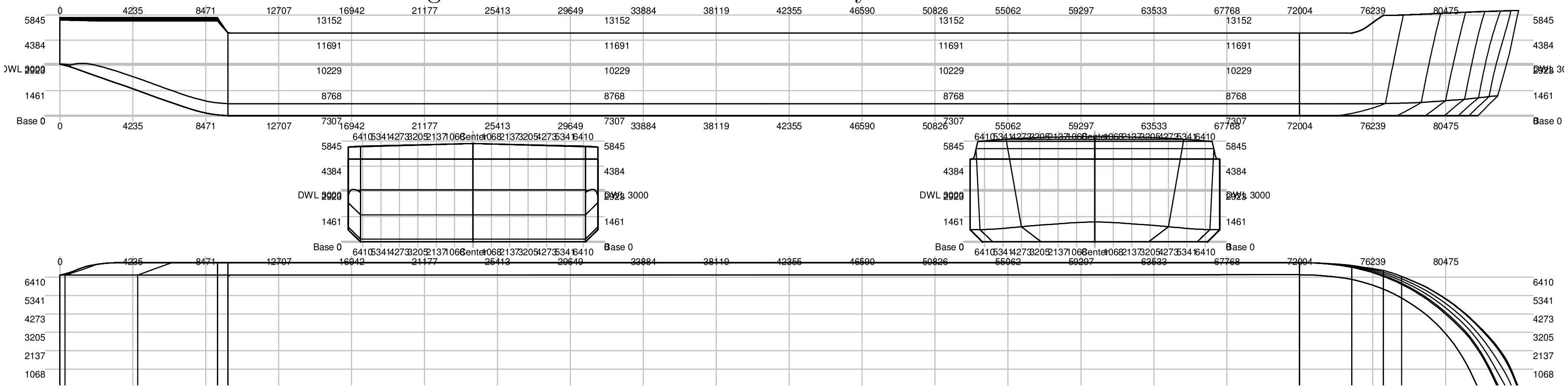

Figure 5.9: Lines-plan of 2700 TDW modeled by author. Source: Author.

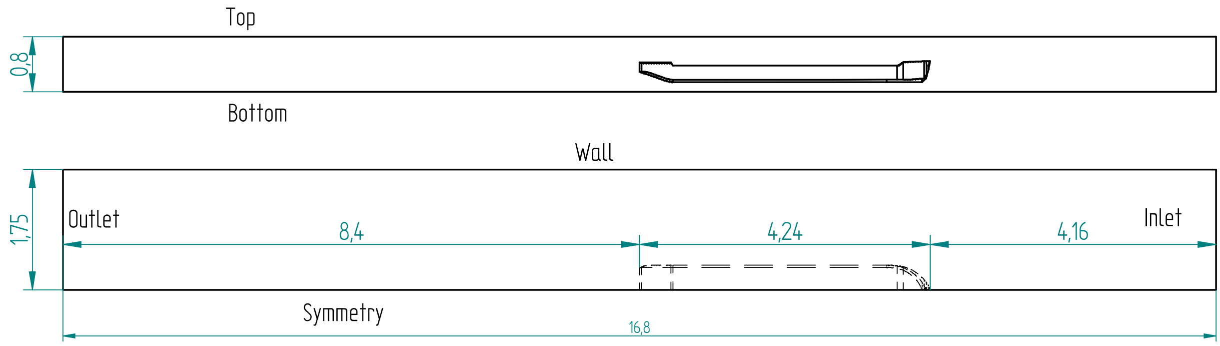

Figure 5.10: Boundary conditions of the domain. Source: Author.

	L_{WL}	**Dimension domain (m)**
Length of vessel	1.00	4.24
Behind	1.98	8.40
Forward	0.98	4.16
Side	0.41	1.75
High	0.19	0.80

Table 5.2: Dimensions of the computational domain geometry. Source: Author.

5.4.1 Mesh

After defining the geometry of the computational domain, the mesh is realized, which it is divided into surface mesh and volume. The *STAR-CCM+* (CD-adapco, 2014) software allows the creation of unstructured surface mesh and structured volume mesh.

For this study, it is important to discretize the regions of greatest interest, where the modification of the cell size is refined. The remainder of volume of the computational domain is maintained at base size of the cell. The regions around the hull are important because pressure and shear forces are obtained through the model, followed by the free surface due to the tracking of waves. Six regions of refined mesh are defined in the Table 5.3 and is illustrated in the Figure 5.11.

The advantages of the structured mesh are the algorithms of discretization and implementation in a computationally efficient manner. Their difficulties are the mesh generation of regions with multi-block shapes and the time required to produce a mesh for extremely complex forms in the computational domain (ANWER, 2016).

The base cell size, used for the computational domain, was 1.36 meters. For the vessel hull mesh, the isotropic prism (where the size of the cells side is equal) was used with 5.3125E-3 meters (base cell size divided 256 times), equivalent to 0.39%.

For the rest of the refined regions, the anisotropic prism is used. For the estimation

Region	Length (m)	Width (m)	Height (m)
Hull - Block	4.11	0.40	0.35
Hull - Cylinder	0.40	0.40	0.40
Bottom - Block	5.00	1.75	0.14
Bottom - Cylinder	1.75	1.75	1.75
Free surface - Thin	16.80	1.75	0.20
Free surface - Very thin	16.80	1.75	0.10

Table 5.3: Dimensions of refined regions. Source: Author.

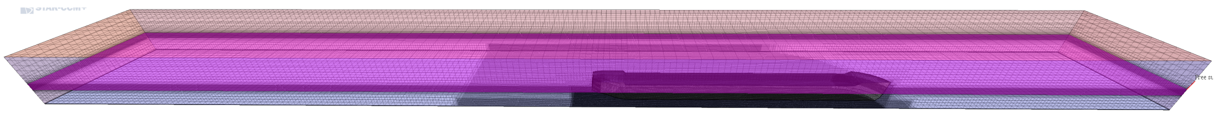

(a) Free surface zone

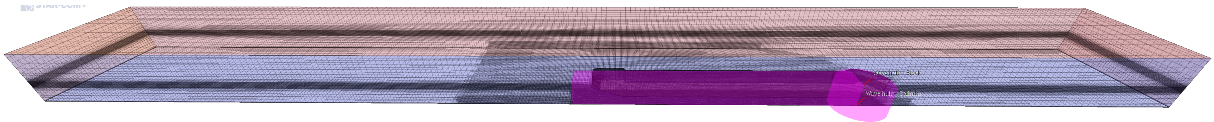

(b) Hull zone

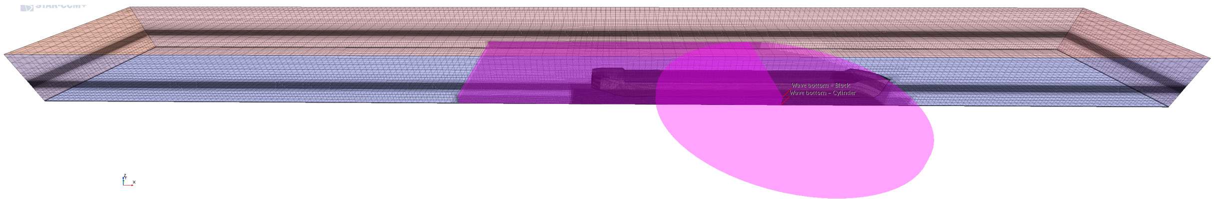

(c) Bottom zone

Figure 5.11: Refined mesh zones (in pink) in the computational domain. Source: Author.

of the cell size in the axes x and y for the free surface region, the wavelength λ generated by the inland vessel is calculated and is defined as (MOLLAND; TURNOCK; HUDSON, 2011)

$$v_{\text{model}}^2 = \frac{g\lambda}{2\pi} \tanh\left(\frac{2\pi h}{\lambda}\right). \tag{5.2}$$

Ji *et al.* (2012) recommends using 10 points per length of the transverse waves. The value of the cell size for both axes is 2.125E-2 meters, because the velocity reference is 0.576 m/s. The cell size in z axe applied on the bottom and free surface-thin regions is equivalent to 5.3125E-3 meters; the free surface in the very thin region is sized at 2.65625E-3 meters and allows tracking and locating the free surface using VOF method. The visualization of the computational domain mesh described above is illustrated in the Figures 5.12 and 5.13, similar to those by Liu *et al.* (2017), and the Table 5.4 is detailed the cell size of each region.

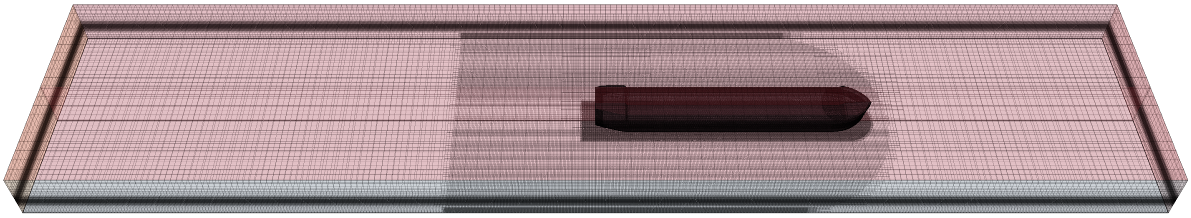

Figure 5.12: Overview of the mesh in the computational domain. Source: Author.

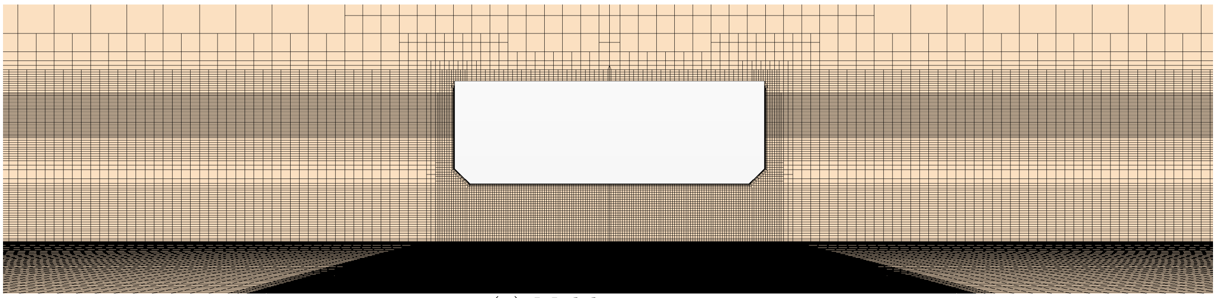

(a) Midship section

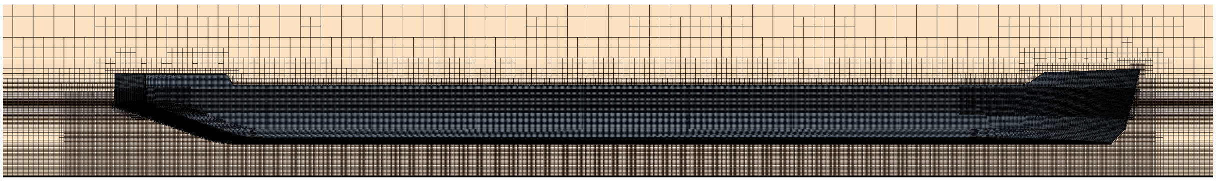

(b) Longitudinal section at symmetry

Figure 5.13: Grid structure around the vessel. Source: Author.

Region	**Trimmer**	**Cell size (m)** x	y	z
Hull - Block	Isotropic	5.31250E-3	5.31250E-3	5.31250E-3
Hull - Cylinder	Isotropic	5.31250E-3	5.31250E-3	5.31250E-3
Bottom - Block	Anisotropic	2.12500E-2	2.12500E-2	5.31250E-3
Bottom - Cylinder	Anisotropic	2.12500E-2	2.12500E-2	5.31250E-3
Free surface - Thin	Anisotropic	2.12500E-2	2.12500E-2	5.31250E-3
Free surface - Very thin	Anisotropic	2.12500E-2	2.12500E-2	2.65625E-3

Table 5.4: Configuration of the mesh in refined regions. Source: Author.

5.4.1.1 Boundary layer mesh

The boundary layer is important because the near-wall flow solution allows the determination of forces and flow features that depend on the velocity gradients (CD-adapco, 2014). In previous chapter it was explained how the near-all treatment works in the wall of the boundary condition and, in this study, is applied only on the hull vessel and on the wall bottom of the computational domain.

Some aspects are taken into account in the generation of prism mesh. One is the boundary thickness, and can be determined according to ITTC (2014),

$$y = \frac{y^+ L_{\text{mod}}}{Re_L \sqrt{\frac{C_f}{2}}}, \tag{5.3}$$

where L_{mod} is the length of the inland vessel model and Re_L is the Reynolds number of the ship model. The value corresponds only to the first thickness layer and the user chooses the value of $y+$. For the finite mesh, $y+ \leq 1$; and for tick mesh, $30 \leq y+ \leq 100$, equivalent to logarithmic profile. In *STAR-CCM+*, the *all y+ wall treatment* is chosen by default.

Another aspect is the stretch factor, that is represented as the ratio between the thickness of a cell layer and the thickness of the preceding layer. For example, the prism layer is 1 unit and stretch factor is 2, the thickness of the next layer is 2 units, continuing the other next layers that would give values of 4, 8, 16 and so on. An example is illustrated in the Figure 5.14. In appendix C, an algorithm generated in *MATLAB* is created to determine the total thickness prism layer. In the Figure 5.15 and the Table 5.5 are detailed the properties of the prism layer for the hull and wall bottom in the computational domain. The hull stern and hull deck are not applied, and do not affect the calculation of the resistance.

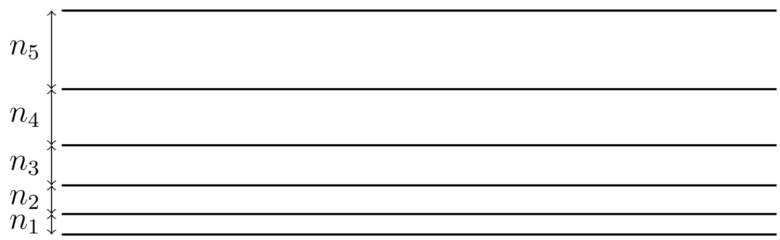

Figure 5.14: Representation of prismatic mesh for boundary layer. Source: Author.

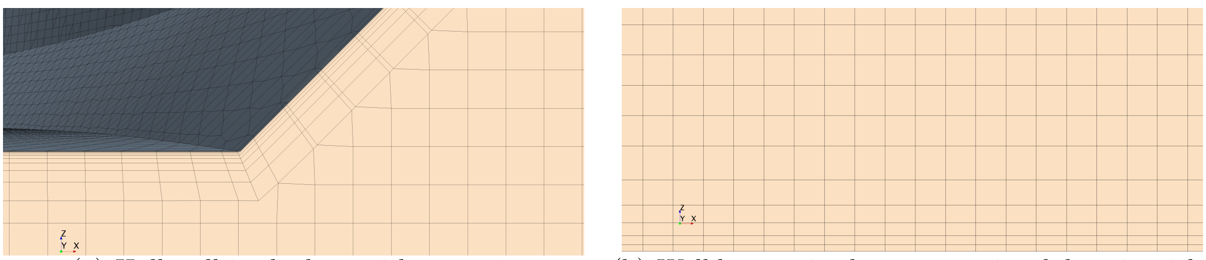

(a) Hull wall in the bow with $y+ = 1$

(b) Wall bottom in the computational domain with $y+ = 30$

Figure 5.15: Prism layer mesh. Source: Author.

Parameter	Hull vessel	Bottom domain
$y+$	1	30
First prism layer (m)	2.4994E-5	0.0011
Stretch factor	1.59	1.4
Number of layers	11	5
Total thickness layer	0.0069	0.00125

Table 5.5: Parameters of the prism layer of the mesh. Source: Author.

5.5 Boundary conditions

The settings for the boundary conditions must be carefully defined according to the test conditions made in the towing tank of the IPT. First, the VOF Waves for the simulation of the gravity waves on a light fluid and a heavy fluid interface are defined. Provides field functions that are used to initialize the VOF calculations (CD-adapco, 2014). In this study, the type of VOF Waves that will be used is *flat*, because represents a plane of calm water. In the Table 5.6 shows the properties of VOF Waves, where the *point on water level* defines the position of the water surface; the *vertical direction* represents the normal vector to the water surface; *current* is the velocity of the heavy fluid; *wind* is the velocity of the light fluid; *light and heavy fluid density* are required for the hydrostatic field function, created automatically with the waves, and the values for the water and the air are determined by default. The variable u stands for the velocity which gains four different values (0.576, 0.691, 0.806 and 0.921 m/s), for the calculation of the resistance, and its vector direction is negative. These configurations are visualized in the Figure 5.16. The heavy and the light fluids corresponds to the water and the air.

Variables	Value
Point on water level (m)	$[0.0, 0.0, 0.0]$
Vertical direction	$[0.0, 0.0, 1.0]$
Current (m/s)	$[-u, 0.0, 0.0]$
Wind (m/s)	$[-u, 0.0, 0.0]$
Light fluid density (kg/m^3)	1.18415
Heavy fluid density (kg/m^3)	997.561

Table 5.6: Properties of Flat VOF Wave on *STAR-CCM+*. Source: Author.

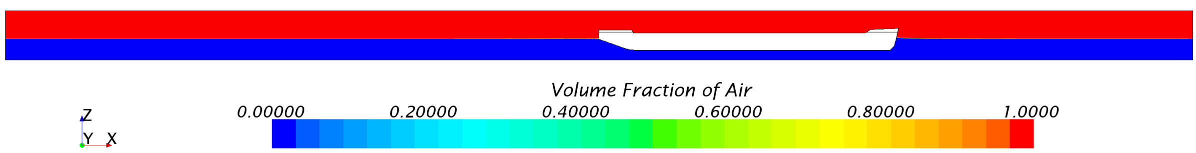

Figure 5.16: Free surface in *flat* state, with the volume fraction of water (blue) and air (red). Source: Author.

The boundary conditions of the computational domain are configured and detailed in the Table 5.7 and the Figure 5.10. The velocities are defined at inlet, wall banks, top and wall bottom and correspond to field function of Flat VOF Wave. A numerical damping with length of 8.5 m is applied at inlet and outlet planes to remove wave reflections and avoid the interaction of the true wave field generated by the vessel of the model, visualized in the Figure 5.17. The prism layer on bottom wall is configured only with $y+ = 30$ and the hull wall on stern and deck of the vessel is not applied.

Boundary	**Condition**	**Properties**
Inlet	Velocity inlet	Normal velocity with volume fraction of water and air. Damping wave reflections avoided.
Outlet	Pressure outlet	Volume fraction of water and air, Damping wave reflections avoided.
Wall banks	Wall	No-slip condition and motion: x-velocity.
Top	Velocity inlet	Volume fraction of water and air. Motion: x-velocity.
Bottom	Wall	No-slip condition and motion: x-velocity. Prism layer mesh with $y+ = 30$.
Symmetry	Symmetry	Default.
Vessel hull	Wall	No-slip condition and smooth wall (default).
Vessel stern and deck	Wall	No-slip condition and smooth wall (default). No prism layer.

Table 5.7: Boundary conditions properties configured on *STAR-CCM+*. Source: Author.

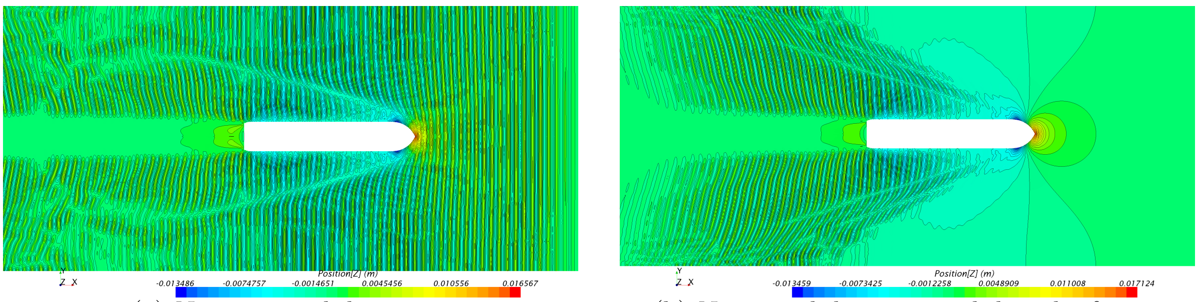

(a) No numerical damping (b) Numerical damping with length of 9 m

Figure 5.17: Numerical damping on *STAR-CCM+*, where no numerical damping (a) affects the true waves generated by the inland vessel model, unlike numerical damping with length of 8.5 m applied only at inlet and outlet boundary conditions (b). Source: Author.

5.6 Solver parameters, monitoring and plotting

Solver is defined by three parameters: time step, maximum iteration numbers and maximum physical time.

Time step could be determined by the Courant number, represented by

$$C_o = \frac{\upsilon \Delta t}{\Delta x} \tag{5.4}$$

where υ is the velocity of the fluid, Δt is the time step and Δx is the length interval. In this study, Δx is defined as 2.125E-2 m and υ is the minimum velocity of the vessel.

The Courant number must be less that or equal to 1. According to ITTC (2014) the equation of the time step is

$$\Delta t = 0.05 - 0.01 \frac{L_{\text{mod}}}{\upsilon}. \tag{5.5}$$

However, for flows in confined water, a significantly smaller time step introduced by Liu *et al.* (2017), which is used in this study, is represented as

$$\Delta t \leq 0.002 \frac{L_{\text{mod}}}{\upsilon}. \tag{5.6}$$

The definition of the maximum iteration number is not established. Checking the journal scientific papers, the average value of iteration is 10 per time step and is chosen in this study. The maximum physical time depends of the simulation results, where the variable of vessel resistance could be stable. Analyzing the results, 120 seconds is enough, as shown in the Figure 5.18. The total iteration process is completed after 80,000 iterations.

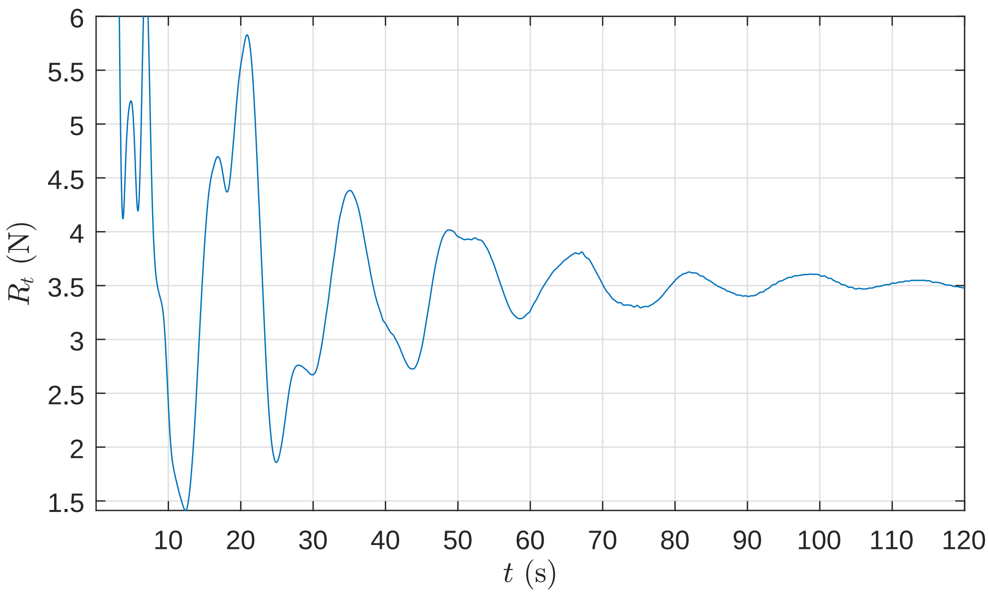

Figure 5.18: Physical time simulation of the 2700 TDW inland vessel performed on *STAR-CCM+* at $\upsilon = 0.576$ m/s. Source: Author.

Plots and visualization are analyzed for the interpretation of the results after the simulation is finished. The plot of the residuals is a convergence analysis and the smaller the residual values, the higher convergence of the simulation with the experimental results. The Figure 5.19 shown an example of the residuals, where is simulated the inland vessel at 0.921 m/s. Initially, the variables of the residuals start with values equal to 1. During process, some variables drop to three levels. The ideal is that all the variables must be in lower levels than $1 \cdot 10^{-2}$. Therefore, the results in CFD simulation could close the experimental results. The description of the residuals (continuity, x-movement, y-movement, z-movement, TKE, TDR and water) is contained in the Table 5.8.

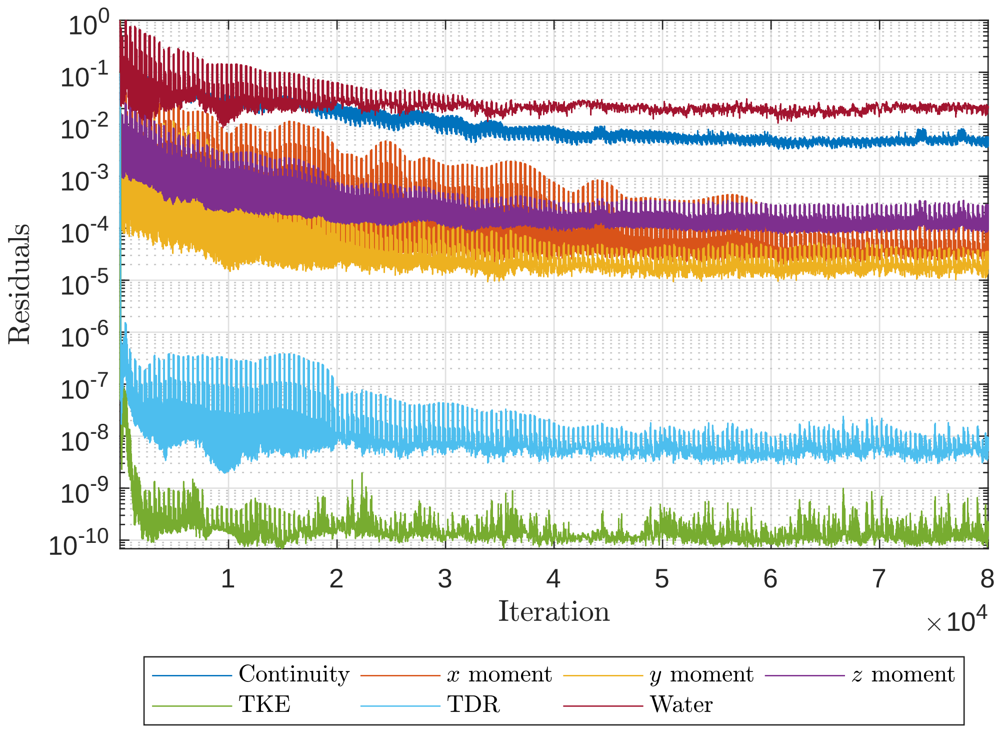

Figure 5.19: Plot of residuals of the 2700 TDW inland vessel performed on *STAR-CCM+* at $v = 0.921$ m/s. Source: Author.

Residual	**Description**
Continuity	How much left to close the continuity equations.
x moment	Quantity movement in x axis
y moment	Quantity movement in y axis
z moment	Quantity movement in z axis
TKE	Residuals referent to k parameter of the Reynolds average of the k-ε model turbulence
TDR	Residuals of the Turbulent Dissipation Rate.
Water	Oscillation of water on the simulation, generating wave system.

Table 5.8: Definition of residuals. Source: CD-adapco (2014).

5.6.1 Cluster specifications

For the execution of the numerical simulation, the cluster available on TPN is used. The cluster is a set of computers united that work together as a one computer. TPN clusters are based on GNU/Linux operating system. The specifications is described in the Tables 5.9 and 5.10. In this study, The SGI cluster is used for the numerical simulation and is executed 2 nodes with 40 cores and 256 GB of RAM memory. The total simulation CPU time for each velocity was 5.5 days.

Cluster SGI	
Total nodes	48.
Processor	Intel(R) Xeon(R) CPU E5-2680 v2 @2.80GHz, 10 cores. Total processors: 960. Total cores: 9600.
Total Teraflops	28.416 (theoretical), 21.000 (Linkpack).
RAM memory	128 GB per nodes. Total: 6 TB.
Storage	148 TB.

Table 5.9: SGI cluster specifications on TPN. Source: Author, in collaboration with TPN.

Cluster 1	
Blades	192 X6175 in water-cooled C48 racks delivering about 15 TFlops of processing.
Processor	Intel Nehalem 2.80GHz. Total cores: 1536.
RAM memory	4.5 TB.
Storage	150 TB.
Cluster 2	
Total servers	16 X4440
Processor	AMD Shangai 2.66GHz, 256 cores.
RAM memory	1 TB.
Total Teraflops	2 of generic processing and almost 30 of vector processing in simple precision.

Table 5.10: Sun microsystems (Oracle) cluster specifications on TPN. Source: Author, in collaboration with TPN.

Figure 5.20: TPN clusters. Source: Author.

5.7 Results

The comparisons between the empirical methods (for large and medium rivers) and the numerical methods with the experimental result are made and observed in the Figure 5.21, where the numerical method and the empirical method for medium rivers are accurately close to the experimental results.

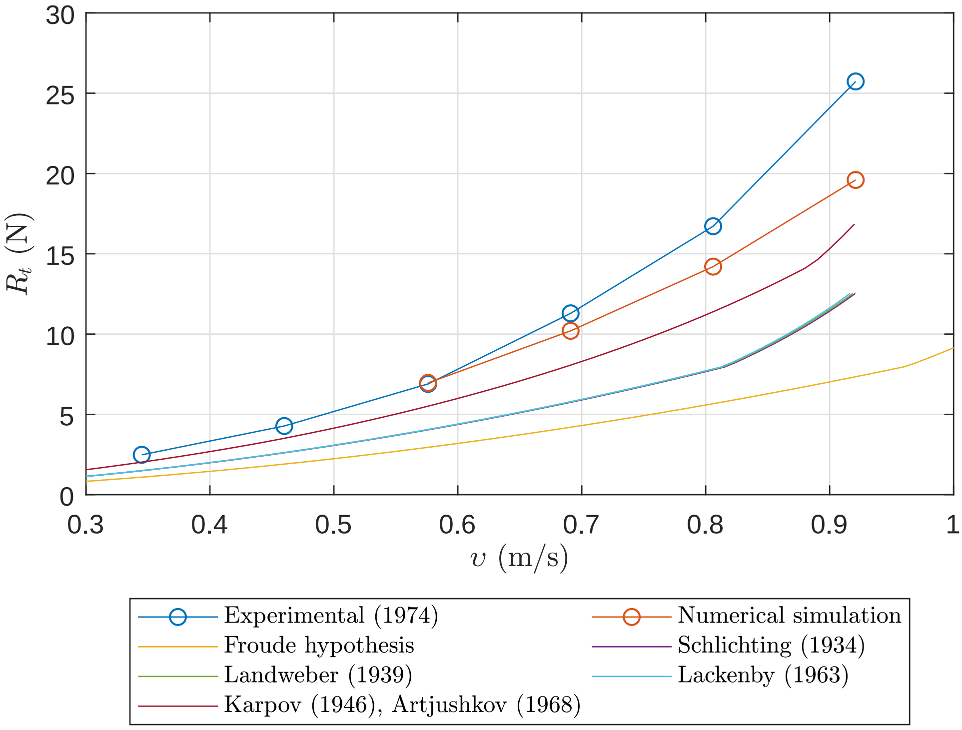

Figure 5.21: Comparison of methods with 2700 TDW inland vessel. Source: Author.

The values obtained from the application of empirical methods applicable for large river operation do not offer, in this study, an accurate prediction of the vessel resistance. The calculation of the coefficient forces are observed in the Figure B.5, where the frictional coefficient resistance are calculated with Reynolds number from $3.5{\cdot}10^{-3}$ to $1.7{\cdot}10^{-3}$. The residual resistance coefficient with infinite velocity is calculated, and the results is constant with $10^3C_r = 0.345$ with length Froude number values up to 0.15. From $Fr_L = 0.15$, 10^3C_r the values goes up to 3.5. The values of the loss in velocities (Figure B.4) using Schlichting's method are between 14.93% ($\upsilon_\infty = 0.345$ m/s) and 15.50% ($\upsilon_\infty = 0.921$ m/s). For Lackenby's method, the loss in velocities are between 15.21% and 15.90%. In the Figure B.6 are shown the comparison of the ship resistance, where the residuary resistance are more higher in shallow waters than in deep waters, because of various factors like the influence of the walls (lateral and bottom), high waves resistance values and other effects.

The values of the vessel resistance using empirical methods for medium rivers are in better agreement with the experimental results. The velocities v_1 and v_2 are calculated from Karpov's diagram (Figure B.7) and are higher than v_∞ (maximum of 12.5% approximately). In the Figure B.8 shows the coefficient forces for middle rivers. The values of the frictional resistance coefficient are higher in comparison with this variable for large rivers. The calculation of the residuary resistance coefficient is constant with value equal to 2.54 and from $Fr_L = 0.15$ this coefficient varies until 2.85. Raven (2012) affirms that the most used empirical methods to estimate shallow water resistance for inland vessels have a very weak theoretical and empirical basis. He recommends the development of new prediction methods that correct separately the components of the total resistance (LINDE *et al.*, 2017).

The results of the numerical method are more accurate at the beginning, but the velocity are higher and the discrepancies appear, described in the Table 5.11. The relative error is necessary to observe the discrepancy between the approximation values and the exact values, and is represented by

$$E_r = \frac{F_m - F_{\mathrm{CFD}}}{F_m} \tag{5.7}$$

where F_m is the model resistance that is tested experimentally and F_{CFD} is the resistance that is calculated numerically.

	R_t (N)			Relative error (%)	
v(m/s)	Experimental	CFD	Empirical	CFD	Empirical
0.576	6.8941	6.9600	5.8256	-0.9563	15.4988
0.691	11.2875	10.2000	8.5450	9.6342	24.2968
0.806	16.7105	14.2000	12.0895	15.0236	27.6533
0.921	25.7228	19.6000	17.8585	23.8031	30.5657

Table 5.11: Comparison of numerical and empirical method with experimental results. Source: Author.

The Figure 5.22 shows the numerical results of the hull resistance for each velocity and the behavior is the same. At the beginning, the values are higher and, over time, the resistances are stabilized around 100 seconds.

5.7.1 Verification of results

Four meshes with number of elements between 2,231,629 and 10,060,010 were used for the analysis of the grid dependence study simulated in *STAR-CCM+*. In the Table 5.12 is presented the number of the mesh and the total resistance of the inland vessel.

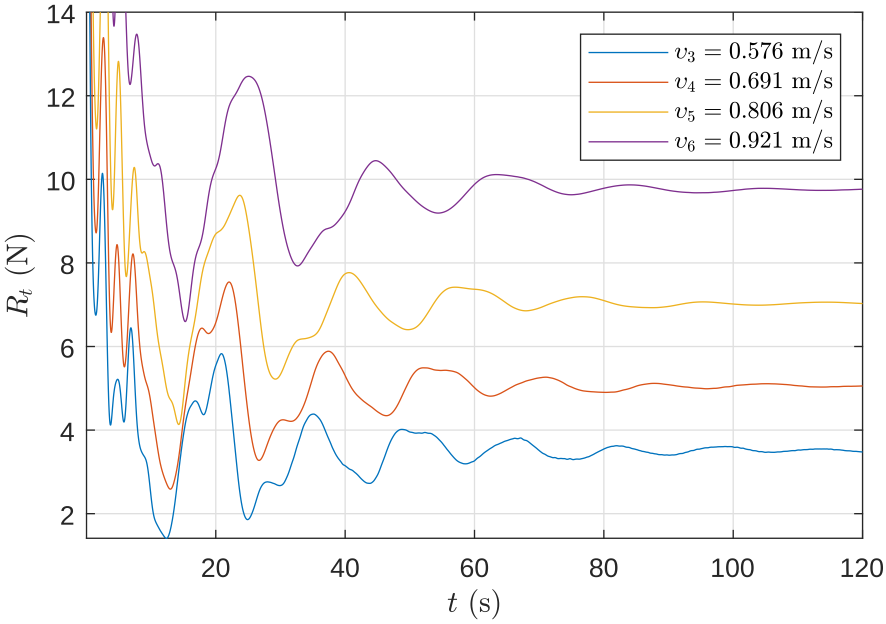

Figure 5.22: Total resistance results of 2700 TDW inland vessel calculated numerically, where the values are half of inland vessel vessel. Source: Author.

The calculation of the resistance for each mesh are shown in the Figure 5.23a, and the difference of the calculated values comparing to the mesh number 1 is illustrated in the Figure 5.23b.

Mesh number (N_i)	Number of cells	Total Resistance (R_t)
1	10 066 010	6.946
2	8 307 654	6.954
3	6 080 167	6.998
4	2 231 629	7.044

Table 5.12: Number of cell in the mesh used in the grid dependence study of 2700 TDW inland vessel at $v = 0.576$ m/s. Source: Author.

For the discretization errors, the Grid Convergence Index (GCI) will be used, developed by Roache (1998) and described by Celik *et al.* (2008). This method is recommended by American Society of Mechanical Engineers (ASME) and American Institute of Aeronautics and Astronautics (AIAA) (LINDE *et al.*, 2017).

Checking the articles where the method is used, a constant refinement ratio is represented in the equation (2.1). The fine grid (N_1) consist of approximately 10.07 million cells; the medium grid (N_2) contains about 8.31 million cells; and about 6.08 million cells in the coarse grid (N_3). The solution changes between two successive grids ι_{21} for

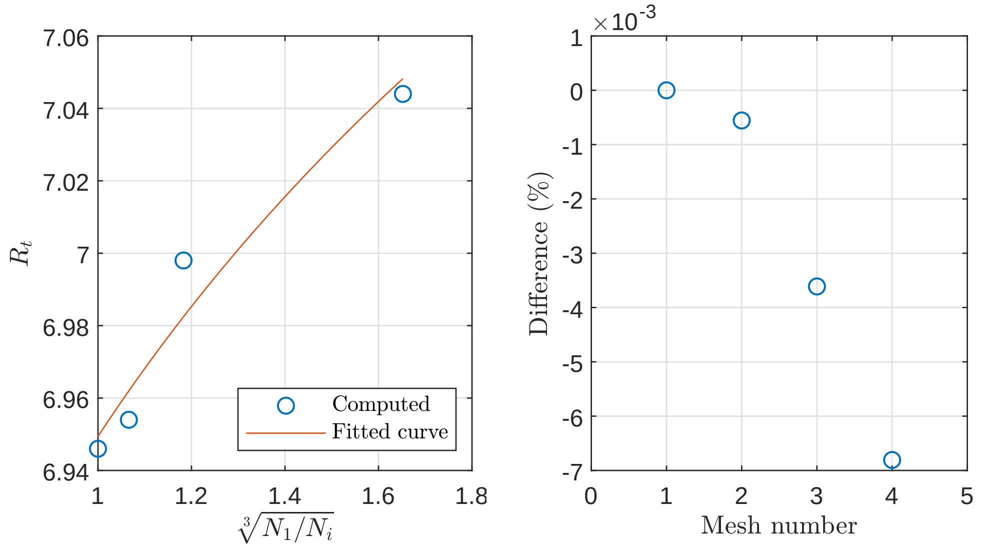

(a) Total resistance (b) Difference between the meshes

Figure 5.23: Convergence of the total resistance with grid refinement of the 2700 TDW inland vessel performed on *STAR-CCM+* at $\upsilon = 0.576$. Source: Author.

medium-fine meshes and ι_{32} for coarse-medium meshes are defined as

$$\iota_{32} = \phi_3 - \phi_2, \qquad \iota_{21} = \phi_2 - \phi_1, \tag{5.8}$$

where ϕ_1, ϕ_2, ϕ_3 are the solutions for fine, medium and coarse kth input parameters. The apparent order Υ of the method is represented by

$$\Upsilon = \frac{1}{\ln(r_k)} \left| \ln \left| \frac{\iota_{32}}{\iota_{21}} \right| \right|. \tag{5.9}$$

The extrapolated values could be determinate by

$$\phi_{\text{ext}}^{21} = (r_k\phi_1 - \phi_2)(r_k^{\Upsilon} - 1). \tag{5.10}$$

The approximate relative error between medium-fine e_a^{21} and coarse-medium e_a^{32} solution and the extrapolate relative error between e_{ext}^{21} and e_{ext}^{32} are computed as

$$e_a^{21} = \left| \frac{\phi_1 - \phi_2}{\phi_1} \right|, \tag{5.11}$$

$$e_{\text{ext}}^{21} = \left| \frac{\phi_{\text{ext}}^{12} - \phi_2}{\phi_{\text{ext}}^{12}} \right|. \tag{5.12}$$

Finally, the fine-GCI is calculated by

$$GCI_{\text{fine}}^{21} = \frac{1.25 e_a^{21}}{r^{\Upsilon} - 1}. \tag{5.13}$$

The total resistance R_t of the vessel is compose of two components: the frictional R_f and the pressure R_p resistances. The computed values of the resistance and its components of the fine, medium and coarse grids are shown in the Table 5.13. The results of e_a^{21} demonstrates that all the resistance have a too small approximate errors. Later, the GCI_{fine}^{21} values in all resistances are no more than 1%. To maintain the an affordable computational cost, the medium grid is chosen since the errors calculated in all grid set are low.

Parameter	R_p (N)	R_f (N)	R_t (N)
ϕ_1	4.3800	2.5650	6.9450
ϕ_2	4.4910	2.5634	6.9544
ϕ_3	4.4320	2.5660	6.9980
p	3.7962	1.4009	4.4272
ϕ_{ext}^{21}	0.6612	1.7025	0.7881
e_a^{21} (%)	0.0025	0.0006	0.0014
e_{ext}^{21} (%)	5.6244	0.5066	7.8124
GCI_{fine}^{21} (%)	0.0012	0.0012	0.0005

Table 5.13: Grid convergence parameters. Source: Author.

5.7.2 Calculation of the properties

The following subsections is presented results of the calculation of the properties of the 2700 TDW inland vessel. Pressure coefficient, skin friction coefficient, dimensionless wall distance and wave pattern are visualized. Finally, the wetted surface is illustrated.

In the Figure 5.24a is shown the cross sections that are used to present the results. According to this figure, three transverse cross sections trace along the hull at $x = 0.200$ m, $x = 2.000$ m and $x = 4.000$ m; three longitudinal cross sections trace along the hull at $y = 0.005$ m, $y = 0.200$ m and $y = 0.350$ m; and two longitudinal cross sections are located outside of the hull at $y = 0.920$ m and $y = 1.500$ m. In the Figure 5.24b is illustrated the longitudinal cross section in z axis to measure the velocity magnitude and pressure distribution between the hull and wall bottom at $z = -0.240$ m.

5.7.2.1 Pressure coefficient

In the Figure 5.25 shows the contour plots of the pressure coefficient on the inland vessel hull. The significant higher pressure is observed for lowest velocity (a). For highest velocity, the pressure is low between the hull and the wall bottom (d). Contour blue color corresponds the air flow.

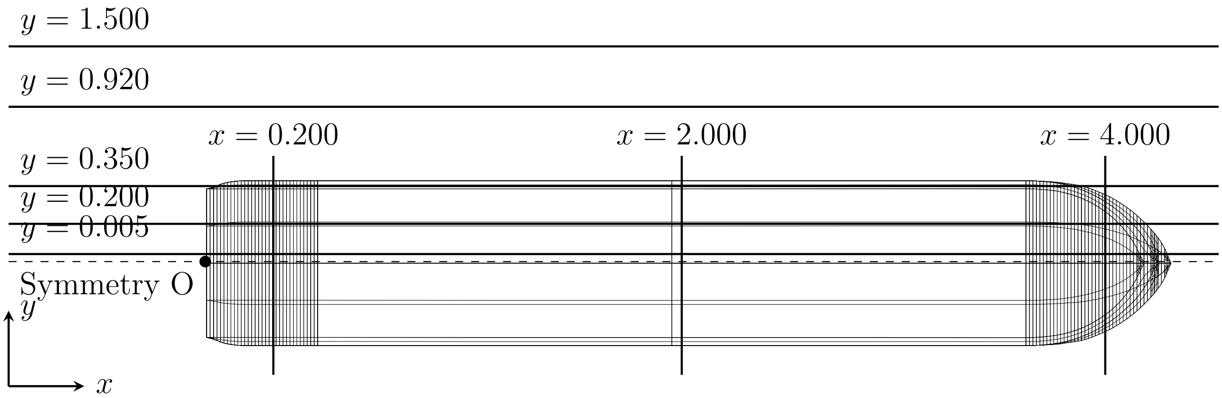

(a) $x - y$ axis

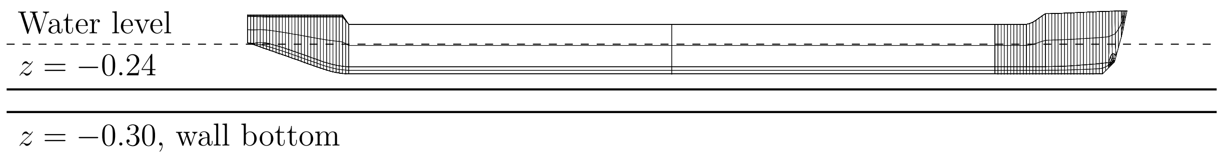

(b) $z - y$ axis

Figure 5.24: Cross sections in scale model at different x, y and z coordinates axis used in the illustrations of the results. The origin point of the computational domain is marked by O, and its position in all coordinate axis is zero ($z = 0$ m in the water surface). Source: Author.

(a) $v = 0.576$ m/s

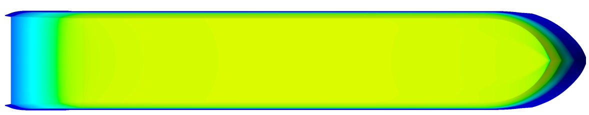

(b) $v = 0.691$ m/s

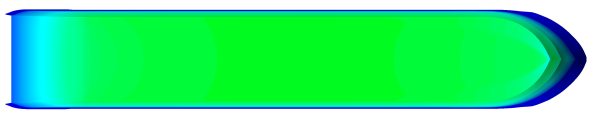

(c) $v = 0.806$ m/s

(d) $v = 0.921$ m/s

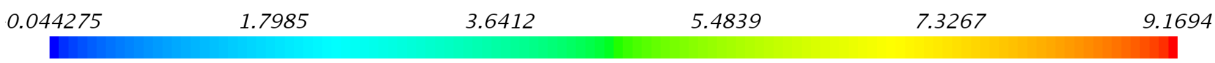

Figure 5.25: Contour plots of the pressure coefficient on the inland vessel hull performed on *STAR-CCM+*. Source: Author.

In the Figure 5.26 are shown the longitudinal cross section of the pressure coefficient on the inland vessel hull. At $y = 0.005$ m and $y = 0.200$ m, the values are similar, but the coefficient is low at the end of the hull beam. The values are more 9 in case of low velocity, and almost 3.5 in case to higher velocity. In the Figure 5.27 are shown the transverse cross section of the pressure coefficient on the inland vessel hull. The values are low at stern but higher at bow and midsection. The plot of these values take the hull geometry form.

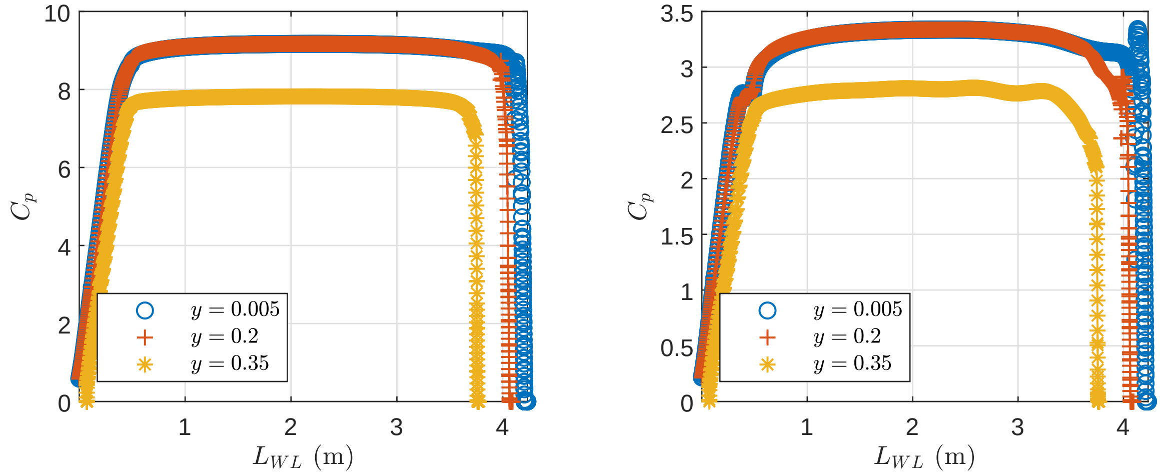

(a) $v = 0.576$ m/s (b) $v = 0.921$ m/s

Figure 5.26: Longitudinal cross section of the pressure coefficient on the inland vessel hull at lowest (a) and highest (b) velocities performed on *STAR-CCM+*. Source: Author.

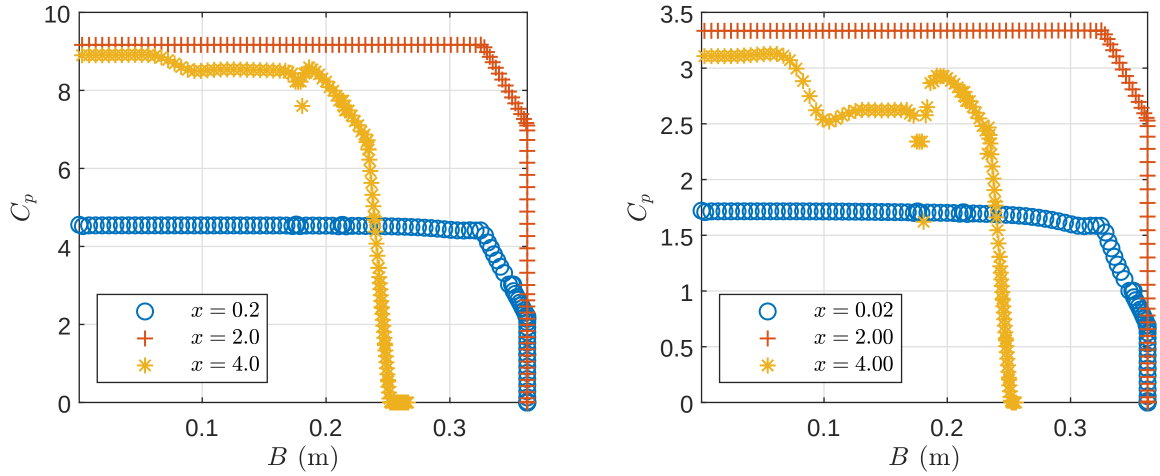

(a) $v = 0.576$ m/s (b) $v = 0.921$ m/s

Figure 5.27: Transverse cross section of the pressure coefficient on the inland vessel hull at lowest (a) and highest (b) velocities performed on *STAR-CCM+*. Source: Author.

5.7.2.2 Skin friction coefficient

In the Figure 5.28 shows the contour plots of the skin friction coefficient on the inland vessel hull. It can be observed that the contour of this coefficient is the same for different velocities, and it is illustrated in the Figures 5.29 and 5.30, where the behavior is similar. The values are maintained in less that 0.01 except in the bow zone, where the values are high.

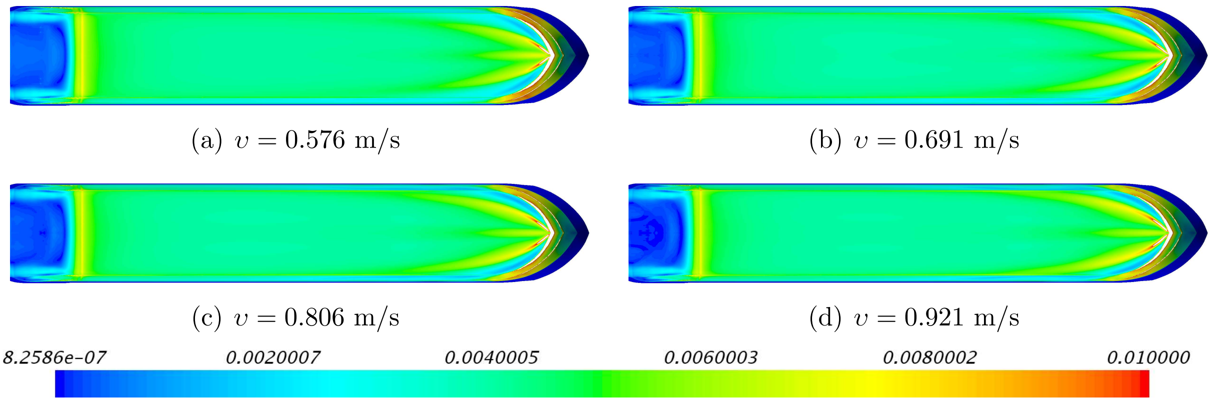

(a) $v = 0.576$ m/s (b) $v = 0.691$ m/s (c) $v = 0.806$ m/s (d) $v = 0.921$ m/s

Figure 5.28: Contour plots of the skin friction coefficient on the inland vessel hull performed on *STAR-CCM+*. Source: Author.

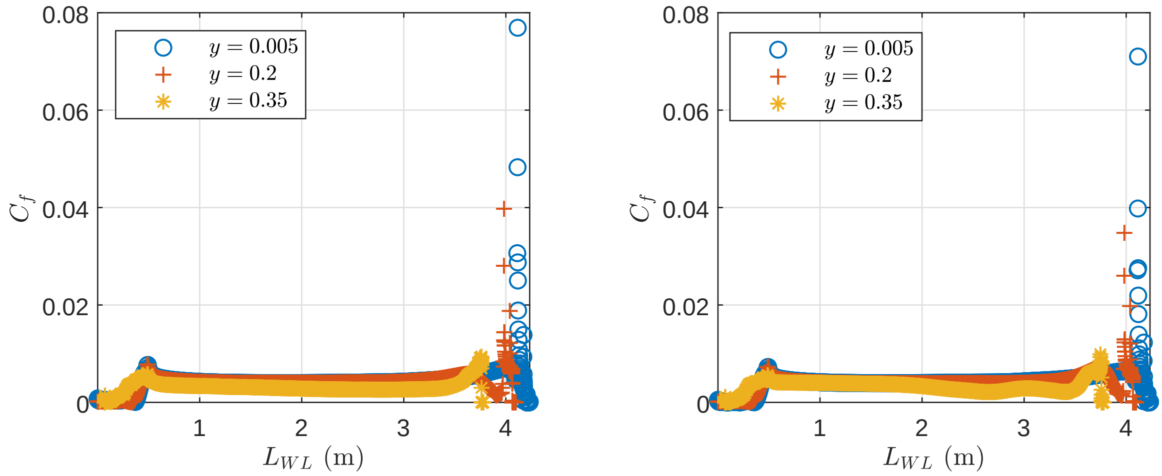

(a) $v = 0.576m/s$ (b) $v = 0.921m/s$

Figure 5.29: Longitudinal cross section of the skin friction coefficient on the inland vessel hull at lowest (a) and highest (b) velocities performed on *STAR-CCM+*. Source. Author.

5.7.2.3 Dimensionless wall distance $y+$

In the Figure 5.31 shows the contour plots of the dimensionless wall distance on the inland vessel hull. The high values of $y+$ greater than 1 are market in white and it happens in the inland vessel bow. This is because the value of the distance y is based on low velocities and it can be used for highest velocities. However, the distance y can be calculated for different velocities without affecting the numerical simulation results. These measures are observed in the Figures 5.32 and 5.33, where in inland vessel bow is higher in all velocities. The choosing of the first thickness of the prism layer $y+$, the region of the air were not taken account.

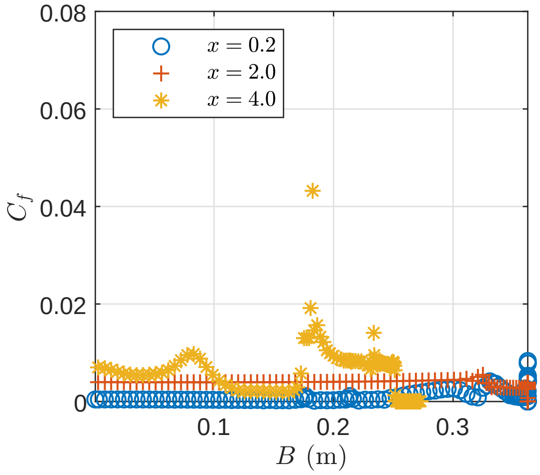

(a) $v = 0.576m/s$

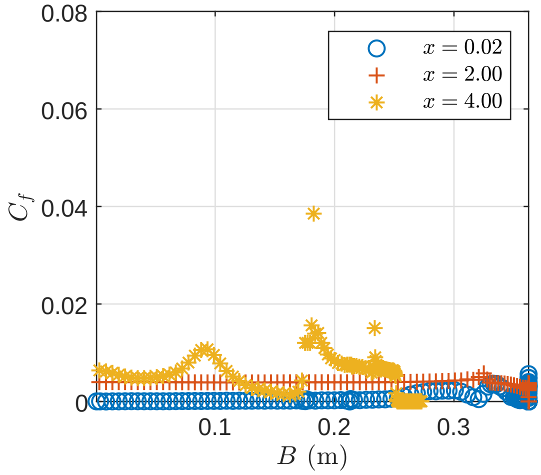

(b) $v = 0.921m/s$

Figure 5.30: Longitudinal cross section of the skin friction coefficient on the inland vessel hull at lowest (a) and highest (b) velocities performed on *STAR-CCM+*. Source. Author.

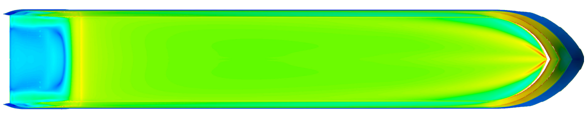

(a) $v = 0.576m/s$

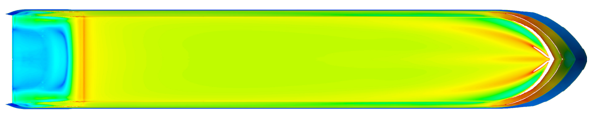

(b) $v = 0.691m/s$

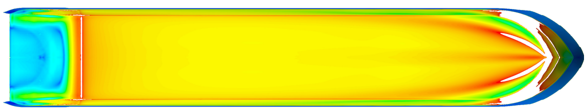

(c) $v = 0.806m/s$

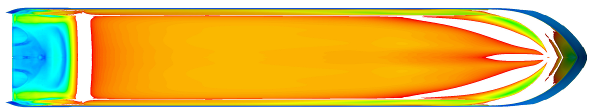

(d) $v = 0.921m/s$

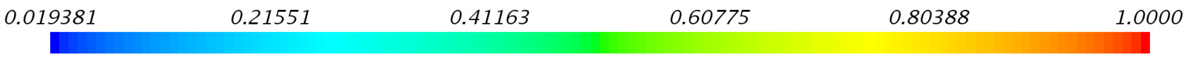

Figure 5.31: Contour plots of the dimensionless wall distance $y+$ on the inland vessel hull performed on *STAR-CCM+*. Source. Author.

5.7.2.4 Wave pattern

The wave pattern is generated by the hull of the inland vessel for each velocity, visualized in the Figure 5.34, showing the Kelvin waves system which consists of transverse and divergent waves, and its angulation is titled up to 19 degrees. The presence of the walls causes reflection of the waves. The wave height was measured in the longitudinal cross section outside in the hull and is illustrated in the Figure 5.35. This measure was captured by the mesh created on *STAR-CCM+*. At lowest velocity, there are more oscillations that highest velocity. Another observation is the level of the water surface at inlet, where is not initiates at origin level. Its mean that the computational domain must be bigger, approximately six times the length of the inland vessel in x-direction.

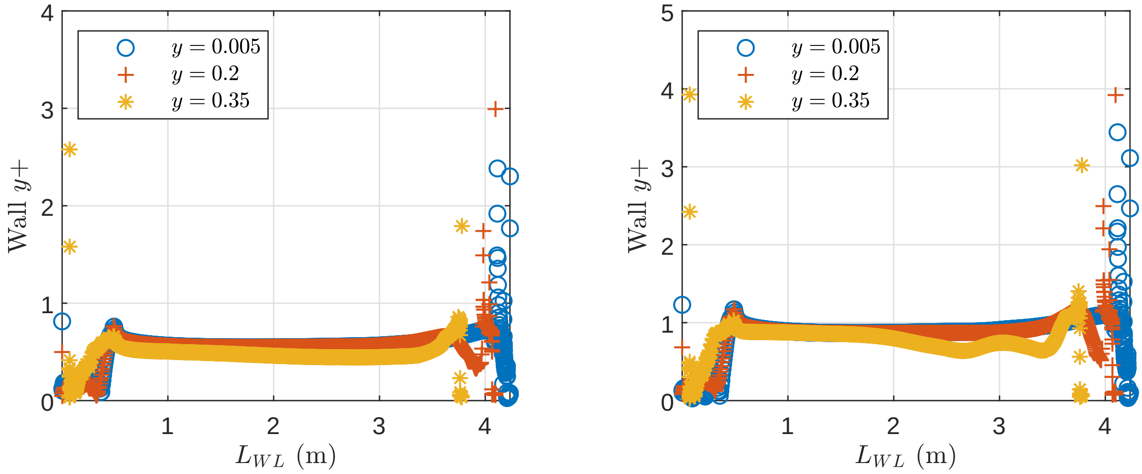

(a) $v = 0.576m/s$ (b) $v = 0.576m/s$

Figure 5.32: Longitudinal cross section of the dimensionless wall $y+$ on the inland vessel hull at lowest (a) and highest (b) velocities performed on *STAR-CCM+*. Source: Author.

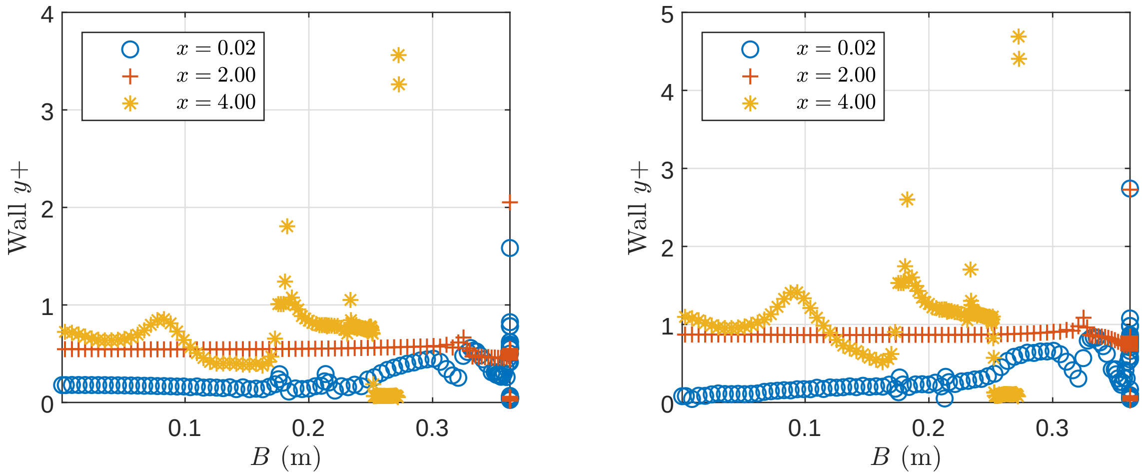

(a) $v = 0.921m/s$ (b) $v = 0.921m/s$

Figure 5.33: Transverse cross section of the dimensionless wall $y+$ on the inland vessel hull at lowest (a) and highest (b) velocities performed on *STAR-CCM+*. Source: Author.

5.7.2.5 Velocity and pressure distribution

In the Figures 5.36 and 5.37 shows the contour of the velocity distribution of the water in the computational domain. From the symmetry view, there is higher velocity between the hull and the wall bottom. From the top view, there is low velocity distribution of the water at the bow and stern. The space between the wall and the hull there is changes of the velocity distribution of the water.

In the Figures 5.38 and 5.39 shows the contour of the pressure distribution of the

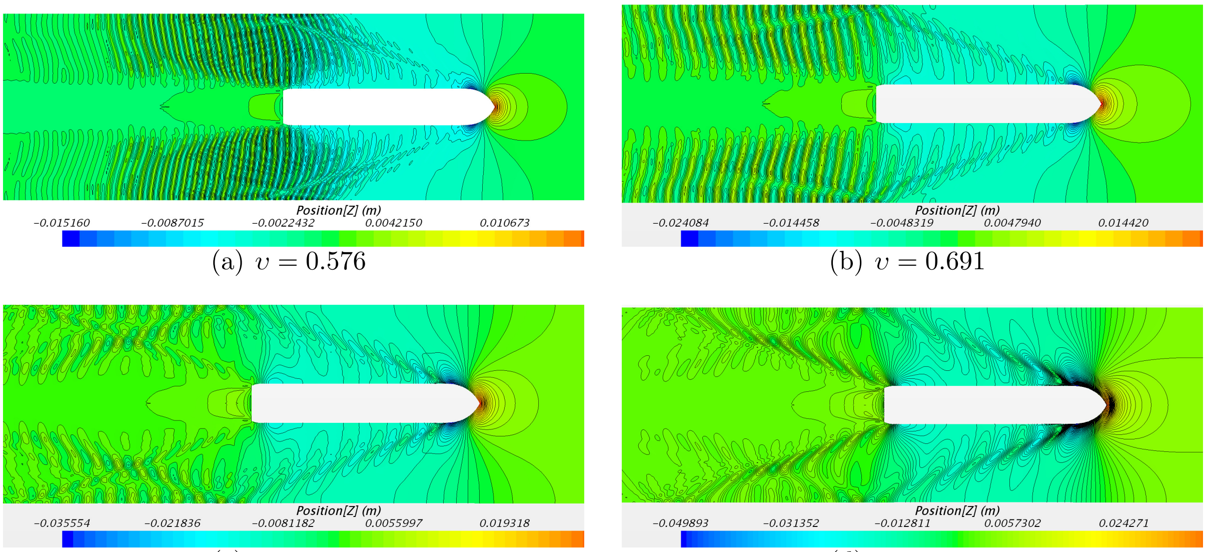

(a) $\upsilon = 0.576$ (b) $\upsilon = 0.691$

(c) $\upsilon = 0.806$ (d) $\upsilon = 0.921$

Figure 5.34: Wave pattern generated by 2700 TDW inland vessel performed on *STAR-CCM+*. Source: Author.

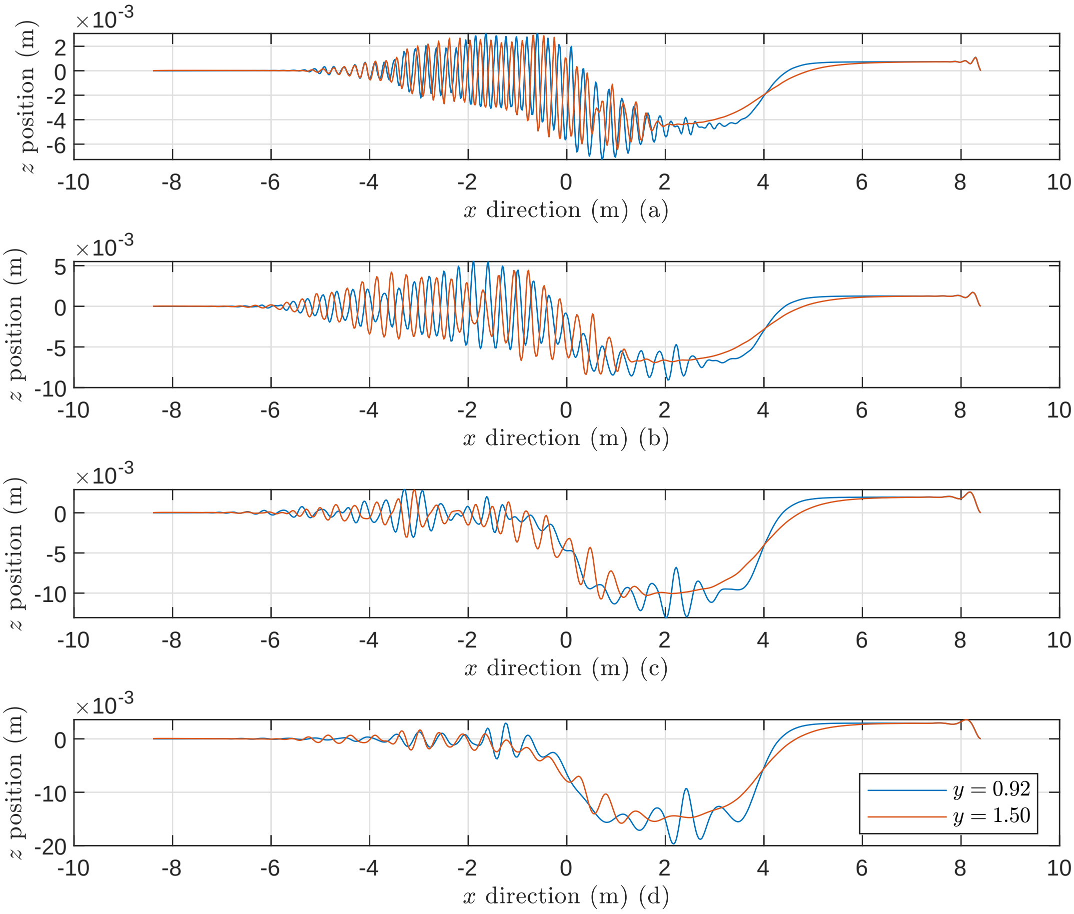

Figure 5.35: Longitudinal cross section of the wave height generated by 2700 TDW inland self-propelled vessel measured in different transversal cross sections at (a) $\upsilon = 0.576$, (b) $\upsilon = 0.691$, (c) $\upsilon = 0.806$ and (d) $\upsilon = 0.921$ performed on *STAR-CCM+*. Source: Author.

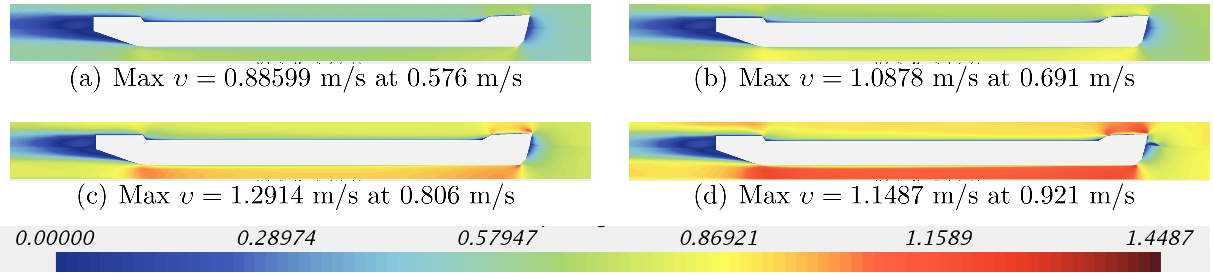

(a) Max $v = 0.88599$ m/s at 0.576 m/s
(b) Max $v = 1.0878$ m/s at 0.691 m/s
(c) Max $v = 1.2914$ m/s at 0.806 m/s
(d) Max $v = 1.1487$ m/s at 0.921 m/s

Figure 5.36: Velocity magnitude on the computational domain (symmetry view) performed on *STAR-CCM+*. Source: Author.

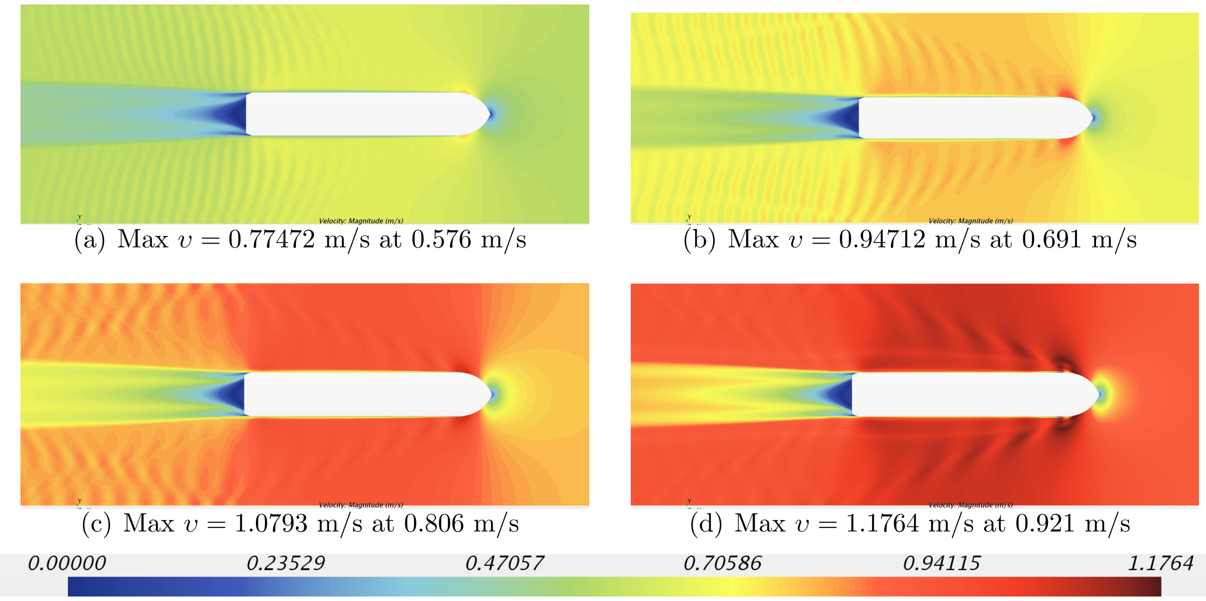

(a) Max $v = 0.77472$ m/s at 0.576 m/s
(b) Max $v = 0.94712$ m/s at 0.691 m/s
(c) Max $v = 1.0793$ m/s at 0.806 m/s
(d) Max $v = 1.1764$ m/s at 0.921 m/s

Figure 5.37: Velocity magnitude of of the water generated by 2700 TDW inland vessel at different velocities (top view) performed on *STAR-CCM+*. Source: Author.

water and air in the computational domain. From the symmetry view, the air flow is marked in blue. There is higher pressure between the hull and wall bottom and there is no changes of the pressure. From the top view, there is significant changes between the wall and the hull. The faster the ship navigates the pressures increase. At the bow, the value of this variable is higher.

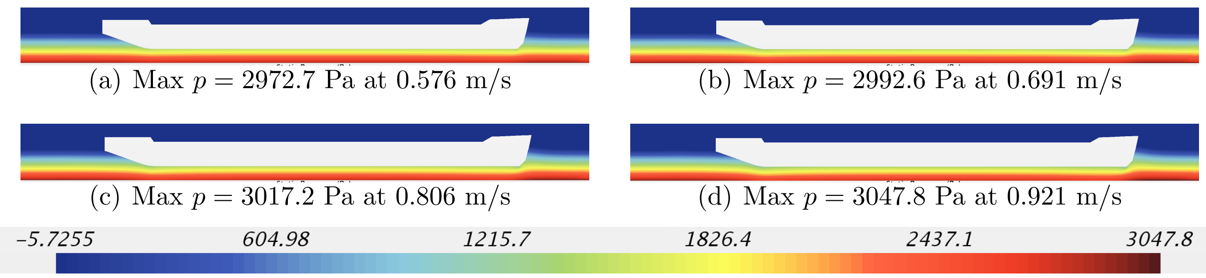

(a) Max $p = 2972.7$ Pa at 0.576 m/s
(b) Max $p = 2992.6$ Pa at 0.691 m/s
(c) Max $p = 3017.2$ Pa at 0.806 m/s
(d) Max $p = 3047.8$ Pa at 0.921 m/s

Figure 5.38: Pressure distribution of the air and water on the computational domain (symmetry view) performed on *STAR-CCM+*. Source: Author.

(a) Min p = 144.63 Pa, Max p = 455.77 Pa at 0.576 m/s

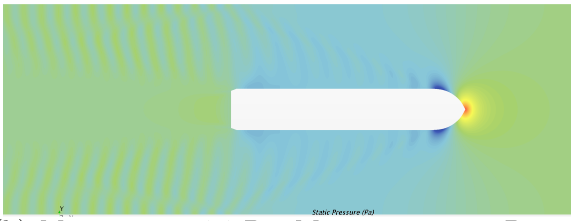

(b) Min p = 58.274 Pa, Max p = 525.56 Pa at 0.691 m/s

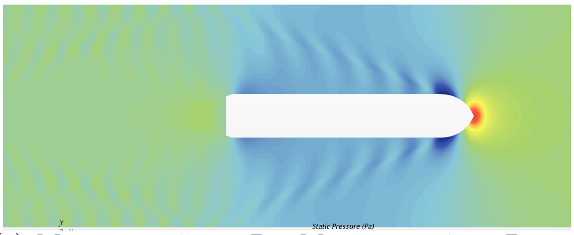

(c) Min p = 0.47628 Pa, Max p = 607.50 Pa at 0.806 m/s

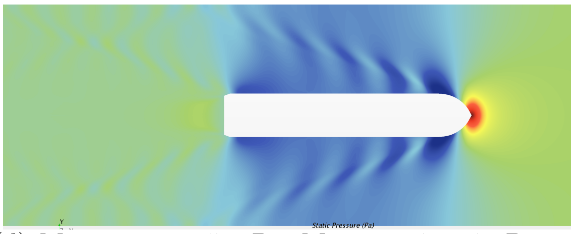

(d) Min p = 0.32479 Pa, Max p = 702.41 Pa at 0.921 m/s

Figure 5.39: Pressure distribution of the water generated by 2700 TDW inland vessel at different velocities (top view) performed on *STAR-CCM+*. Source: Author.

These effects are agreement with the Bernoulli's principle, explained in the chapter 3. The effect where the velocity of the water is higher between the hull and the bottom wall causing low pressure at this area is called *squat*. This behavior was measured in the Figure 5.40.

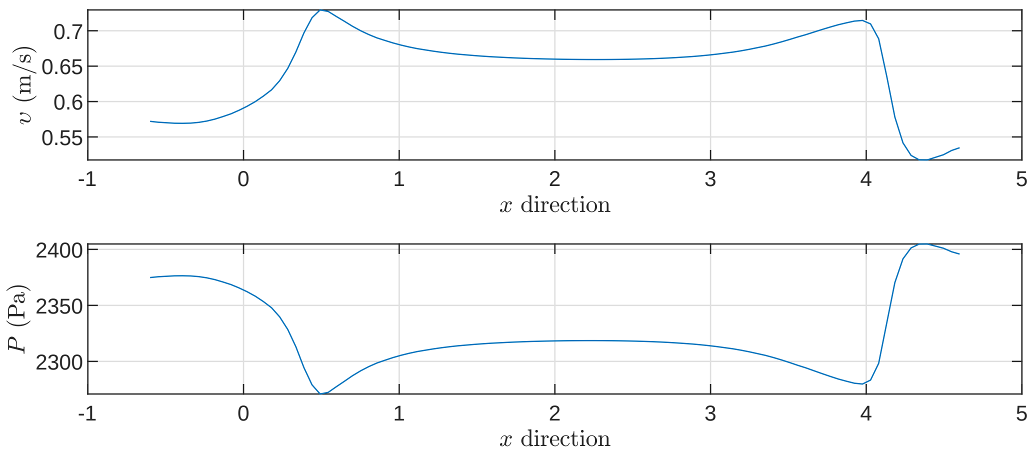

Figure 5.40: Longitudinal cross section of the velocity and the pressure distribution between the hull and wall bottom performed on *STAR-CCM+* on $z = -0.24$ m at $v = 0.576$ m/s. Source: Author.

5.7.2.6 Wetted surface of the hull

In the Figure 5.41 is shown the wetted surface area of the hull obtained from CFD-simulation. From IPT (1974), there is no measurement of the wetted surface for different velocities, thus, it is difficult to make measurements for this variable and there is no conclusions to describe these results.

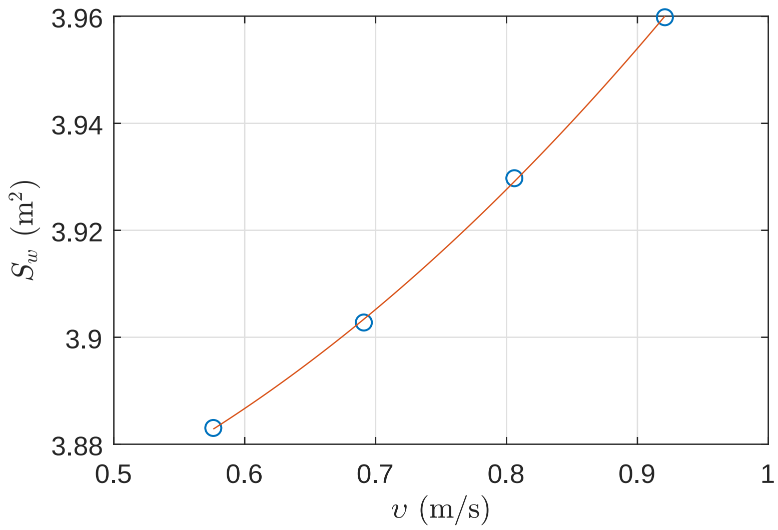

Figure 5.41: Wetted surface area of the 2700 TDW inland self-propelled vessel performed on *STAR-CCM+* at different velocities. Source: Author.

6 CONCLUSIONS

The problem solution by CFD allows the collecting data that are difficult to obtain from the experimental tests, for example, the velocity distribution of the water in the computational domain and the streamlines around the hull. The use of CFD can realize the corrections and improvements of the hull in the process design. This is no mean that the experimental test could be replaced by CFD simulation despite the numerical simulations must be faster or cost less.

The conclusions of this study could be listed as follows:

- The formulations for the empirical procedure were satisfactory only in case of vessel navigating in middle rivers in which case the most appropriate is the Karpov's and Artjushkov's method.
- In the case of other methods used in barge operating in large rivers, the width of the affluent is not taken into account, implying less velocity loss. The wave resistance is not taken account instead of residuary resistance is used. Also, the formulations for the application to this shallow water effects are not satisfied for the inland vessel hull in this study.
- The results of the inland vessel resistance by numerical simulation are satisfactory only in case of low speeds. As the speed increases, the relative error also increases up to 18%.
- The GCI applied in the mesh convergence criteria allow the choosing of the number of mesh in the numerical solution. The errors are too small, and the medium grid is chosen to simulate the ship resistance and calculate its properties at different velocities.
- The calculation properties by CFD allow the inside analysis of the performance of the inland vessel that the experimental analysis could be not measured. Is very

important the comparison of the numerical and the experimental results of some variables, as example, the wetted surface of the hull.

The numerical simulation results can be corrected with more precision in order to obtain results similar to those obtained in cases of navigation in shallow waters. For this purpose, it is important to present the future work, specifying aspects that must be analyzed.

6.1 Future analysis

All difficulties found during the development of this research could be listed as follows:

- Execution of test in reduced scale of the 2700 TDW inland vessel for obtaining the analysis as skinage and trim. Also, it must be calculating some measure variables as length of the vessel in waterline, wetted surface area, inclination angle, etc.
- Improves and optimizes the inland vessel hull geometry in bow and stern based on reference as Rotteveel, Hekkenberg and Ploeg (2017) and Tabaczek and Zawiślak (2018).
- Modification of the computational domain size (at last 6.5 times of L_{WL} of the ship model in x coordinate and 1.2 times of L_{WL} z coordinate from free surface of the water) and more elements in the grid mesh distribution (approximately 22 million), specially on the free surface and the space between the ship hull and the wall bottom.
- Apply the GCI criteria for the highest velocity imputing parameters (time step or cell size of the mesh) according to Linde *et al.* (2017).
- Application of the propulsion analysis, where it will study the propeller design and the power required to push the self-propelled inland vessel using CFD software with semi-empirical approach and its validation in model scale.
- Comparison of the experimental and semi-empirical approaches with others CFD software as *STAR-CCM+*, *ANSYS Fluent*, *OPEN Foam* and *Nektar++*. The relative error must be, at last, increase up to 5 %.
- News semi-empirical formulations of the shallow waters that implies the analysis of maneuverability, stability, hull dimensions, skinage, trim and others according to Raven (2012).

REFERENCES

ACOSTA-LOPERA, O. D.; CABRERA-TOVAR, J. H. *Conceptual Design of an Inland Water Ship Self-Propelled for Coal Transportation to Navigability of the Magdalena River Low Section (in Spanish)*. 89 p. Thesis (BSc.) — UTB, 2014.

ANSYS. *ANSYS Fluent R18.1 user guide*. Canonsburg, PA, United States: ANSYS, Inc., 2017.

ANWER, S. F. Basics of Mesh Generation. In: *TEQIP School on Computational Methods in Engineering Applications*. Kanpur, India: IITK, 2016. Available at: ⟨http://www.iitk.ac.in/tkic/workshop/FEM/ppt.php⟩.

ARTJUSHKOV, L. Wall Effect Correction for Shallow Water Model Tests. *Transactions of North East Coast Institution of Engineers and Shipbuilders*, v. 85, n. 2, p. 35–42, 1968.

BARAKAT, H. Z.; CLARK, J. A. Analytical and Experimental study of the Transient Laminar Natural Convection Flows in Partially Filled Liquid Containers. In: *3rd IHTC*. Chicago, United States: IHTC, 1966. p. 152–162.

BATCHELOR, G. *An Introduction of Fluid Dynamics*. Cambridge, United Kingdom: Cambridge University Press, 1967. 615 p.

Bernal Duffo, E. Magdalena River: Primordial scenario of the Fatherland (in Spanish). *Credencial Historia*, Bogotá, D.C., Colombia, 2013. Available at: ⟨http://www.banrepcultural.org/biblioteca-virtual/credencial-historia/numero-282/el-rio-magdalena-escenario-primordial-de-la-patria⟩.

BERTRAM, V. *Practical Ship Hydrodynamics*. Oxford, United Kingdom: Butterworth-Heinemann, 2000. 270 p.

BOUWMEESTER, J. *et al.* Recent studies on Push - Towing as a base for Dimensioning Waterways. In: *24th International Navigation Congress*. Brussels, Belgium: PIANC, 1977.

Bureau Voorlichting Binnenvaart. Inland Shipping in Numbers (in Dutch). *Blue Magazine*, Rotterdam, The Netherlands, p. 11, 2011.

Bureau Voorlichting Binnenvaart. *Types of Vessels*. n.d. Available at: ⟨https://www.bureauvoorlichtingbinnenvaart.nl/inland-navigation-promotion/basic-knowledge/types-of-vessels⟩.

Castro Pinzón, C. Páramo de las Papas. In: PÉREZ, R. M. (Ed.). *Holy Water (in Spanish)*. Bogotá, D.C., Colombia: Semana, 2017. ch. 3. Available at: ⟨http://especiales.semana.com/agua-bendita/paramopapas.html⟩.

CD-adapco. *STAR-CCM+ Version 9.06 User Guide*. Melville, United States: CD-adapco, 2014. 14041 p.

CELIK, I. B. *et al.* Procedure for Estimation and Reporting of Uncertainty Due to Discretization in CFD Applications. *Journal of Fluids Engineering*, v. 130, n. 7, 2008.

ÇENGEL, J. A.; CIMBALA, J. M. *Fluid Mechanics: Fundamentals and Applications.* 1st. ed. New York, United States: McGraw-Hill, 2006. 929 p.

COURANT, R.; ISAACSON, E.; REES, M. On the Solution of Nonlinear Hyperbolic Differential Equations by Finite Differences. *Communications on Pure and Applied Mathematics*, v. 5, n. 3, p. 243–255, 1952.

DELEFORTRIE, G.; GEERTS, S.; VANTORRE, M. The Towing Tank for Manoeuvres in Shallow Water. In: ULICZKA, K. *et al.* (Ed.). *4th MASHCON.* Hamburg, Germany: Bundesanstalt für Wasserbau, 2016. p. 266–235.

DEWAN, A. *Tackling Turbulent Flows in Engineering.* Berlin, Germany: Springer, 2011. 124 p.

DURBIN, P. A.; Pettersson Rief, B. A. *Statistical Theory and Modeling for Turbulent Flows.* 2nd. ed. Chichester, United Kingdom: John Wiley & Sons, 2011. 357 p.

Encyclopædia Britannica. Canals and Inland Waterways. In: DAVIES, E. A. J.; MARSH, C. M. (Ed.). *Encyclopædia Britannica Ultimate Reference Suite.* Chicago, United States: Encyclopædia Britannica, Inc., 2015a.

Encyclopædia Britannica. Fluid. In: *Encyclopædia Britannica Ultimate Reference Suite.* Chicago, United States: Encyclopædia Britannica, Inc., 2015b.

Encyclopædia Britannica. Froude Number (Fr). In: *Encyclopædia Britannica Ultimate Reference Suite.* Chicago, United States: Encyclopædia Britannica, Inc., 2015c.

Encyclopædia Britannica. Magdalena River. In: *Encyclopædia Britannica Ultimate Reference Suite.* Chicago, United States: Encyclopædia Britannica, Inc., 2015d.

Encyclopædia Britannica. Navier-Stokes Equation. In: HOSCH, W. L. (Ed.). *Encyclopædia Britannica Ultimate Reference Suite.* Chicago, United States: Encyclopædia Britannica, Inc., 2015e.

Encyclopædia Britannica. Reynolds number. In: *Encyclopædia Britannica Ultimate Reference Suite.* Chicago, United States: Encyclopædia Britannica, Inc., 2015f.

ENGELAND, M. v. *FREE!ship Manual.* Boston, United States: FREE!ship Project, 2006. 57 p.

EULER, L. General Principles Concerning the Motion of Fluids (in French). *Mémoires de lLacadémie des Sciences et des Belles-Lettres de Berlin*, n. 11, p. 217–273, 1755.

FIELDING, S. M. *Laminar Boundary Layer Theory.* Duham, United Kingdom: Durham University, 2005. Available at: ⟨https://community.dur.ac.uk/suzanne.fielding/teaching.html⟩.

FORTUNA, A. d. O. *Computational Techniques for Fluid Dynamics: Basic Concepts and Applications (in Portuguese).* 2nd. ed. São Paulo, Brazil: EDUSP, 2012. 552 p.

GENTRY, R. A.; MARTIN, R. E.; DALY, B. J. An Eulerian Differencing Method for Unsteady Compressible Flow problems. *Journal of Computational Physics*, v. 1, n. 1, p. 87–118, 1966.

GEORGAKAKI, A.; SORENSON, S. C. *Report on Collected Data and Resulting Methodology for Inland Shipping*. Lyngby, Denmark: Department of Mechanical Engineering, DTU, 2004. 110 p.

GULDHAMMER, H. E.; HARVALD, S. A. *Ship Resistance Effect of Form and Principal Dimensions*. Copenhagen, Denmark: Akademisk Forlag, 1974.

HARVALD, S. A. *Resistance and Propulsion of Ships*. New York, United States: John Wiley & Sons, 1983. 353 p.

HIRSCH, C. *Numerical Computation of Internal and External Flows: The Fundamentals of Computational Fluid Dynamics*. 2nd. ed. Oxford, United Kingdom: Butterworth-Heinemann, 2007. 680 p.

HIRT, C.; NICHOLS, B. Volume of Fluid (VOF) Method for the Dynamics of Free Boundaries. *Journal of Computational Physics*, v. 39, n. 1, p. 201–225, 1981.

HODGE, J. K.; STONE, A. L.; MILLER, T. E. Numerical Solution for Airfoils near Stall in optimized Boundary–Fitted Curvilinear Coordinates. *AIAA Journal*, v. 17, n. 5, p. 458–464, 1979.

IACCARINO, G. *Lectures in Computational Methods in Fluid Dynamics using commercial CFD Codes*. Stanford, United States: Stanford University, 2004. Available at: ⟨https://web.stanford.edu/class/me469b/index.html⟩.

IPT. *Resistance Test of Inland Vessel 2700 Self-propelled in Shallow Waters (in Portuguese)*. São Paulo, Brazil, 1974. 9 p.

ITTC. *Proceedings of the 11th ITTC Conference*. Madrid, Spain: ITTC, 1957. 347 p.

ITTC. *Proceedings of the 18th ITTC Conference*. Kobe, Japan: ITTC, 1987. 502 p.

ITTC. *Recommended Procedures and Guidelines*. Lyngby, Denmark: ITTC, 2014.

JANSEN, P.; SCHIJF, J. The Relation between the form of Cross Section, the method of Revetment and the Distribution of the Water Velocities in a Waterway. In: *Proceedings of 18th International Navigation Congress*. Rome, Italy: PIANC, 1953. p. 175–197.

JI, S. C. *3D Numerical Modelling of Shipwaves and associated Sediment Transport (in French)*. 130 p. Thesis (PhD) — UTC, 2013.

JI, S. C. *et al.* 3-D numerical simulation of convoy-generated waves in a restricted waterway. *Journal of Hydrodynamics*, Publishing House for Journal of Hydrodynamics, v. 24, n. 3, p. 420–429, 2012.

KARPOV, A. Calculation of Ship Resistance in Restricted Waters (in Russian). *TRUDY GII. T. IV*, v. 2, 1946.

LACKENBY, H. The Effect of Shallow Water on Ship Resistance. *The Shipbuilder and the Marine Engine-Builder*, v. 70, n. 672, 1963.

LANDWEBER, L. *Test of a Model in Restricted Channels*. Washington, D.C., United States: DTMB, 1939. 32 p.

LATORRE, R.; LUTHRA, G.; TANG, K. *Improvement of Inland Waterway Vessel and Barge Tow Performance: Translations of selected Chinese, German and Russian Technical Articles (Report No. 249)*. Ann Arbor, United States: Department of Naval Architecture and Marine Engineering, College of Engineering, University of Michigan, 1982. 73 p.

LAUNDER, B. E.; SPALDING, D. B. *Lectures in Mathematical Models of Turbulence*. London, United Kingdom: Academic Press, 1972. 169 p.

LAUNDER, B. E.; SPALDING, D. B. The Numerical Computation of Turbulent Flows. *Computer Methods in Applied Mechanics and Engineering*, v. 3, n. 2, p. 269–289, 1974.

LEWIS, E. V. (Ed.). *Principles of Naval Architecture*. 2. ed. Jersey City, United States: SNAME, 1988. 327 p.

LINDE, F. *et al.* Three-dimensional Numerical Simulation of Ship Resistance in Restricted Waterways: effect of Ship Sinkage and Channel Restriction. *Journal of Waterway, Port, Coastal, Ocean Engineering*, v. 143, n. 1, p. 1–11, 2017.

LIU, Y. *et al.* Numerical Predictions of Hydrodynamic Forces and Squat of Ships in Confined Waters. In: LIU, G.; HAN, X.; LI, Z. (Ed.). *Proceedings of the 8th ICCM*. Guilin, Guangxi, China: Scientech Publisher LLC, 2017. p. 1095–1110.

MALISKA, C. R. *Heat Transfer and Computational Fluid Mechanics (in Portuguese)*. Rio de Janeiro, Brazil: LTC Editora S.A., 1995. 424 p.

MENTER, F. R. Zonal Two Equation k-ω Turbulence Models for Aerodynamic Flows. In: *23rd Fluid Dynamics, Plasmadynamics, and Lasers Conference*. Orlando, United States: AIAA, 1993. p. 21.

Merriam-Webster. *The Merriam-Webster's Collegiate Dictionary*. 11th. ed. Springfield (MA), United States: Merriam-Webster, Inc., 2004. 939 p.

Ministry of Transport - Colombia. *Transportation in Numbers - Statistics 2017 (in Spanish)*. Bogotá, D.C., Colombia, 2018. 107 p.

MOLLAND, A. F.; TURNOCK, S. R.; HUDSON, D. A. *Ship Resistance and Propulsion*. New York, United States: Cambridge University Press, 2011. 537 p.

MOLLAND, A. F.; WILSON, P.; TAUNTON, D. Resistance Experiments on a Systematic Series of High Speed Displacement Monohull and Catamaran forms in Shallow Water. *Transactions of the Royal Institution of Naval Architects. Part A: International Journal of Maritime Engineering*, v. 2, n. 146, p. 19–38, 2004.

NAVIER, C.-L.-M.-H. Memory on the Laws of the Movement of Fluids (in French). *Mémoires de l'Académie Royale des Sciences Paris*, n. 6, p. 389–416, 1822.

NOH, W.; WOODWARD, P. SLIC (Simple Line Interface Calculation). In: VOOREN, A. van de; ZANDBERGEN, P. (Ed.). *Proceedings of the 5th International Conference on Numerical Methods in Fluid Dynamics*. Berlin, Germany: Springer, 1976. Lecture Notes in Physics, v. 59, p. 330–340.

NORRIS, S. E. *A Parallel Navier-Stokes Solver for Natural Convection and Free Surface Flow*. 229 p. Thesis (Ph.D.) — University of Sydney, 2000.

PATANKAR, S. V.; SPALDING, D. B. A calculation Procedure for Heat, Mass and Momentum Transfer in Three-Dimensional Parabolic Flows. *International Journal of Heat and Mass Transfer*, v. 15, n. 10, p. 1787–1806, 1972.

PATHAK, A.; RAESSI, M. A Three-Dimensional Volume-of-Fluid Method for reconstructing and advecting Three-Material Interfaces forming Contact Lines. *Journal of Computational Physics*, Elsevier Inc., v. 307, p. 550–573, 2016.

PLETCHER, R. H.; TANNEHILL, J. C.; ANDERSON, D. A. *Computational Fluid Mechanics and Heat Transfer*. 3rd. ed. Boca Raton, United States: CRC Press, 2013. 740 p.

POMMIER, M.; SELMI, M. Optimization of the Section of a Navigation Channel, study by Mathematical and Physical models. *La Houille Blanche*, n. 2, 1981.

POMPÉE, P.-J. About Modelling Inland Vessels Resistance and Propulsion and Interaction Vessel - Waterway. Key Parameters driving Restricted/Shallow Water Effects (Paper 180). In: PIANC. *7th International PIANC-SMART Rivers Conference*. Buenos Aires, Argentina: PIANC, 2015.

RAVEN, H. C. A Computational Study of Shallow-Water Effects on Ship Viscous Resistance. In: *Proceedings of 29th Symposium on Naval Hydrodynamics*. Gothenburg, Sweden: Chalmers University of Technology, 2012.

REYNOLDS, O. An Experimental Investigation of the Circumstances Which Determine Whether the Motion of Water Shall Be Direct or Sinuous, and of the Law of Resistance in Parallel Channels. *Philosophical Transactions of the Royal Society of London.*, v. 174, p. 935–982, 1883.

REYNOLDS, O. On the Dynamical Theory of Incompressible Viscous Fluids and the Determination of the Criterion. *Philosophical Transactions of the Royal Society of London. (Serie A.)*, v. 186, p. 123–164, 1895.

RICHARDSON, L. F. The Approximate Arithmetical Solution by Finite Differences of physical problems involving Differential Equations, with an application to the Stresses in a Masonry Dam. *Philosophical Transactions of the Royal Society A*, v. 210, n. 459-470, p. 307–357, 1910.

ROACHE, P. J. *Verification and Validation in Computational Science and Engineering*. Albuquerque, United States: Hermosa Publications, 1998. 464 p.

ROTTEVEEL, E.; HEKKENBERG, R.; PLOEG, A. van der. Inland Ship Stern Optimization in Shallow Water. *Ocean Engineering*, Elsevier Ltd., v. 141, p. 555–569, 2017.

RUNCHAL, A.; WOLFSHTEIN, M. Numerical Integration Procedure for the Steady State Navier-Stokes Equations. *Journal of Mechanical Engineering Science*, v. 11, n. 5, p. 445–453, 1969.

SAVEY, P. Hydraulic Phenomena related to the Passage of a Boat in a Canal. In: *The defense of Banks, Canals and Rivers (in French)*. Paris, France: ENPC, 1977. ch. 2.

SCHIJF, J. Protection of Embankments and Bed in Inland and Maritime Waters, and in Overflows or Weirs (in French). In: *Proceedings of 17th International Navigation Congress*. Lisbon, Portugal: PIANC, 1949. p. 61–78.

SCHLICHTING, H. *Boundary-Layer Theory*. 7nd. ed. New York, United States: McGraw-Hill, 1979. 817 p.

SCHLICHTING, O. Ship Resistance in Water of Limited Depth – Resistance of Seagoing Vessels in Shallow Water (in German). *Janhrbuch der Schiffbautechnischen Gesellshaft*, v. 35, p. 127–148, 1934.

SHIH, T.-H. *et al.* A new k-ϵ Eddy Viscosity Model for High Reynolds Number Turbulent Flows. *Computers and Fluids*, v. 24, n. 3, p. 227–238, 1995.

STOKES, G. G. On the Theories of the Internal Friction of Fluids in Motion and of the Equilibrium and Motion of Elastic Solids. *Transactions of the Cambridge Philosophical Society*, v. 8, p. 287–305, 1845.

STULL, R. *Meteorology for Scientists and Engineers*. 2. ed. Pacific Grove, United States: Brooks/Cole, 2000. 502 p.

TABACZEK, T.; ZAWIŚLAK, M. Hull Resistance of An Inland Waterway Vessel in Model Scale and in Full Scale. *Polish Maritime Research*, v. 25, n. s1, p. 80–84, 2018.

TAMAMIDIS, P.; ASSANIS, D. N. Evaluation of Various High-Order-Accuracy Schemes with and without Flux Limiters. *International Journal for Numerical Methods in Fluids*, v. 16, n. 10, p. 931–948, 1993.

TENAUD, R. Model tests and Mathematical models for the Study of the Passage of Pushed Convoys in a Canal and Defenses of the Banks (in French). In: *Proceedings of 24h International Navigation Congress*. Leningrad, Russia: PIANC, 1977.

THOMPSON, C.; WILKERS, N. *Experiments with Higher-Order Finite Difference Formulae*. Harwell, Oxfordshire, United Kingdom, 1982.

TU, J.; YEOH, G.-H.; LIU, C. *Computational Fluid Dynamics: A Practical Approach*. 2nd. ed. Oxford, United Kingdom: Butterworth-Heinemann, 2008. 480 p.

TUPPER, E. C. *Introduction to Naval Architecture*. 4th. ed. Oxford, United Kingdom: Butterworth-Heinemann, 2004. 446 p.

VERSTEEG, H. K.; MALALASEKERA, W. *An Introduction to Computational Fluid Dynamics, The Finite Volume Methods*. 2nd. ed. Harlow, United Kingdom: Pearson Education Limited, 2007. 503 p.

WARMING, R.; BEAM, R. M. Upwind Second-Order Difference Schemes and Applications in Aerodynamic Flows. *AIAA Journal*, v. 14, p. 1241–1249, 1976.

WHITE, F. M. *Viscous Fluid Flow*. 2nd. ed. New York: McGraw-Hill, 1991. 614 p.

WHITE, F. M. *Fluid Mechanics*. 7th. ed. New York, United States: McGraw-Hill, 2011. 862 p.

WILCOX, D. C. Reassessment of the Scale-Determining Equation for Advanced Turbulence Models. *AIAA Journal*, v. 26, n. 11, p. 1299–1310, 1988.

WILCOX, D. C. *Turbulence Modeling for CFD*. 2nd. ed. La Cañada, United States: DCW Industries, Inc., 1998. 540 p.

YAKHOT, V. *et al.* Development of Turbulence Models for Shear Flows by a Double Expansion Technique. *Physics of Fluids*, v. 4, n. 7, p. 1510–1520, 1992.

APPENDIX A – GRAPHICS AND TABLES

This appendix shows the graphics of residuary resistance coefficient, made by Guldhammer and Harvald (1974). Also, the table of Georgakaki and Sorenson (2004) is included for generation of a code made in *MATLAB*.

Factor	Value	Limits
α^*	1	$x < 0.2$
α^*	$(1.072817327 - 2.95517983x + 2.677257924x^2 - 0.34935866x^3 + 0.242040284\ln(y/10) + 0.09728855(\ln(y/10))^2)/(1 - 2.65876522x + 2.128572396x^2 + 0.196411142\ln(y/10) + 0.05573344(\ln(y/10))^2 - 0.01424796(\ln(y/10))^3)$	$0.2 < x < 0.75$
α^*	$(1.016019336 + 12.53814509\ln x + 53.26949464(\ln x)^2 + 74.73282869(\ln x)^3 + 0.001376743\ln(y/10))/(1 + 12.31125171\ln x + 52.09394682(\ln x)^2 + 72.79361228(\ln x)^3 - 0.00395828\ln(y/10))$	$0.75 < x < 0.9$
α^*	1	$x > 0.9$
α^{**}	$(0.951498465 + 0.090322144\ln y - 0.02585333(\ln y)^2 + 0.003378671(\ln y)^3 - 2.05546622x + 1.088478007x^2)/(1 + 0.03275693\ln y - 0.0036447(\ln y)2 - 2.17156612x + 1.407458972x^2 - 0.18634398x^3)$	$\alpha^{**} < 1$
V_∞/V'	$(1.201296612 - 0.24893659y + 0.753380571\ln z + 0.004502733(\ln(z))^2)/(1 - 0.21424821y - 0.00366378y^2 + 0.000121814y^3 + 0.708479783\ln z)$	
ΔC_r	$0.001(-0.10885912 + 0.023641012y - 0.00248865y^2 + 0.0000856328y^3 - 0.02474568\ln z - 0.00476151(\ln z)^2)/(1 - 0.03640844y + 0.001560549y^2 + 1.696914134\ln z + 0.943623478(\ln z)^2 + 0.194816129(\ln z)^3)$	

Table A.1: Equations for the approximation of factors α^*, α^{**}, V_∞/V' and ΔC_r. Parameters: $x = F_h$, $y = h/T$, $z = B/b$. Source: Georgakaki and Sorenson (2004).

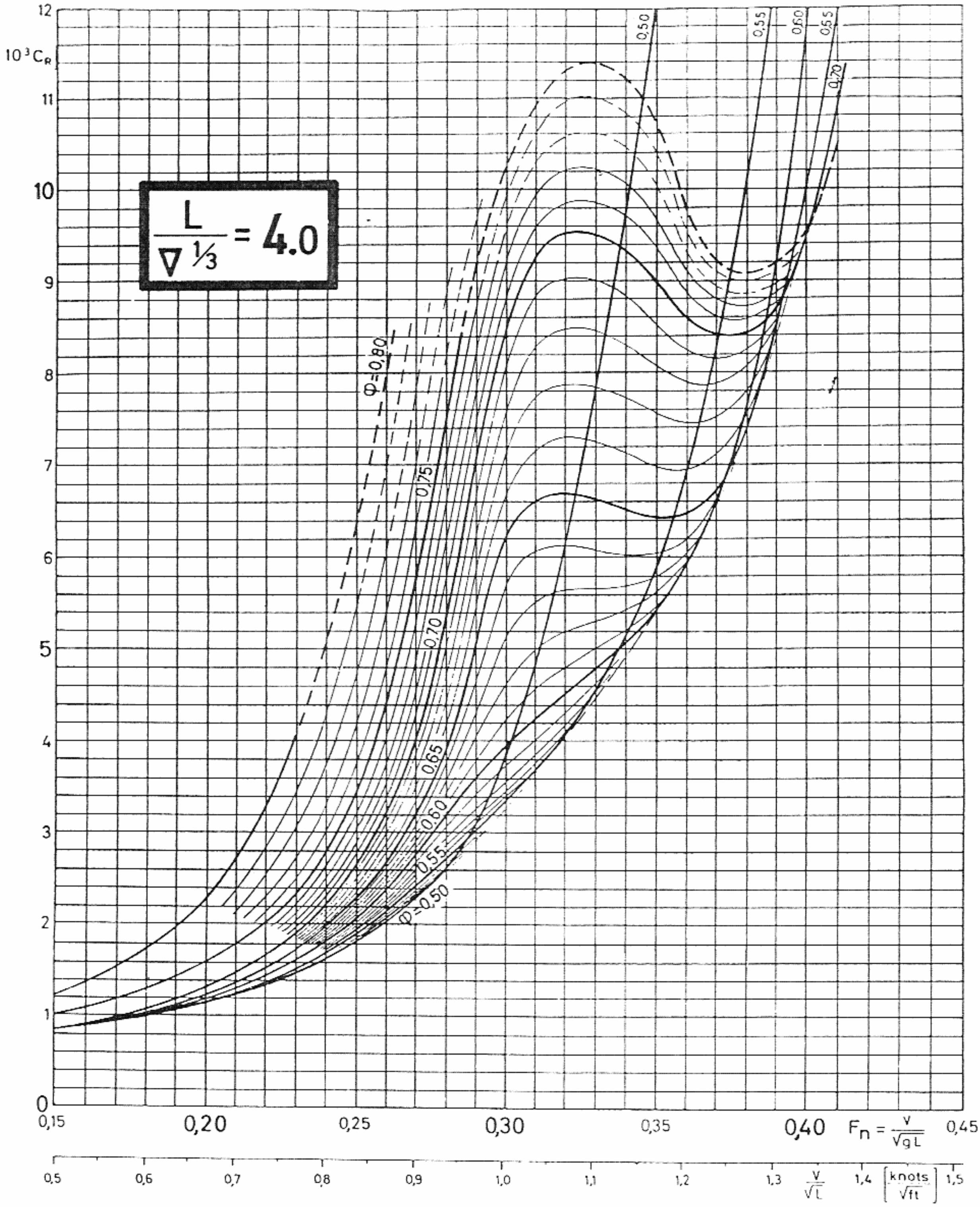

Figure A.1: Residuary resistance coefficient versus length Froude number for different values of longitudinal prismatic coefficient. $M = 4.0$. Source: Harvald (1983).

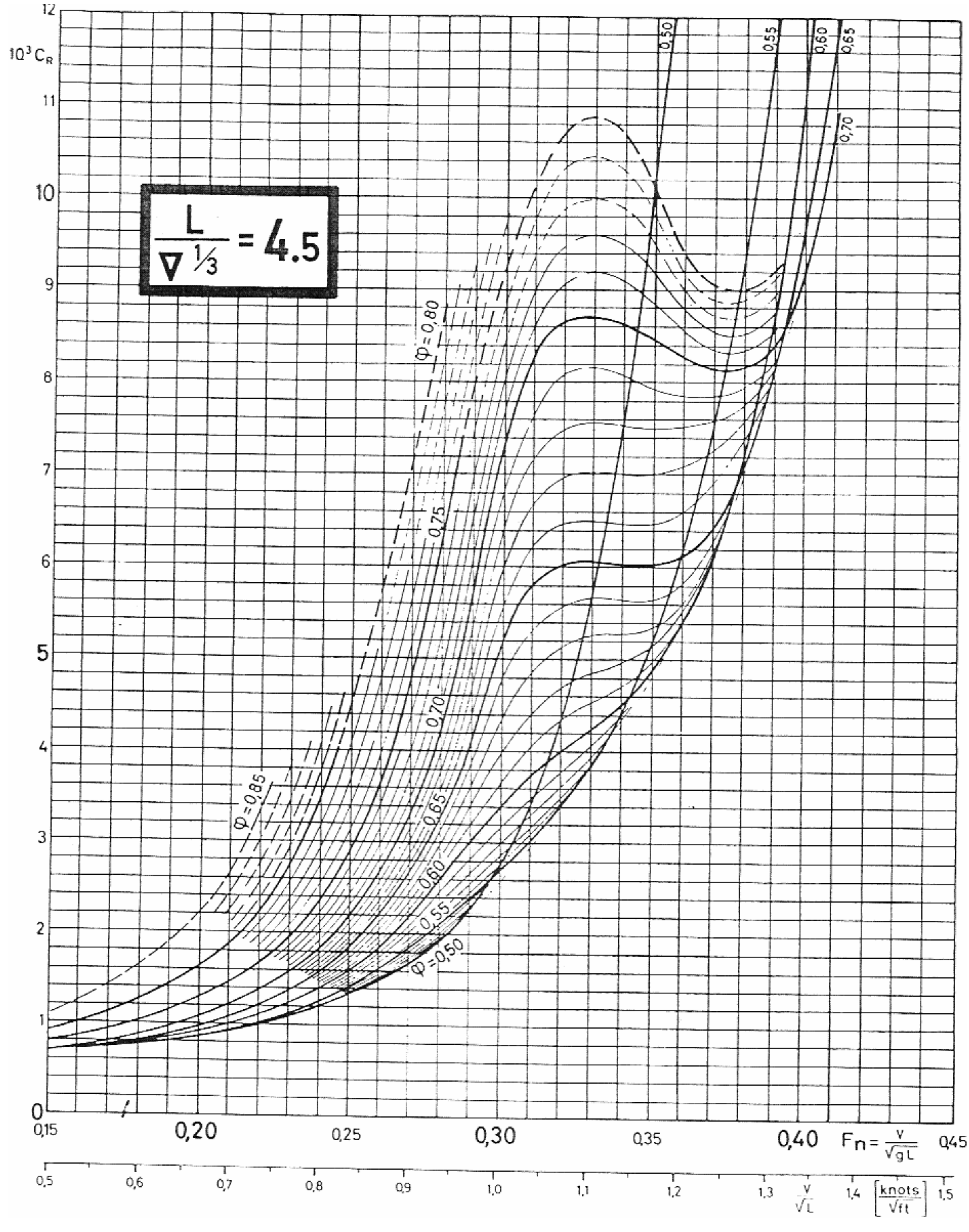

Figure A.2: Residuary resistance coefficient versus length Froude number for different values of longitudinal prismatic coefficient. $M = 4.5$. Source: Harvald (1983).

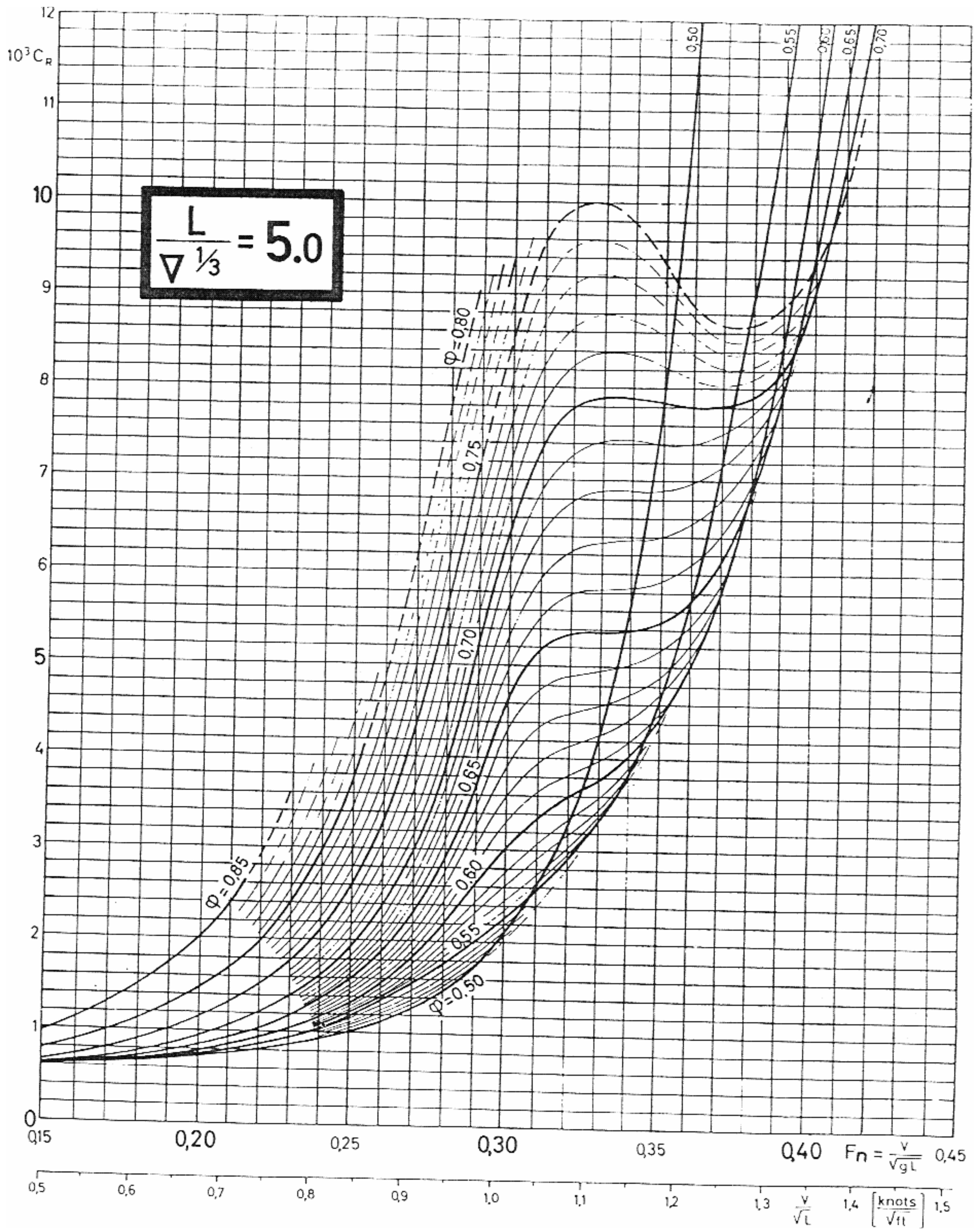

Figure A.3: Residuary resistance coefficient versus length Froude number for different values of longitudinal prismatic coefficient. $M = 5.0$. Source: Harvald (1983).

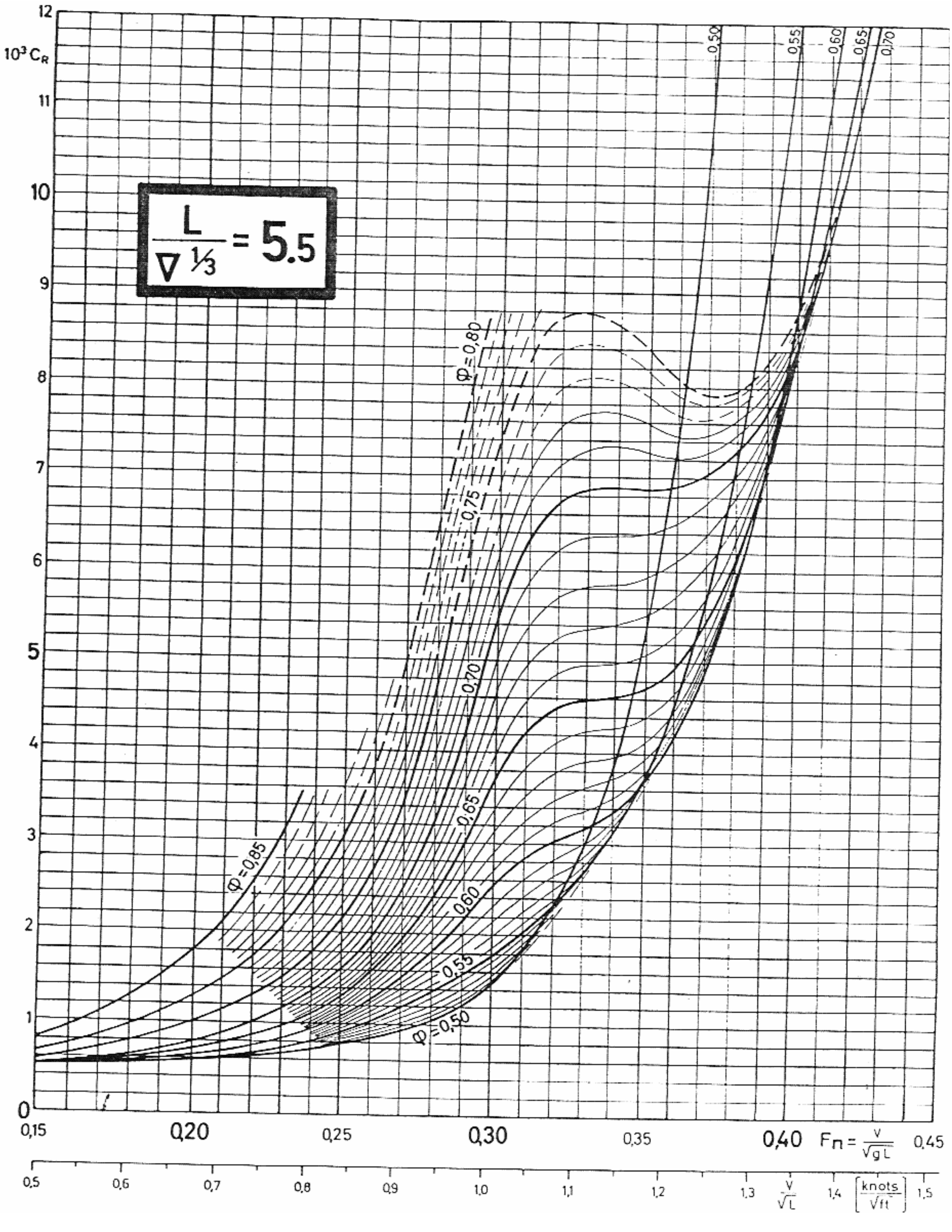

Figure A.4: Residuary resistance coefficient versus length Froude number for different values of longitudinal prismatic coefficient. $M = 5.5$. Source: Harvald (1983).

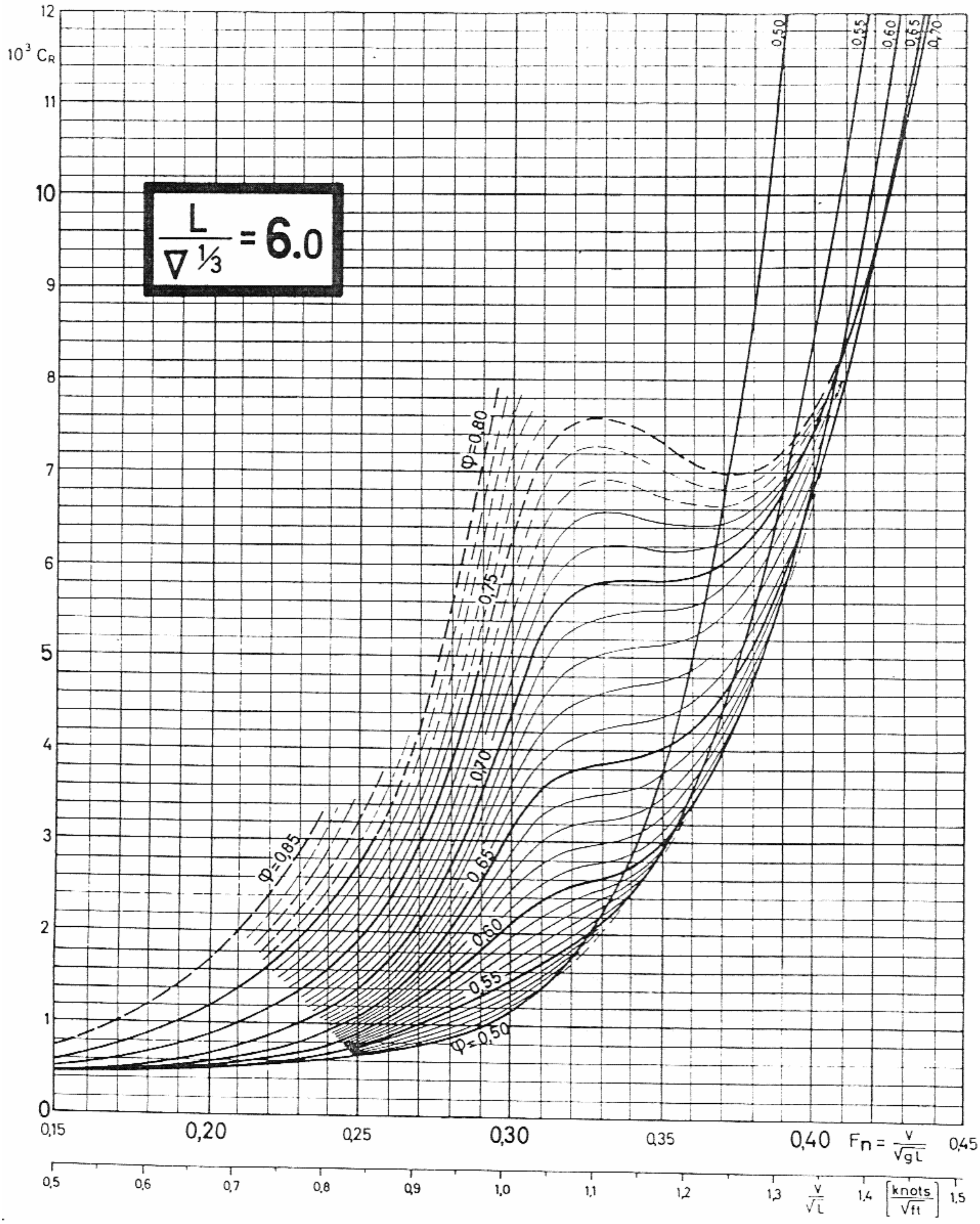

Figure A.5: Residuary resistance coefficient versus length Froude number for different values of longitudinal prismatic coefficient. $M = 6.0$. Source: Harvald (1983).

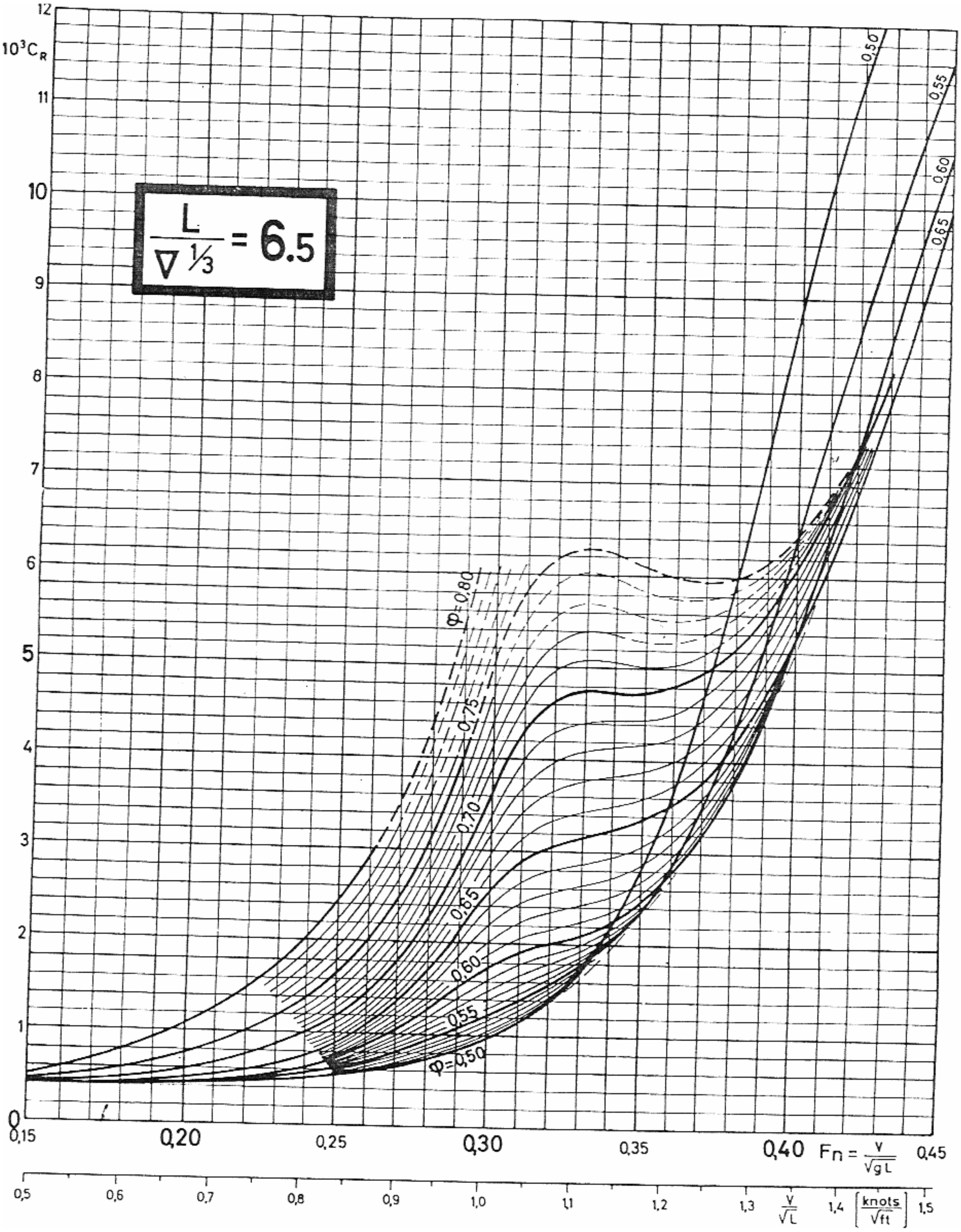

Figure A.6: Residuary resistance coefficient versus length Froude number for different values of longitudinal prismatic coefficient. $M = 6.5$. Source: Harvald (1983).

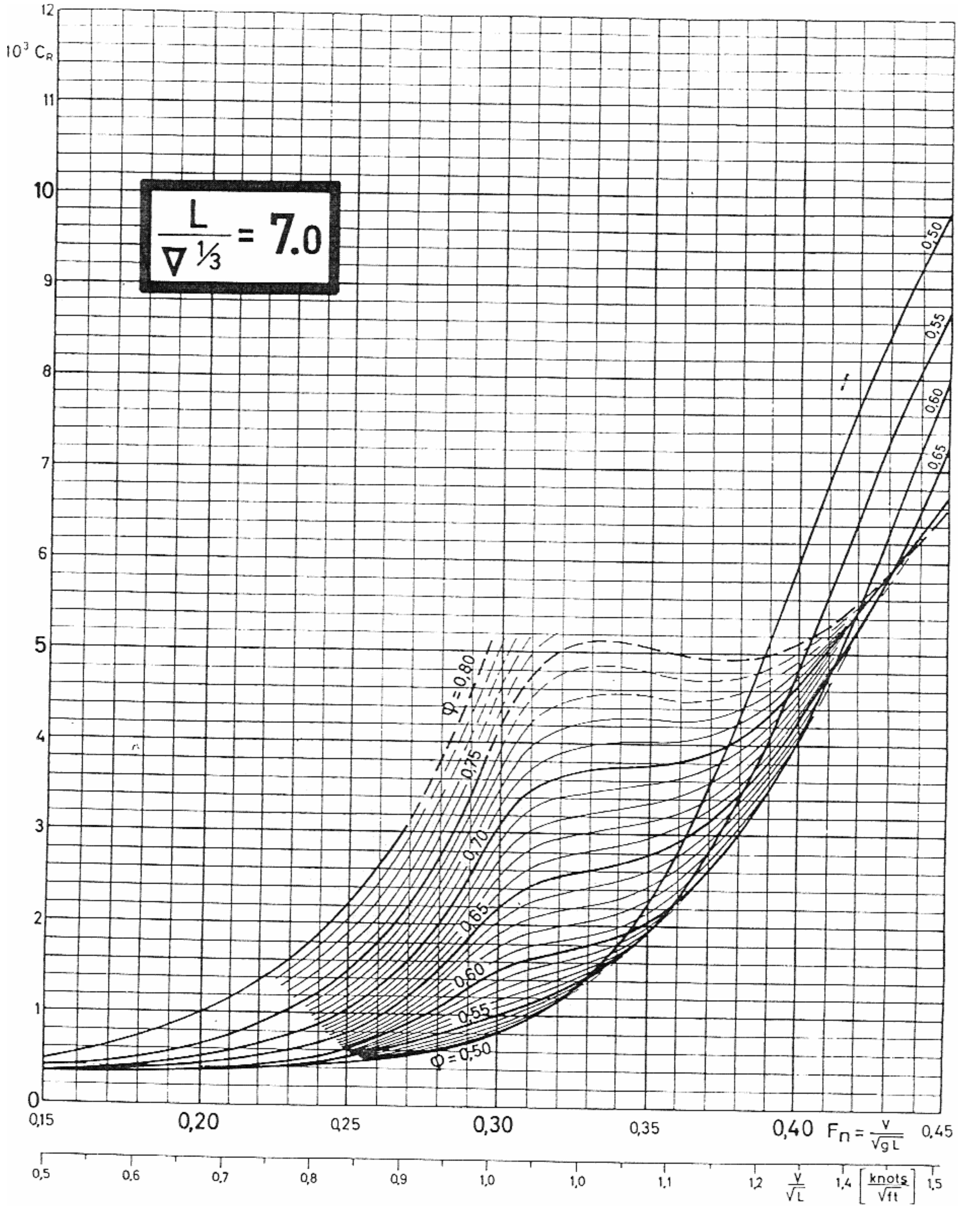

Figure A.7: Residuary resistance coefficient versus length Froude number for different values of longitudinal prismatic coefficient. $M = 7.0$. Source: Harvald (1983).

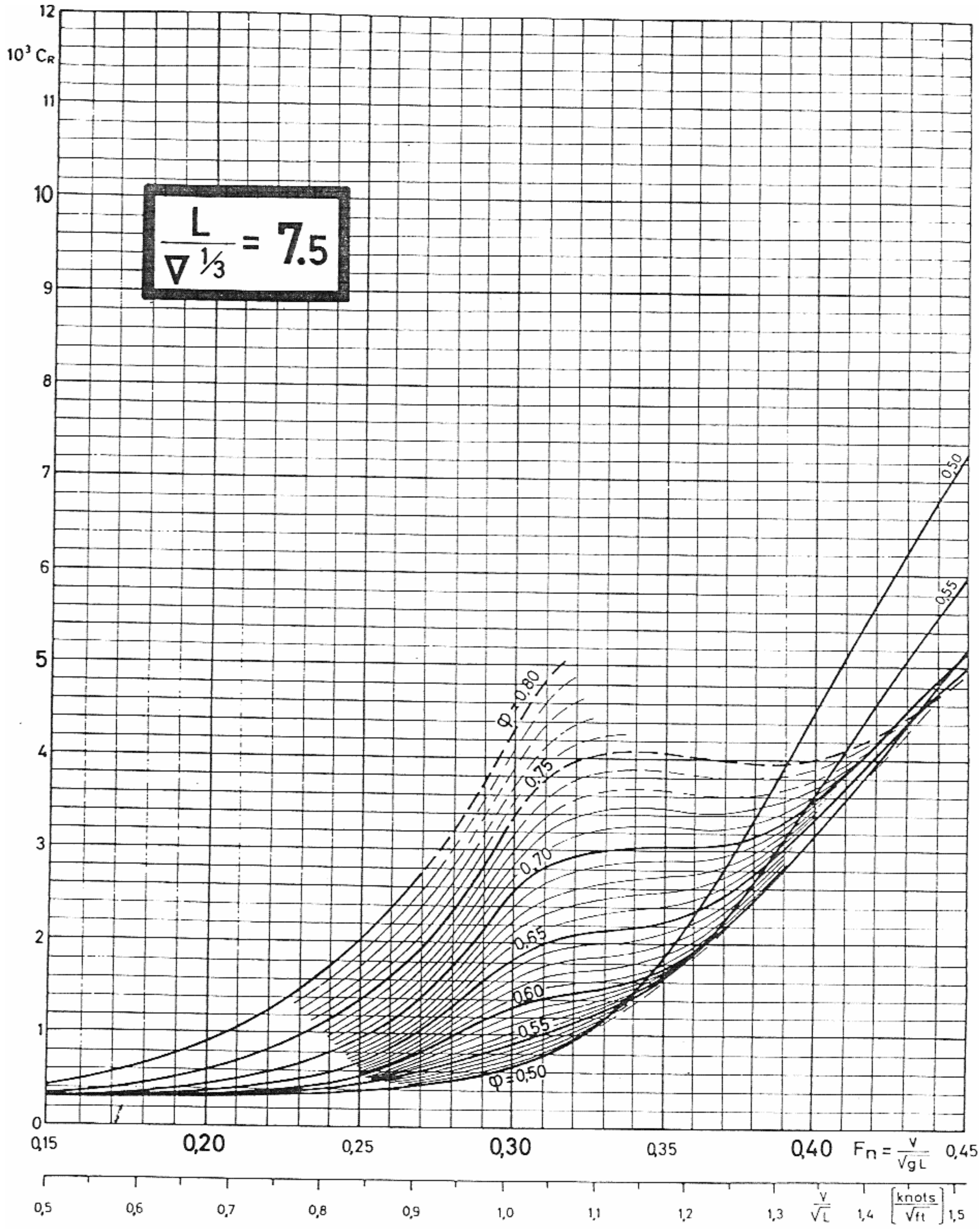

Figure A.8: Residuary resistance coefficient versus length Froude number for different values of longitudinal prismatic coefficient. $M = 7.5$. Source: Harvald (1983).

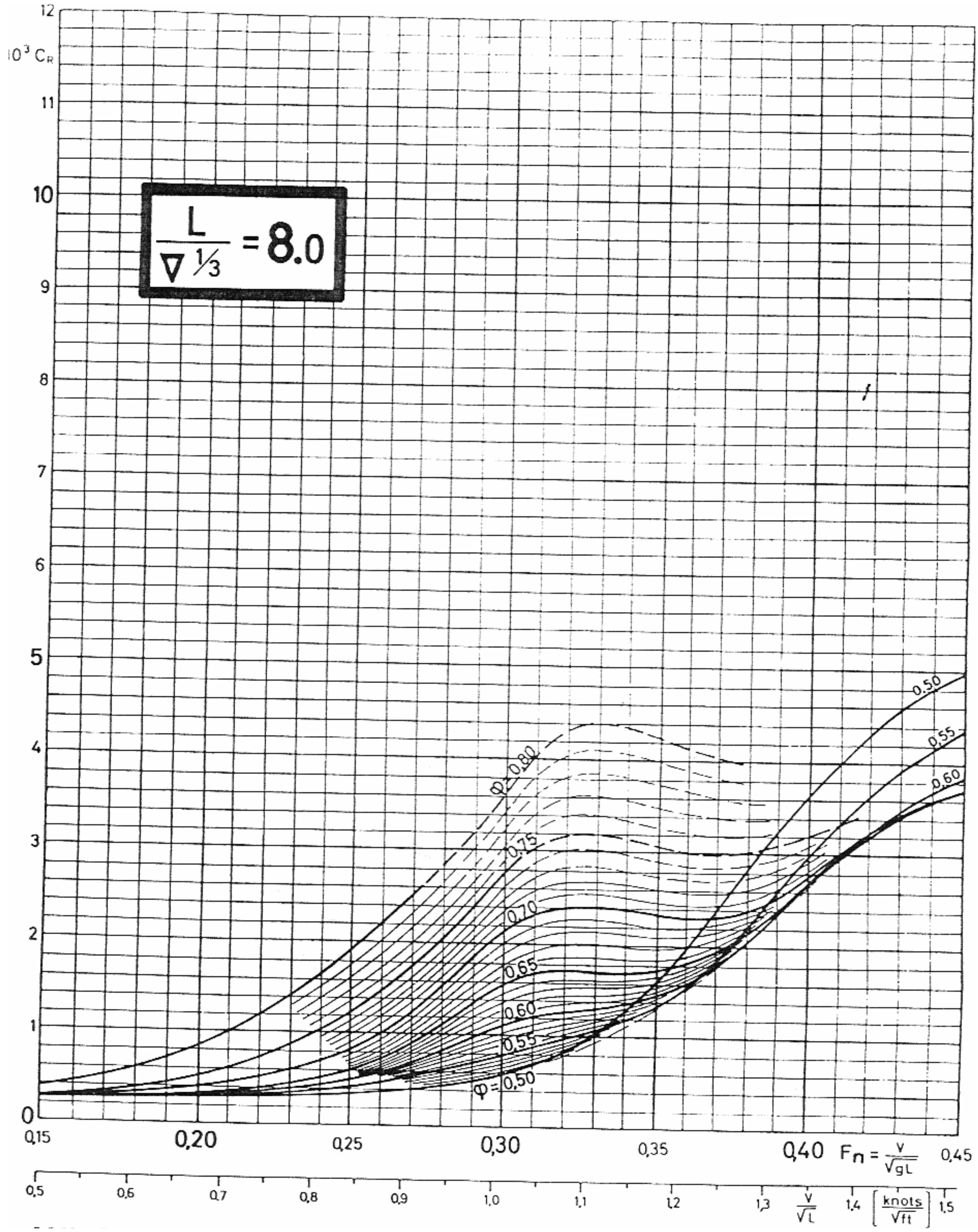

Figure A.9: Residuary resistance coefficient versus length Froude number for different values of longitudinal prismatic coefficient. $M = 8.0$. Source: Harvald (1983).

APPENDIX B – RESULTS OF THE 2700 TDW INLAND VESSEL RESISTANCE IN SHALLOW WATERS

In this appendix is presented the offset of the vessel, the original lines plan, the characteristic of the model in test condition and resistance results, made by IPT (1974). Also, is shown the empirical results of the ship model.

Characteristic	**Full scale**	**Model scale**
Water line length (m)	83.86	4.193
Beam (m)	14.50	0.725
Displacement (m^3)	3560.00	0.445
Draft (m)	3.20	0.160
Wetted surface (m^2)	1564.40	3.911

Table B.1: Characteristics of 2700 TDW inland vessel in full and in model scale. Source: IPT (1974)

Characteristic	**Value**
Model scale	0.05
Turbulence coefficient	0.00
Number of test	6
Temperature (C)	21.6
Water density ($kg \cdot s^2/m^4$)	201.75
Viscosity (m^2/s)	0.96895E-06
Roughness coefficient	0.40E-03
Block factor	1.00
Form factor	1.00

Table B.2: Characteristics of experimental test. Source: IPT (1974)

Test	v_{model} (m/s)	R_{model} (kgf)	v_{ship} (knot)	R_{ship} (kgf)	EHP	EHP/Λ (EHP/m^3)	Re_{model}
1	0.345	0.253	3.00	1,712	35	0.991E-02	0.149E+07
2	0.460	0.436	4.00	2,979	81	0.230E-01	0.199E+07
3	0.576	0.703	5.00	4,879	167	0.470E-01	0.249E+07
4	0.691	1.151	6.00	8,192	337	0.948E-01	0.299E+07
5	0.806	1.704	7.00	12,312	591	0.166E+00	0.349E+07
6	0.921	2.623	8.00	19,330	1,061	0.298E+00	0.399E+07
Test	$\frac{v}{\sqrt{L_{pp}}}$	$C_{\nu_{\text{model}}}$	$C_{\nu_{\text{model}}}$ (15 C.)	C_w	$C_{t_{\text{model}}}$	$C_{\nu_{\text{ship}}}$	$C_{t_{\text{ship}}}$
1	0.181	0.409E-02	0.421E-02	0.658E-02	0.108E-01	0.244E-02	0.901E-02
2	0.241	0.387E-02	0.399E-02	0.646E-02	0.105E-01	0.236E-02	0.882E-02
3	0.301	0.372E-02	0.383E-02	0.694E-02	0.108E-01	0.230E-02	0.924E-02
4	0.362	0.360E-02	0.371E-02	0.852E-02	0.122E-01	0.225E-02	0.108E-01
5	0.422	0.351E-02	0.361E-02	0.968E-02	0.133E-01	0.221E-02	0.119E-01
6	0.482	0.342E-02	0.352E-02	0.121E-01	0.156E-01	0.218E-02	0.143E-01

Table B.3: Experimental results of 2700 TDW inland vessel resistance test for condition 2. Source: IPT (1974)

x	y	z	x	y	z	x	y	z
Station 0.0000			Station 4.2355			Station 8.4710		
0.0000	0.0000	5.0250	4.2355	0.0000	1.5624	8.4710	0.0000	0.1538
0.0000	0.0000	5.7000	4.2355	1.6325	1.5624	8.4710	1.6325	0.1538
0.0000	1.6325	5.6625	4.2355	3.2650	1.5624	8.4710	3.2650	0.1538
0.0000	3.2650	5.6250	4.2355	4.8975	1.5624	8.4710	4.8975	0.1538
0.0000	4.8975	5.5875	4.2355	6.5300	1.5624	8.4710	6.5300	0.1538
0.0000	6.5300	5.5500	4.2355	6.7100	1.7381	8.4710	6.7100	0.3294
0.0000	6.5300	4.9125	4.2355	6.8900	1.9138	8.4710	6.8900	0.5049
0.0000	6.5300	4.2750	4.2355	7.0700	2.0895	8.4710	7.0700	0.6805
0.0000	6.5300	3.6375	4.2355	7.2500	2.2651	8.4710	7.2500	0.8561
0.0000	6.5300	3.0000	4.2355	7.2500	3.0739	8.4710	7.2500	2.0170
0.0000	4.8975	3.0000	4.2355	7.2500	3.8826	8.4710	7.2500	3.1780
0.0000	3.2650	3.0000	4.2355	7.2500	4.6913	8.4710	7.2500	4.3390
0.0000	1.6325	3.0000	4.2355	7.2500	5.5000	8.4710	7.2500	5.5000
0.0000	0.0000	3.0000	4.2355	5.4375	5.5500	8.4710	5.4375	5.5500
0.0000	0.0000	3.6750	4.2355	3.6250	5.6000	8.4710	3.6250	5.6000
0.0000	0.0000	4.3500	4.2355	1.8125	5.6500	8.4710	1.8125	5.6500
0.0000	0.0000	5.0250	4.2355	0.0000	5.7000	8.4710	0.0000	5.7000
Station 12.7065			Station 16.9420			Station 21.1775		
12.7065	0.0000	0.0000	16.9420	0.0000	0.0000	21.1775	0.0000	0.0000
12.7065	1.6327	0.0000	16.9420	1.6331	0.0000	21.1775	1.6334	0.0000
12.7065	3.2655	0.0000	16.9420	3.2662	0.0000	21.1775	3.2668	0.0000

Table B.4 – Offset of 2700 TDW inland vessel. Source: Author. *Continued on next page*

Continued from previous page

x	y	z	x	y	z	x	y	z
12.7065	4.8982	0.0000	16.9420	4.8992	0.0000	21.1775	4.9003	0.0000
12.7065	6.5309	0.0000	16.9420	6.5323	0.0000	21.1775	6.5337	0.0000
12.7065	6.7107	0.1726	16.9420	6.7117	0.1728	21.1775	6.7128	0.1730
12.7065	6.8905	0.3452	16.9420	6.8912	0.3456	21.1775	6.8918	0.3459
12.7065	7.0702	0.5179	16.9420	7.0706	0.5184	21.1775	7.0709	0.5189
12.7065	7.2500	0.6905	16.9420	7.2500	0.6912	21.1775	7.2500	0.6918
12.7065	7.2500	1.7179	16.9420	7.2500	1.7184	21.1775	7.2500	1.7189
12.7065	7.2500	2.7452	16.9420	7.2500	2.7456	21.1775	7.2500	2.7459
12.7065	7.2500	3.7726	16.9420	7.2500	3.7728	21.1775	7.2500	3.7730
12.7065	7.2500	4.8000	16.9420	7.2500	4.8000	21.1775	7.2500	4.8000
12.7065	5.4375	4.8000	16.9420	5.4375	4.8000	21.1775	5.4375	4.8000
12.7065	3.6250	4.8000	16.9420	3.6250	4.8000	21.1775	3.6250	4.8000
12.7065	1.8125	4.8000	16.9420	1.8125	4.8000	21.1775	1.8125	4.8000
12.7065	0.0000	4.8000	16.9420	0.0000	4.8000	21.1775	0.0000	4.8000
Station 25.4130			Station 29.6485			Station 33.8840		
25.4130	0.0000	0.0000	29.6485	0.0000	0.0000	33.8840	0.0000	0.0000
25.4130	1.6338	0.0000	29.6485	1.6341	0.0000	33.8840	1.6344	0.0000
25.4130	3.2675	0.0000	29.6485	3.2682	0.0000	33.8840	3.2689	0.0000
25.4130	4.9013	0.0000	29.6485	4.9023	0.0000	33.8840	4.9033	0.0000
25.4130	6.5350	0.0000	29.6485	6.5364	0.0000	33.8840	6.5378	0.0000
25.4130	6.7138	0.1731	29.6485	6.7148	0.1733	33.8840	6.7158	0.1735
25.4130	6.8925	0.3463	29.6485	6.8932	0.3466	33.8840	6.8939	0.3469
25.4130	7.0713	0.5194	29.6485	7.0716	0.5199	33.8840	7.0719	0.5204
25.4130	7.2500	0.6925	29.6485	7.2500	0.6932	33.8840	7.2500	0.6939
25.4130	7.2500	1.7194	29.6485	7.2500	1.7199	33.8840	7.2500	1.7204
25.4130	7.2500	2.7463	29.6485	7.2500	2.7466	33.8840	7.2500	2.7469
25.4130	7.2500	3.7731	29.6485	7.2500	3.7733	33.8840	7.2500	3.7735
25.4130	7.2500	4.8000	29.6485	7.2500	4.8000	33.8840	7.2500	4.8000
25.4130	5.4375	4.8000	29.6485	5.4375	4.8000	33.8840	5.4375	4.8000
25.4130	3.6250	4.8000	29.6485	3.6250	4.8000	33.8840	3.6250	4.8000
25.4130	1.8125	4.8000	29.6485	1.8125	4.8000	33.8840	1.8125	4.8000
25.4130	0.0000	4.8000	29.6485	0.0000	4.8000	33.8840	0.0000	4.8000
Station 38.1195			Station 42.3550			Station 46.5905		
38.1195	0.0000	0.0000	42.3550	0.0000	0.0000	46.5905	0.0000	0.0000
38.1195	1.6348	0.0000	42.3550	1.6351	0.0000	46.5905	1.6355	0.0000
38.1195	3.2696	0.0000	42.3550	3.2702	0.0000	46.5905	3.2709	0.0000
38.1195	4.9043	0.0000	42.3550	4.9054	0.0000	46.5905	4.9064	0.0000
38.1195	6.5391	0.0000	42.3550	6.5405	0.0000	46.5905	6.5418	0.0000
38.1195	6.7168	0.1736	42.3550	6.7179	0.1738	46.5905	6.7189	0.1740
38.1195	6.8946	0.3473	42.3550	6.8952	0.3476	46.5905	6.8959	0.3480

Table B.4 – Offset of 2700 TDW inland vessel. Source: Author. *Continued on next page*

Continued from previous page

x	y	z	x	y	z	x	y	z
38.1195	7.0723	0.5209	42.3550	7.0726	0.5214	46.5905	7.0730	0.5219
38.1195	7.2500	0.6946	42.3550	7.2500	0.6952	46.5905	7.2500	0.6959
38.1195	7.2500	1.7209	42.3550	7.2500	1.7214	46.5905	7.2500	1.7219
38.1195	7.2500	2.7473	42.3550	7.2500	2.7476	46.5905	7.2500	2.7480
38.1195	7.2500	3.7736	42.3550	7.2500	3.7738	46.5905	7.2500	3.7740
38.1195	7.2500	4.8000	42.3550	7.2500	4.8000	46.5905	7.2500	4.8000
38.1195	5.4375	4.8000	42.3550	5.4375	4.8000	46.5905	5.4375	4.8000
38.1195	3.6250	4.8000	42.3550	3.6250	4.8000	46.5905	3.6250	4.8000
38.1195	1.8125	4.8000	42.3550	1.8125	4.8000	46.5905	1.8125	4.8000
38.1195	0.0000	4.8000	42.3550	0.0000	4.8000	46.5905	0.0000	4.8000
Station 50.8260			Station 55.0615			Station 59.2970		
50.8260	0.0000	0.0000	55.0615	0.0000	0.0000	59.2970	0.0000	0.0000
50.8260	1.6358	0.0000	55.0615	1.6361	0.0000	59.2970	1.6365	0.0000
50.8260	3.2716	0.0000	55.0615	3.2723	0.0000	59.2970	3.2730	0.0000
50.8260	4.9074	0.0000	55.0615	4.9084	0.0000	59.2970	4.9094	0.0000
50.8260	6.5432	0.0000	55.0615	6.5446	0.0000	59.2970	6.5459	0.0000
50.8260	6.7199	0.1742	55.0615	6.7209	0.1743	59.2970	6.7219	0.1745
50.8260	6.8966	0.3483	55.0615	6.8973	0.3486	59.2970	6.8980	0.3490
50.8260	7.0733	0.5225	55.0615	7.0736	0.5230	59.2970	7.0740	0.5235
50.8260	7.2500	0.6966	55.0615	7.2500	0.6973	59.2970	7.2500	0.6980
50.8260	7.2500	1.7225	55.0615	7.2500	1.7230	59.2970	7.2500	1.7235
50.8260	7.2500	2.7483	55.0615	7.2500	2.7486	59.2970	7.2500	2.7490
50.8260	7.2500	3.7742	55.0615	7.2500	3.7743	59.2970	7.2500	3.7745
50.8260	7.2500	4.8000	55.0615	7.2500	4.8000	59.2970	7.2500	4.8000
50.8260	5.4375	4.8000	55.0615	5.4375	4.8000	59.2970	5.4375	4.8000
50.8260	3.6250	4.8000	55.0615	3.6250	4.8000	59.2970	3.6250	4.8000
50.8260	1.8125	4.8000	55.0615	1.8125	4.8000	59.2970	1.8125	4.8000
50.8260	0.0000	4.8000	55.0615	0.0000	4.8000	59.2970	0.0000	4.8000
Station 63.5325			Station 67.7680			Station 72.0035		
63.5325	0.0000	0.0000	67.7680	0.0000	0.0000	72.0035	0.0000	0.0000
63.5325	1.6368	0.0000	67.7680	1.6372	0.0000	72.0035	1.6374	0.0000
63.5325	3.2736	0.0000	67.7680	3.2743	0.0000	72.0035	3.2748	0.0000
63.5325	4.9105	0.0000	67.7680	4.9115	0.0000	72.0035	4.9122	0.0000
63.5325	6.5473	0.0000	67.7680	6.5486	0.0000	72.0035	6.5496	0.0000
63.5325	6.7230	0.1747	67.7680	6.7240	0.1748	72.0035	6.7247	0.1750
63.5325	6.8986	0.3493	67.7680	6.8993	0.3497	72.0035	6.8998	0.3500
63.5325	7.0743	0.5240	67.7680	7.0747	0.5245	72.0035	7.0749	0.5250
63.5325	7.2500	0.6986	67.7680	7.2500	0.6993	72.0035	7.2500	0.7000
63.5325	7.2500	1.7240	67.7680	7.2500	1.7245	72.0035	7.2500	1.7250
63.5325	7.2500	2.7493	67.7680	7.2500	2.7497	72.0035	7.2500	2.7500

Table B.4 – Offset of 2700 TDW inland vessel. Source: Author. *Continued on next page*

Continued from previous page

x	y	z	x	y	z	x	y	z
63.5325	7.2500	3.7747	67.7680	7.2500	3.7748	72.0035	7.2500	3.7750
63.5325	7.2500	4.8000	67.7680	7.2500	4.8000	72.0035	7.2500	4.8000
63.5325	5.4375	4.8000	67.7680	5.4375	4.8000	72.0035	5.4375	4.8000
63.5325	3.6250	4.8000	67.7680	3.6250	4.8000	72.0035	3.6250	4.8000
63.5325	1.8125	4.8000	67.7680	1.8125	4.8000	72.0035	1.8125	4.8000
63.5325	0.0000	4.8000	67.7680	0.0000	4.8000	72.0035	0.0000	4.8000
Station 76.2390			Station 80.4745					
76.2390	0.0000	0.0000	80.4745	0.0000	0.0000			
76.2390	1.4864	0.0000	80.4745	0.7824	0.0000			
76.2390	2.9729	0.0000	80.4745	1.5648	0.0000			
76.2390	4.4593	0.0000	80.4745	2.3471	0.0000			
76.2390	5.9458	0.0000	80.4745	3.1295	0.0000			
76.2390	6.1282	0.1750	80.4745	3.4147	0.2171			
76.2390	6.3107	0.3500	80.4745	3.6999	0.4341			
76.2390	6.4931	0.5250	80.4745	3.9851	0.6512			
76.2390	6.6756	0.7000	80.4745	4.2703	0.8683			
76.2390	6.7334	1.8756	80.4745	4.4927	2.1390			
76.2390	6.7913	3.0513	80.4745	4.7150	3.4097			
76.2390	6.8491	4.2269	80.4745	4.9373	4.6804			
76.2390	6.9070	5.4026	80.4745	5.1596	5.9511			
76.2390	5.1802	5.4026	80.4745	3.8697	5.9511			
76.2390	3.4535	5.4026	80.4745	2.5798	5.9511			
76.2390	1.7267	5.4026	80.4745	1.2899	5.9511			
76.2390	0.0000	5.4026	80.4745	0.0000	5.9511			

Table B.4: Offset of 2700 TDW inland vessel. Source: Author.

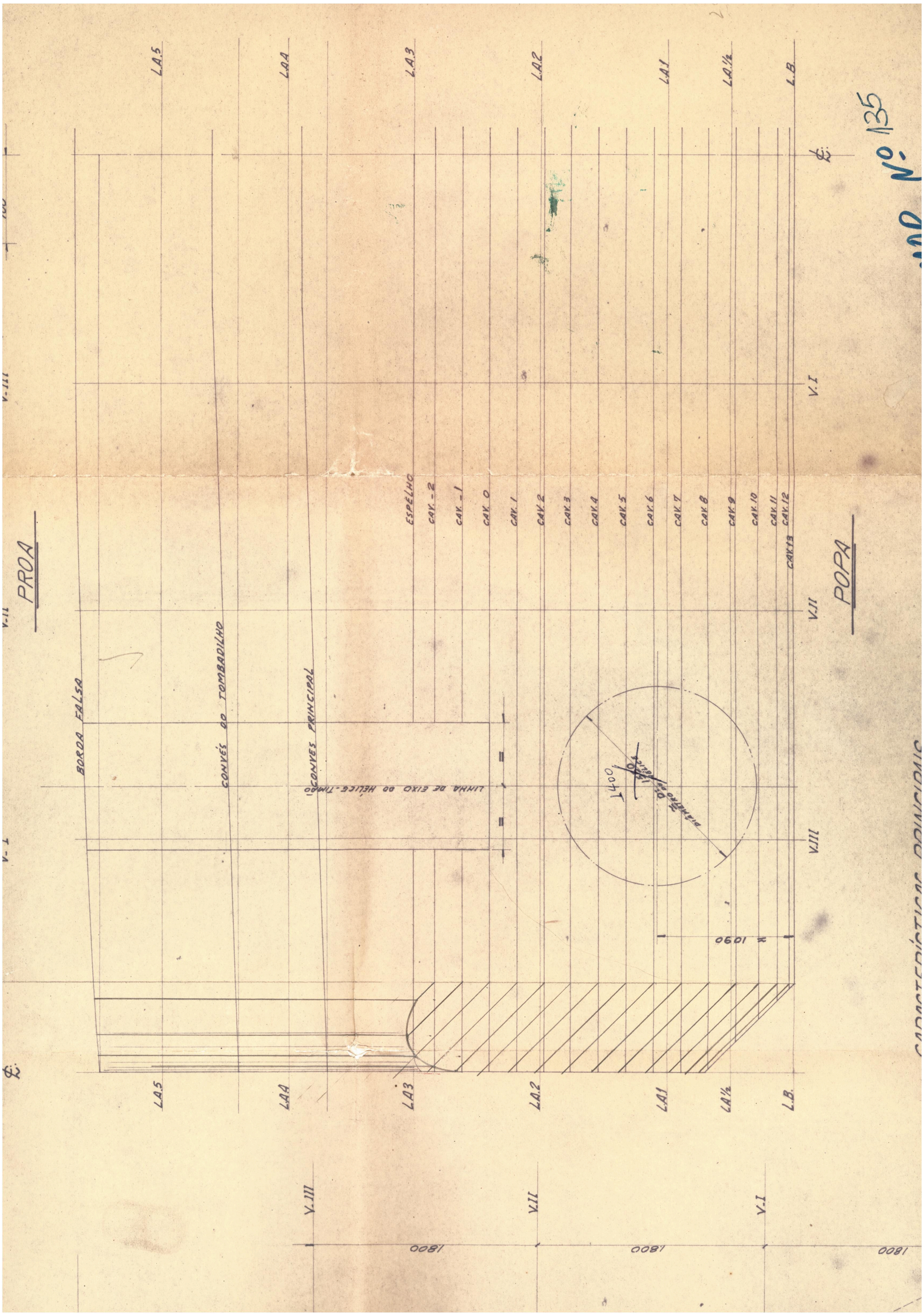

Figure B.1: 2700 TDW original inland vessel lines-plan (stern view). Source: (IPT, 1974).

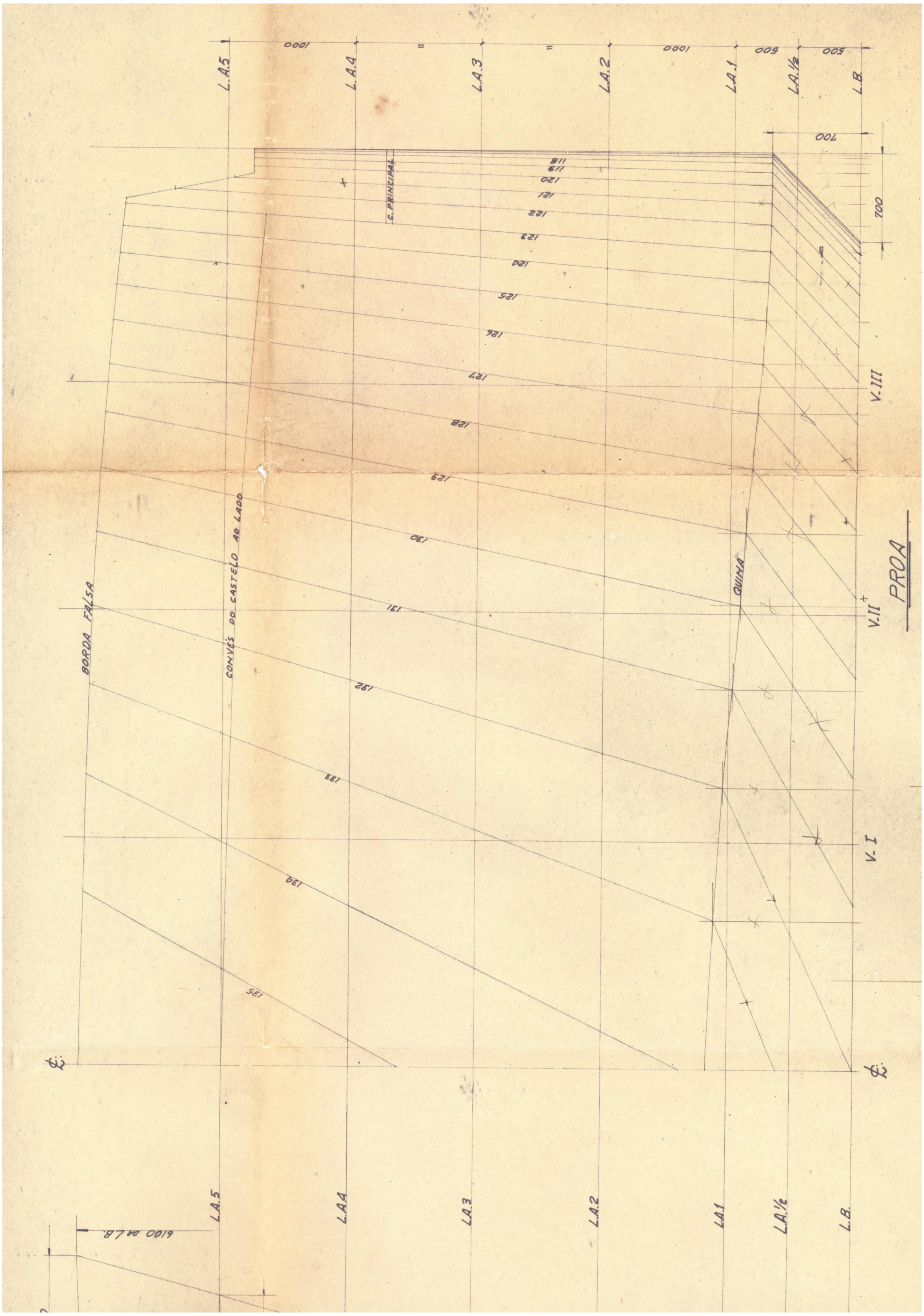

Figure B.2: 2700 TDW inland vessel original lines-plan (bow view). Source: (IPT, 1974).

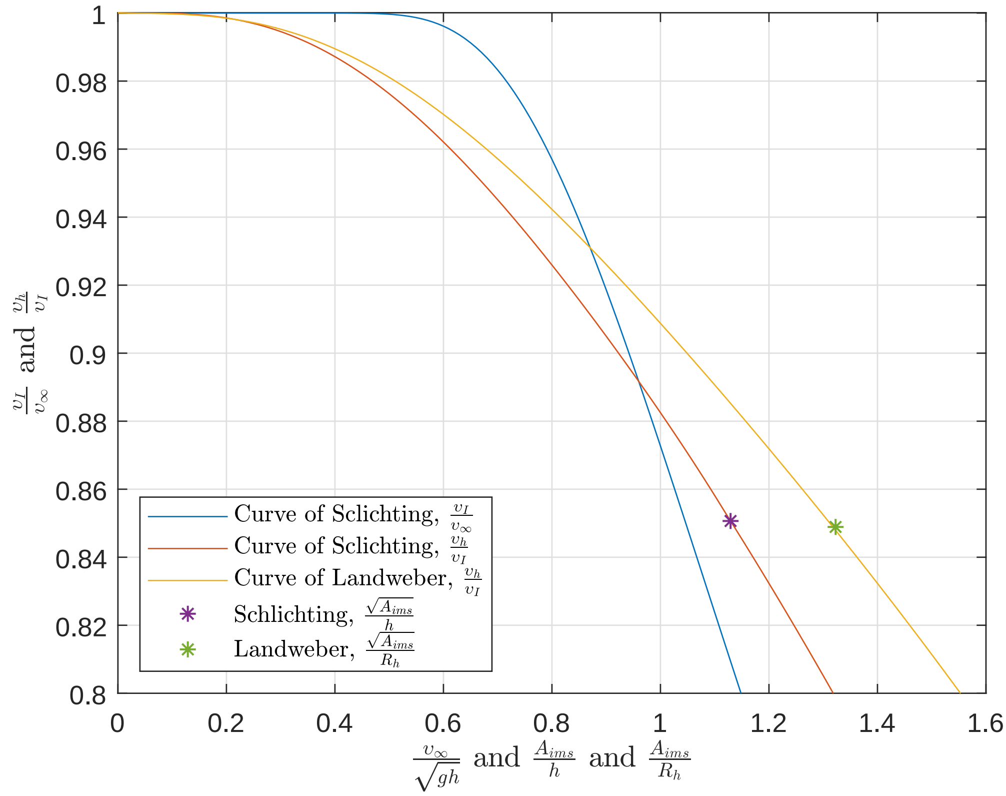

Figure B.3: Schlichting's curves applied to 2700 TDW inland vessel, where is indicated the values of $A_{ims}^{1/2}/h$ and $A_{ims}^{1/2}/R_h$ of the ship. Source: Author.

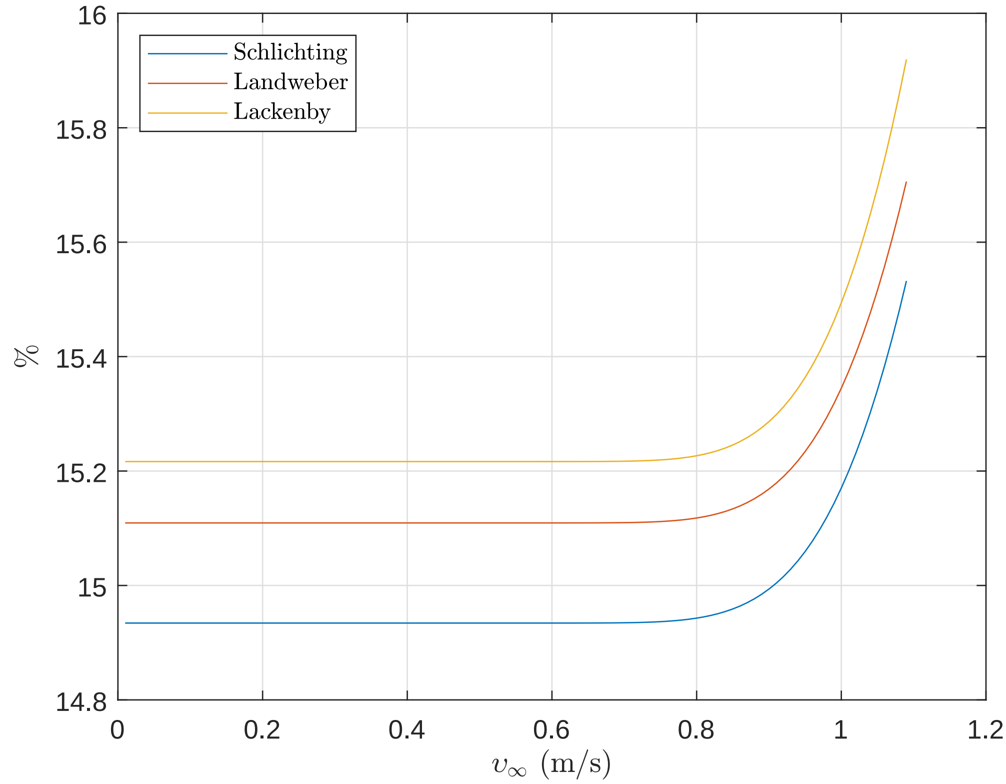

Figure B.4: Loss in velocities using empirical method for large rivers applied to 2700 TDW inland vessel. Source: Author.

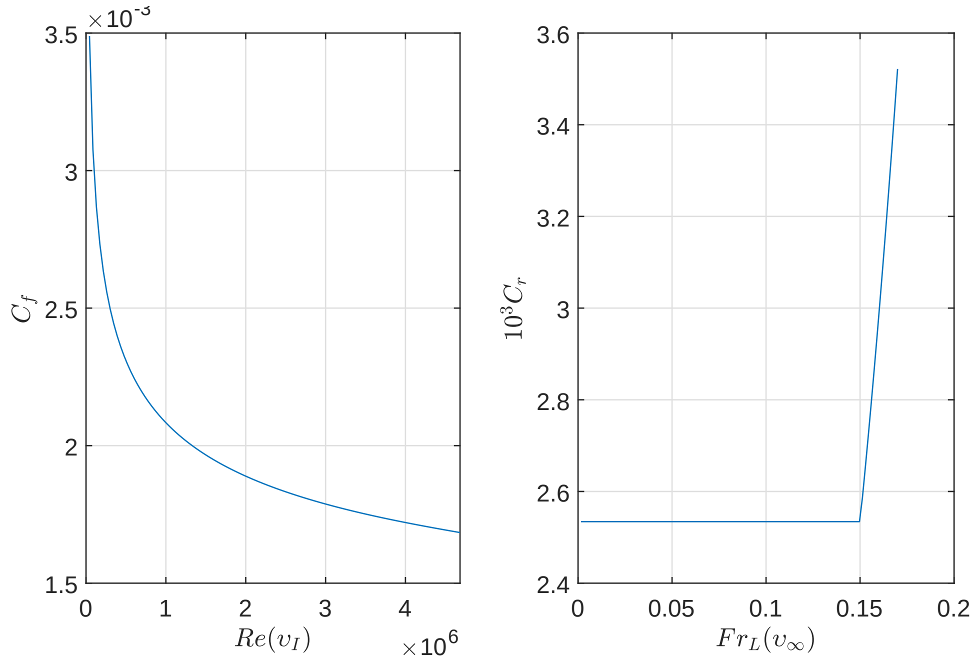

Figure B.5: Coefficient forces for large rivers of the 2700 TDW inland vessel. Source: Author.

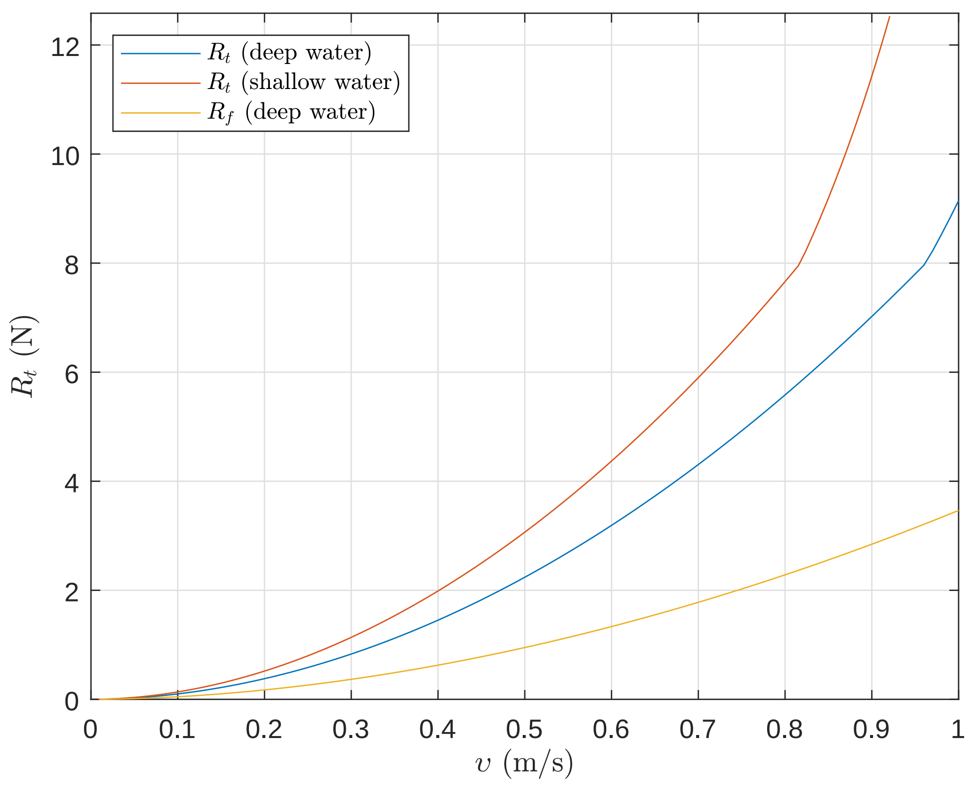

Figure B.6: Total resistance using Schlichting's method in comparison with Froude hypothesis ship resistance of the 2700 TDW inland vessel. Source: Author.

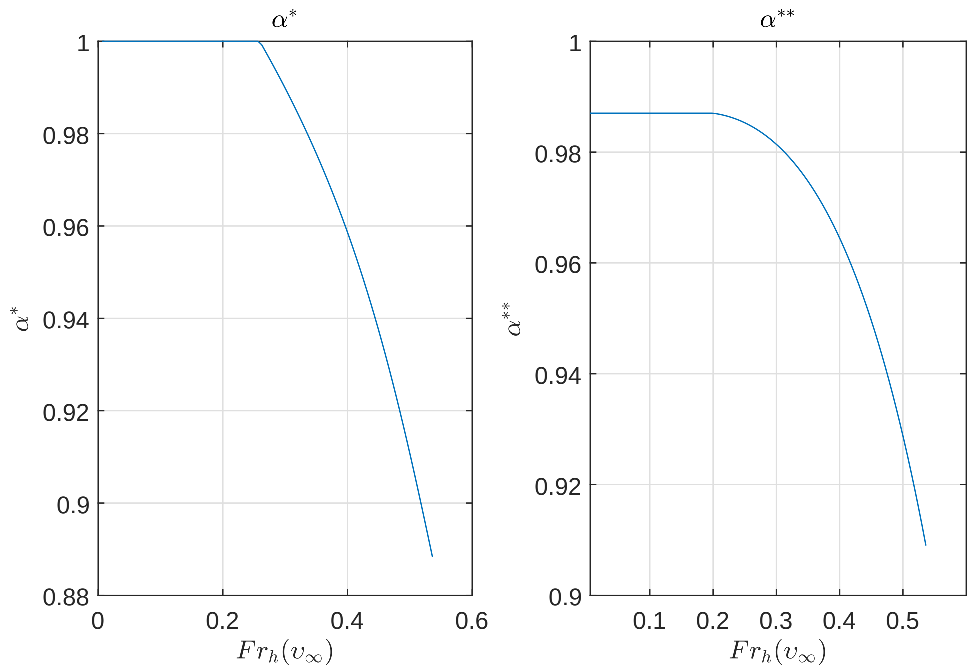

Figure B.7: Karvop's diagrams for 2700 TDW inland vessel.

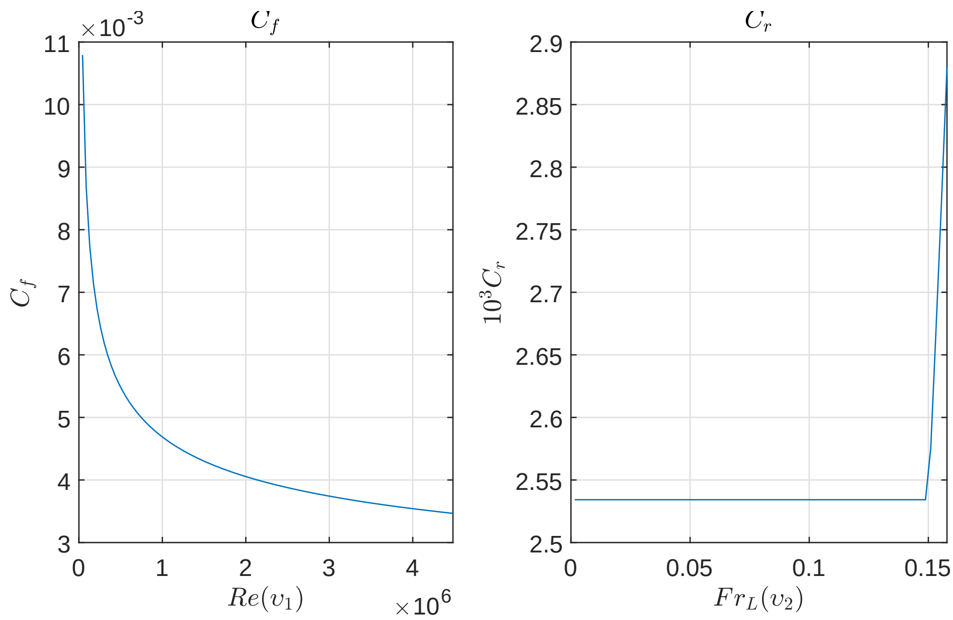

Figure B.8: Coefficient forces for middle rivers of the 2700 TDW inland vessel. Source: Author.

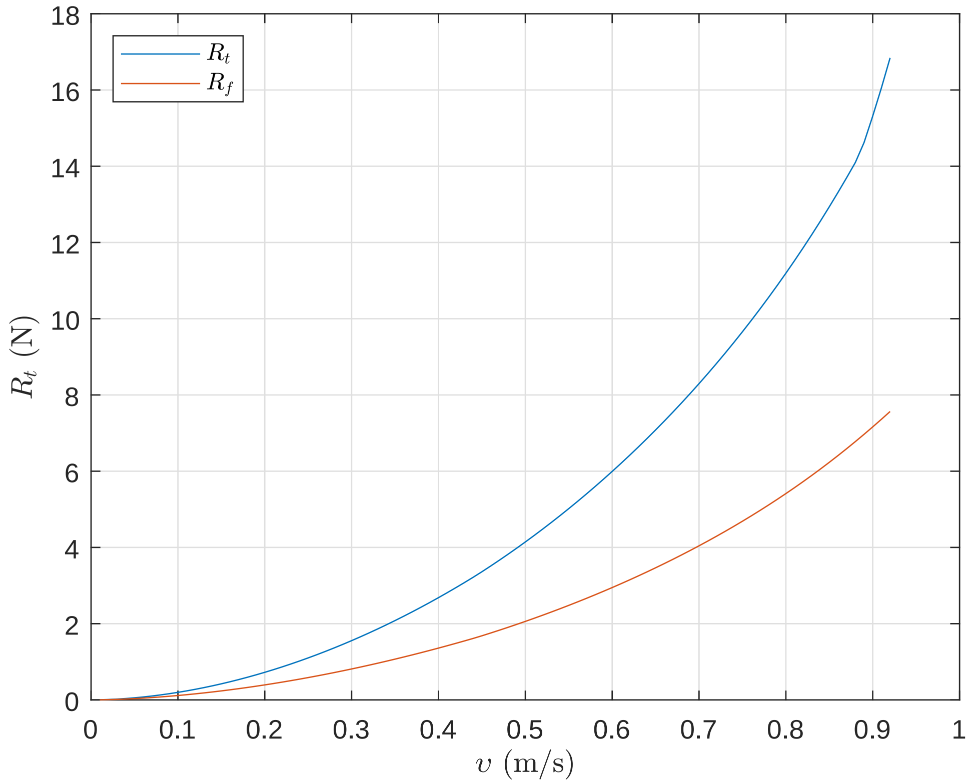

Figure B.9: Total forces for middle rivers of the 2700 TDW inland vessel. Source: Author.

APPENDIX C – CODES

In this appendix is shown the codes made on *MATLAB*.

C.1 Schlichting's method

```
%% Evaluation of resistance of inland vessel 2700 TDW using Schlichting's method
% In this alghorithm, the calculation of the inland vessel resistance is
% based on Schlicting's method, where the loss in velocity is calculated.
% The components of the resistance is composed by Froude's hypothesis.
%---------------------------------------------------------------------------

%% Initial comands
% Always is checked the command windows and variables are clear, and
% the windows opened in MATLAB are being close.

clc % Clear command windows
clear % Clear all variables
close all % Close all windows

%% Initial variables

% Only variables that can apply to this method are the gravity and
% kinematic viscosity at 21.6 C.

g = 9.81; % Gravity ( m / s^2 )
nu = 0.96895 * 10^(-6); % Kinematic viscosity ( m^2 / s )7
rho = 101.75 * g; % Density of water ( kg / m^3 )

%---------------------------------------------------------------------------

% Also, the variables of the towing tank.
Scale = 1 / 20; % Model scale.
h = 6 * Scale; % False depth of the tank ( m )

%---------------------------------------------------------------------------

% Finally, the characteristics of the inland vessel are
L_pp =     83.860 * Scale; % Length in the water line ( m )
B =        14.500 * Scale; % Beam ( m )
T =         3.200 * Scale; % Stern ( m )
```

```
S =     1630.500 * Scale^2; % Wetted surface area ( m^2 )
Nabla = 3504.400 * Scale^3; % Displacement volume ( m^3 )
A_ms =    45.906 * Scale^2; % Midship section area ( m^2 )

% Velocity of the inland vessel model ( m / s )
V_inf_1 = 0.01:0.01:1.09; %Velocity of the inland vessel model
V_inf = V_inf_1'; %Transpose of the velocity vector

%% Calcation of the inland vessel resistance, condition 2.
beta = A_ms / ( B * T ); % Midship section area coefficient
phi = Nabla / ( L_pp * B * T * beta ); % Prismatic coefficient
ratio_L_Nabla_3 = L_pp / Nabla^( 1 / 3 ); % Ratio between model length and
% volume displacement
ratio_B_T = B / T; % Ratio between model beam and draft
ratio_A_ms_h = sqrt( A_ms ) / h; %Ratio between midship section area of the
% vessel and depth
j = length( V_inf ); % Length of the velocity vector

%--------------------------------------------------------------------------

% Calculation of the ratio between midship section area and the depth using
% Schlichting's diagram.
if ratio_A_ms_h <= 1.11
    ratio_V_h_V_I = - 0.0155 * ratio_A_ms_h^6 - 0.0897 * ...
        ratio_A_ms_h^5 + 0.3867 * ratio_A_ms_h^4 - 0.4418 * ...
        ratio_A_ms_h^3 + 0.0441 * ratio_A_ms_h^2 - 0.0013 * ...
        ratio_A_ms_h + 1;
else
    ratio_V_h_V_I = - 0.0716 * ratio_A_ms_h^2 - 0.0924 * ratio_A_ms_h ...
        + 1.0463;
end

%--------------------------------------------------------------------------
% Variables that can calculate the residual resistance coefficient. These
% equations are the extrapolation of the Guldhammer and Harvald (1974) and
% is deteremінated by Georgagaki and Sorenson (2004).

A_0 = 1.35 - 0.23 * ratio_L_Nabla_3 + 0.012 * ratio_L_Nabla_3^2;
A_1 = 0.0011 * ratio_L_Nabla_3^( 9.1 );
N_1 = 2 * ratio_L_Nabla_3 - 3.7;
B_1 = 7 - 0.09 * ratio_L_Nabla_3^2;
B_2 = ( 5 * phi - 2.5 )^2;

%--------------------------------------------------------------------------
% Looping variables. Initially are empty with zero.
Re = zeros; % Reynolds number
C_f = zeros; % Frictional resistance coefficient.
Fr_L = zeros; % Length Froude number
Fr_h = zeros; % Depth Froude number
E = zeros; % Variable used for the calculation of the residual resistance
% coefficient.
B_3 = zeros; %Variable used for the calculation of the residual resistance
% coefficient
G = zeros; %Variable used for the calculation of the residual resistance
```

```
% coefficient
H = zeros; %Variable used for the calculation of the residual resistance
% coefficient
K = zeros; %Variable used for the calculation of the residual resistance
% coefficient
C_r_25_10_3 = zeros; % 10^3 Residual resistance coefficient if B/T = 2.5
C_r_10_3 = zeros; % 10^3 Residual resistance coefficient
C_r = zeros; % Residual resistance coefficient
R_f = zeros; % Frictional resistance
R_r = zeros; % Residuary resistance
R_t = zeros; % Total resistance

V_I = zeros; % Intermediate velocity
Re_V_I = zeros; % Reynolds number in intermediate velocity
C_f_V_I = zeros; % Frictional resistance in intermediate velocity
Fr_L_V_I = zeros; % Length Froude number in intermediate velocity
Fr_h_V_I = zeros; % Depth Froude number in intermediate velocity
R_f_V_I = zeros; % Frictional resistance in intermediate velocity

V_h = zeros; % Velocity in shallow water
dV_V = zeros; % Velocity loss
Fr_L_V_h = zeros; % Length Froude number in shallow water
Fr_h_V_h = zeros; % Depth Froude number in shallow water
R_t_V_h = zeros; % Total resistance in shallow waters

% Looping the calculation of the resistance in shallow waters
%--------------------------------------------------------------------------

for k=1:j
    % Calculation of the resistance in deep water
    Re(k,1) = L_pp * V_inf(k,1) / nu; % Reynolds number
    C_f(k,1) = 0.075 / ( log10( Re(k,1) - 2 ) )^2; % Frictional resistance
    % coefficient
    Fr_L(k,1) = V_inf(k,1) / sqrt( g * L_pp ); % Length Froude number
    Fr_h(k,1) = V_inf(k,1) / sqrt( g * h ); % Depth Froude number

    % Calculation of the residual resistance in deep water
    if Fr_L(k,1) <= 0.15 % C_r is constant.
        E(k,1) = ( A_0 + 1.5 * 0.15^( 1.8 ) + A_1 * 0.15^( N_1 ) ) * ...
            ( 0.98 + 2.5 / ( ratio_L_Nabla_3 - 2 )^4 ) + ...
            ( ratio_L_Nabla_3 - 5 )^4 * ( 0.15 - 0.1 )^4;
        B_3(k,1) = ( 600 * ( 0.15 - 0.315 )^2 + 1 )^( 1.5 );
        G(k,1) = B_1 * B_2 / B_3(k,1);
        H(k,1) = exp( 80 * ( 0.15 - ( 0.04 + 0.59 * phi ) - ...
            ( 0.015 * ( ratio_L_Nabla_3 - 5 ) ) ) );
        K(k,1) = 180 * 0.15^( 3.7 ) * exp( 20 * phi - 16 );
        if ratio_B_T == 2.5
            C_r_25_10_3(k,1) = E(k,1) + G(k,1) + H(k,1) + K(k,1);
            C_r_10_3(k,1) = C_r_25_10_3(k,1);
            C_r(k,1) = C_r_10_3(k,1) / 10^3; % Residuary resistance coef.
        else
            C_r_25_10_3(k,1) = E(k,1) + G(k,1) + H(k,1) + K(k,1);
            C_r_10_3(k,1) = C_r_25_10_3(k,1) + 0.16 * ( ratio_B_T - 2.5 );
            C_r(k,1) = C_r_10_3(k,1) / 10^3; % Residuary resistance coef.
```

```
        end
    else % C_r is a function.
        E(k,1) = ( A_0 + 1.5 * Fr_L(k,1)^( 1.8 ) + A_1 * Fr_L(k,1)^(...
            N_1 ) ) * ( 0.98 + 2.5 / ( ratio_L_Nabla_3 - 2 )^4 ) + ...
            ( ratio_L_Nabla_3 - 5 )^4 * ( Fr_L(k,1) - 0.1 )^4;
        B_3(k,1) = ( 600 * ( Fr_L(k,1) - 0.315 )^2 + 1 )^( 1.5 );
        G(k,1) = B_1 * B_2 / B_3(k,1);
        H(k,1) = exp( 80 * ( Fr_L(k,1) - ( 0.04 + 0.59 * phi ) - ...
            ( 0.015 * ( ratio_L_Nabla_3 - 5 ) ) ) );
        K(k,1) = 180 * Fr_L(k,1)^( 3.7 ) * exp( 20 * phi - 16 );
        if ratio_B_T == 2.5
            C_r_25_10_3(k,1) = E(k,1) + G(k,1) + H(k,1) + K(k,1);
            C_r_10_3(k,1) = C_r_25_10_3(k,1);
            C_r(k,1) = C_r_10_3(k,1) / 10^3; % Residuary resistance coef.
        else
            C_r_25_10_3(k,1) = E(k,1) + G(k,1) + H(k,1) + K(k,1);
            C_r_10_3(k,1) = C_r_25_10_3(k,1) + 0.16 * ( ratio_B_T - 2.5 );
            C_r(k,1) = C_r_10_3(k,1) / 10^3; % Residuary resistance coef.
        end
    end

    R_f(k,1) = 1 / 2 * rho * S * ( V_inf(k,1) )^2 * C_f(k,1); %Frictional
    % resistance
    R_r(k,1) = 1 / 2 * rho * S * ( V_inf(k,1) )^2 * C_r(k,1); %Residual
    % resistance
    R_t(k,1) = R_f(k,1) + R_r(k,1); %Total resistance

    % ---------------------------------------------------------------------
    % Calculation of the resistance in intermediate velocity
    V_I(k,1) = V_inf(k,1) * sqrt( tanh( g * h / ( V_inf(k,1) )^2 ) ); % Ca-
    % lculation of the intermediate velocity.
    Re_V_I(k,1) = L_pp * V_I(k,1) / nu; % Reynolds number
    C_f_V_I(k,1) = 0.075 / ( log10( Re_V_I(k,1) - 2 ) )^2; %Frictional res-
    % istance
    Fr_L_V_I(k,1) = V_I(k,1) / sqrt( g * L_pp ); % Length Froude number
    Fr_h_V_I(k,1) = V_I(k,1) / sqrt( g * h ); % Depth Froude number

    R_f_V_I(k,1) = 1 / 2 * rho * S * ( V_I(k,1) )^2 * C_f_V_I(k,1); %Frict-
    % ional resistance in intermediate velocity.

    % ---------------------------------------------------------------------
    % Velocity in shallow water
    V_h(k,1) = ratio_V_h_V_I * V_I(k,1); % Velocity in shallow water
    dV_V(k,1) = ( V_inf(k,1) - V_h(k,1) ) / V_inf(k,1) * 100; % Percentage
    % of the loss in velocity
    Fr_L_V_h(k,1) = V_h(k,1) / sqrt( g * L_pp ); % Length Froude number
    Fr_h_V_h(k,1) = V_h(k,1) / sqrt( g * h ); % Depth Froude number

    R_t_V_h(k,1) = R_f_V_I(k,1) + R_r(k,1); % Total resistance in shallow
    % waters
end

V = [ V_inf V_I V_h dV_V ]; % Matrix of the velocity
Re_M = [ Re Re_V_I ]; % Matrix of Reynolds number
```

```
C_M = [ C_f C_f_V_I C_r ] * 10^3; % Matrix of the resistance coefficients
Fr_L_M = [ Fr_L Fr_L_V_I Fr_L_V_h ]; % Matrix of length Froude number
Fr_h_M = [ Fr_h Fr_h_V_I Fr_h_V_h ]; % Matrix of depth Froude number
R_t_M = [ V R_f R_r R_t R_f_V_I R_r R_t_V_h ]; % Matrix of total resistance

%% Cuves of velocities ratios for calculating resistance in shallow waters
i = 0;
x_2 = 0:0.01:1.6;
x_1 = zeros(length(x_2),1);
y_Sch_f = zeros(length(x_2),1);
y_Sch_c = zeros(length(x_2),1);
y_Landweber_c = zeros(length(x_2),1);
for x = x_2
    i = i + 1;
    x_1(i,:) = x;
    y_Sch_f(i,:) = sqrt( tanh( ( 1 / x )^2 ) );

    %Schlichting's curve
    if x <= 1.11
        y_Sch_c(i,:) = - 0.0155 * x^6 - 0.0897 * x^5 + 0.3867 * x^4 ...
            - 0.4418 * x^3 + 0.0441 * x^2 - 0.0013 * x + 1;
    else
        y_Sch_c(i,:) = - 0.0716 * x^2 - 0.0924 * x + 1.0463;
    end

    %Landweber's curve
    if x <= 1.56
        y_Landweber_c(i,:) = 0.0269 * x^6 - 0.1664 * x^5 + 0.38267 ...
            * x^4 - 0.3729 * x^3 + 0.0429 * x^2 - 0.0045 * x + 1.0001;
    else
        y_Landweber_c(i,:) = - 0.1406 * x^2 - 0.2077 * x + 0.8177;
    end
end

%% Displaying in command window
% In this section, is displayed the results of the resistance calulation of
% the 2700 TDW inland vessel.

disp('Evaluation of resistance of inland vessel 2700 TDW using method of Schlichting')
disp('--------------------------------------------------------------------------------')

disp('Scale')
disp(Scale)

disp('Length of waterline - L_pp (m)')
disp(L_pp)

disp('Beam - B (m)')
disp(B)

disp('Draft - T (m)')
disp(T)

disp('Wetted surface of the hull - S (m^2)')
```

```
disp(S)

disp('Displacement - Nabla (m^3)')
disp(Nabla)

disp('Midship section area - A_ms (m^2)')
disp(A_ms)

disp('Depth of the tank (m)')
disp(h)

disp('Midship section area coefficient - beta')
disp(beta)

disp('Prismatic coefficient - phi')
disp(phi)

disp('Ratio between model length and volume displacement - L_pp / Nabla^3')
disp(ratio_L_Nabla_3)

disp('Ratio between model beam and draft - B / T')
disp(ratio_B_T)

disp('Ratio between Midship section area and depth - sqrt(A_ms) / h')
disp(ratio_A_ms_h)

disp('Ratio between velocity in shallow water and intermediate velocity - V_h / V_I')
disp(ratio_V_h_V_I)

disp('Velocity (m/s)')
disp('     V_inf      V_I        V_h      Losses (%)')
disp(V)

disp('Reynolds number - Re in function of')
disp('     V_inf      V_I')
disp(Re_M)

disp('Resistance coefficient * 10^3')
disp('     C_f        C_f_V_I    C_r')
disp(C_M)

disp('Length Froude number - Fr_L in function of')
disp('     V_inf      V_I        V_h')
disp(Fr_L_M)

disp('Depth Froude number - Fr_h in function of')
disp('     V_inf      V_I        V_h')
disp(Fr_h_M)

disp('Total resistance R_t')
disp('                                           |                    Total resistance (N)'
    )
disp('             Velocity (m/s)                |      Deep water            |
    Shallow water')
```

```
disp('     V_inf      V_I        V_h      Losses (%)    R_f        R_f        R_t       R_f_V_I       R_r      R_t_V_h')
disp(R_t_M)

%% Graphics

set (0,'defaulttextinterpreter','Latex'); %Fonte de letra LaTeX

figure('Name','Diagram of Schlichting')
plot(x_1,y_Sch_f,x_1,y_Sch_c,x_1,y_Landweber_c,...
    ratio_A_ms_h,ratio_V_h_V_I,'*')
grid on
axis([0 1.6 0.8 inf])
xlabel('$\frac{ \upsilon_\infty }{ \sqrt{ g h} }$ and $\frac{ A_{ms} }{ h }$ and $\frac{ A_{ms} }{ R_h }$')
ylabel('$\frac{ \upsilon_I }{ \upsilon_\infty }$ and $\frac{ \upsilon_h }{ \upsilon_I }$')
legend({'Curve of Sclichting, $\frac{ \upsilon_I }{ \upsilon_\infty }$',...
    'Curve of Sclichting, $\frac{ \upsilon_h }{ \upsilon_I } $',...
    'Curve of Landweber, $\frac{ \upsilon_h }{ \upsilon_I } $',...
    'Schlichting, $\frac{ \sqrt{A_{ms} } }{ h }$'},...
    'Interpreter','latex','Location','southwest')

figure('Name','Velocity in loss')
plot(V_inf,dV_V)
grid on
xlabel('$\upsilon_\infty$ (m/s)')
ylabel('\%')

figure('Name','Frictional resistance coefficient in deep water')
plot(Re,C_f)
grid on
xlabel('$Re$')
ylabel('$C_f$')

figure('Name','Residual resistance coefficient in deep water')
plot(Fr_L,C_r_10_3)
grid on
xlabel('$Fr_L ( \upsilon_\infty )$')
ylabel('$10^3 C_r$')

figure('Name','Residual resistance coefficient in deep water')
subplot(1,2,1);
plot(Re_V_I,C_f)
grid on
xlabel('$Re (\upsilon_I)$')
ylabel('$C_f$')
subplot(1,2,2);
plot(Fr_L,C_r_10_3)
grid on
xlabel('$Fr_L ( \upsilon_\infty )$')
ylabel('$10^3 C_r$')

figure('Name','Total resistance')
```

```
plot(V_inf,R_t,V_h,R_t_V_h,V_inf,R_f)
axis([0 1 0 inf])
grid on
xlabel('$\upsilon$ (m/s)')
ylabel('$R_t$ (N)')
legend({'$R_t$ (deep water)','$R_t$ (shallow water)',...
    '$R_f$ (deep water)'},'Interpreter','latex','Location','northwest')

figure('Name','Total resistance')
plot(Fr_L,R_t,Fr_L_V_h,R_t_V_h,Fr_L,R_f)
axis([0 0.15 0 inf])
grid on
xlabel('$Fr_L$')
ylabel('$R_t$ (N)')
legend({'$R_t$ (deep water)','$R_t$ (shallow water)',...
    '$R_f$ (deep water)'},'Interpreter','latex','Location','northwest')

%% Save variables
V_C2_Froude = V_inf;
V_C2_Schlichting = V_h;
R_t_C2_Froude = R_t;
R_t_C2_Schlichting = R_t_V_h;
ratio_A_ms_h_C2_Schlichting = ratio_A_ms_h;
ratio_V_h_V_I_C2_Schlichting = ratio_V_h_V_I;
V_inf_C2_Schlichting = V_inf;
dV_V_C2_Schlichting = dV_V;

save('V_C2_Froude.mat','V_C2_Froude')
save('V_C2_Schlichting.mat','V_C2_Schlichting')
save('R_t_C2_Froude.mat','R_t_C2_Froude')
save('R_t_C2_Schlichting.mat','R_t_C2_Schlichting')
save('ratio_A_ms_h_C2_Schlichting.mat','ratio_A_ms_h_C2_Schlichting')
save('ratio_V_h_V_I_C2_Schlichting.mat','ratio_V_h_V_I_C2_Schlichting')
save('V_inf_C2_Schlichting.mat','V_inf_C2_Schlichting')
save('dV_V_C2_Schlichting.mat','dV_V_C2_Schlichting')
```

C.2 Karpov's and Artjuskov's method

```
%% Evaluation of resistance of inland vessel using Karpov's and Artjuskov's method
% Evaluate the inland vessel by Karpov's and Artjuskov's method. For this
% ocasion we calculate the resistance of the vessel.
%-----------------------------------------------------------------------

%% Initial comands
% Always we check that the command windows and variables are clear, and
% windows are close too.
clc %Clear command windows
clear %Clear all variables
close all % Close all windows

%% Initial variables
% Only variables that can apply to this method are the gravity and
```

```
% kinematic viscosity at 20 C.
g = 9.81; %Gravity ( m / s^2 )
nu = 0.96895 * 10^(-6); %Kinematic viscosity ( m^2 / s )
rho = 101.77 * g; %Density of water ( kg / m^3 )

%--------------------------------------------------------------------------

% Also, the variables of the river.
Scale = 1 / 20; % Model scale.
h = 6 * Scale; % False depth of the tank ( m )

%--------------------------------------------------------------------------

% Finally, the characteristics of vessel river are
L_pp =     83.860 * Scale; %Length ( m )
B =        14.500 * Scale; %Beam ( m )
T =         3.200 * Scale; %Stern ( m )
S =      1630.500 * Scale^2; %Wetted surface area ( m^2 )
Nabla = 3504.400 * Scale^3; %Displacement volume ( m^3 )
A_ms =     45.906 * Scale^2; %Midship section area ( m^2 ) - Checked
B_0 =       3.500; %Towing tank width (m)

% Velocity of the inland vessel model ( m / s )
V_inf_1 = 0.01:0.01:0.92; %Velocity of the inland vessel model
V_inf = V_inf_1'; %Transpose of the velocity vector

%% Calculation of the resistance of vessel condition 2.
beta = A_ms / ( B * T ); %Midship section area coefficient
phi = Nabla / ( L_pp * B * T * beta ); %Prismatic coefficient
ratio_L_Nabla_3 = L_pp / Nabla^( 1 / 3 ); %Ratio between ship length and
% volume displacement
ratio_B_T = B / T; %Ratio between ship beam and draft
ratio_A_ms_h = sqrt( A_ms ) / h; %Ratio between midship section area of the
% vessel and depth
ratio_h_T = h / T; % Ratio between depth of the river and draft of the
%vessel model
ratio_B_B_0 = B / B_0; % Ratio between beam of the vessel model and the
% width of the river
j = length(V_inf); % Length of the velocity vector

% Diference of residual resistance coefficient and velocities defined by
% Artjuskov

Delta_C_r = ( 1 / 10^3 ) * ( - 0.10885912 + 0.023641012 * ratio_h_T - ...
    0.00248865 * ( ratio_h_T )^2 + 0.0000856328 * ( ratio_h_T )^3 -     ...
    0.02474568 * log( ratio_B_B_0 ) - 0.00476151 * ...
    ( log( ratio_B_B_0 ) )^2 ) / ( 1 - 0.03640844 * ratio_h_T + ...
    0.001560549 * ( ratio_h_T )^2 + 1.696914134 * log( ratio_B_B_0 ) ...
    + 0.943623478 * ( log( ratio_B_B_0 ) )^2 + 0.194816129 * ...
    ( log( ratio_B_B_0 ) )^3 );

V_V_1 = ( 1.201296612 - 0.24893659 * ratio_h_T + 0.753380571 * ...
    log( ratio_B_B_0 ) + 0.004502733 * ( log( ratio_B_B_0 ) )^2 ) / ( 1 ...
    - 0.21424821 * ratio_h_T - 0.00366378 * ( ratio_h_T )^2 + ...
```

```
    0.000121814 * ( ratio_h_T )^3 + 0.708479783 * log( ratio_B_B_0 ) );

%------------------------------------------------------------------------
% Variables that can calculate the residual resistance coefficient. These
% equations are the extrapolation of the Guldhammer and Harvald (1974) and
% is deteremininated by Georgagaki and Sorenson (2004).

A_0 = 1.35 - 0.23 * ratio_L_Nabla_3 + 0.012 * ratio_L_Nabla_3^2;
A_1 = 0.0011 * ratio_L_Nabla_3^( 9.1 );
N_1 = 2 * ratio_L_Nabla_3 - 3.7;
B_1 = 7 - 0.09 * ratio_L_Nabla_3^2;
B_2 = ( 5 * phi - 2.5 )^2;

%------------------------------------------------------------------------
% Looping variables. Initially are empty with zero.
Fr_L = zeros; % Length Froude number
Fr_h = zeros; % Depth Froude number
alpha_1 = zeros; % Alpha^* Karpov's diagrama
alpha_2 = zeros; % Alpha^{**} Karpov's diagrama
V_1 = zeros; % Velocity 1 by Karpov
V_2 = zeros; % Velocity 2 by Karpov
Re = zeros; % Reynolds number
C_f = zeros; % Frictional resistance coefficient

E = zeros; % Variable used for the calculation of the residual resistance
% coefficient.
B_3 = zeros; % Variable used for the calculation of the residual resistance
% coefficient.
G = zeros; % Variable used for the calculation of the residual resistance
% coefficient.
H = zeros; % Variable used for the calculation of the residual resistance
% coefficient.
K = zeros; % Variable used for the calculation of the residual resistance
% coefficient.
C_r_25_10_3 = zeros; % 10^3 Residual resistance coefficient if B/T = 2.5
C_r_10_3 = zeros; % 10^3 Residual resistance coefficient
C_r = zeros; % Residual resistance coefficient

R_f = zeros; % Frictional resistance
R_r = zeros; % Residuary resistance
R_t = zeros; % Total resistance

% Looping the calculation of the resistance in shallow waters
%------------------------------------------------------------------------
for k = 1:j
    Fr_h(k,1) = V_inf(k,1) / sqrt( g * h ); % Depth Froude number

    %--------------------------------------------------------------------

    % Alphas diagrams defined by Karpov

    % Alpha^*
    if Fr_h(k,1) < 0.2
        alpha_1(k,1) = 1;
```

```
    elseif ( Fr_h(k,1) >= 0.2 ) && ( Fr_h(k,1) <= 0.75 )
        alpha_1(k,1) = ( 1.072817327 - 2.95517983 * Fr_h(k,1) +...
            2.677257924 * ( Fr_h(k,1) )^2 - 0.34935866 * ( Fr_h(k,1) ...
            )^3 + 0.242040284 * log( ratio_h_T / 10 ) + 0.09728855 * ...
            ( log( ratio_h_T / 10 ) )^2 ) / ( 1 - 2.65876522 * Fr_h(k,1)...
            + 2.128572396 * ( Fr_h(k,1) )^2 + 0.196411142 * log( ...
            ratio_h_T / 10 ) + 0.05573344 * ( log( ratio_h_T / 10 ) )^2 ...
            - 0.01424796 * ( log( ratio_h_T / 10 ) )^3 );
        if alpha_1(k,1) > 1
            alpha_1(k,1) = 1;
        else
            alpha_1(k,1) = alpha_1(k,1);
        end
    elseif ( Fr_h(k,1) > 0.75 ) && ( Fr_h(k,1) < 0.9 )
        alpha_1(k,1) = ( 1.016019336 + 12.53814509 * log( Fr_h(k,1) ) + ...
            53.26949464 * ( log( Fr_h(k,1) ) )^2 + 74.73282869 * ( ...
            log( Fr_h(k,1) ) )^3 + 0.001376743 * log( ratio_h_T / 10 ) ...
            ) / ( 1 + 12.31125171 * log( Fr_h(k,1) ) + 52.09394682 * ...
            ( log ( Fr_h(k,1) ) )^2 + 72.79361228 * ( log( Fr_h(k,1) ) ...
            )^3 - 0.00395828 * log( ratio_h_T / 10 ) );
    else
        alpha_1(k,1) = 1;
    end

    % Alpha^{**}
    alpha_2(k,1) = ( 0.951498465 + 0.090322144 * log( ratio_h_T ) - ...
        0.02585333 * ( log( ratio_h_T ) )^2 + 0.003378671 * ( log( ...
        ratio_h_T ) )^3 - 2.05546622 * Fr_h(k,1) + 1.088478007 * ( ...
        Fr_h(k,1) )^2 ) / ( 1 + 0.03275693 * log( ratio_h_T ) - ...
        0.0036447 * ( log( ratio_h_T ) )^2 - 2.17156612 * Fr_h(k,1) + ...
        1.407458972 * ( Fr_h(k,1) )^2 - 0.18634398 * ( Fr_h(k,1) )^3 );

    if alpha_2(k,1) > 1
        alpha_2(k,1) = 1;
    else
        alpha_2(k,1) = alpha_2(k,1);
        if Fr_h <= 0.2
            alpha_2(k,1) = ( 0.951498465 + 0.090322144 * log( ratio_h_T ...
                ) - 0.02585333 * ( log( ratio_h_T ) )^2 + 0.003378671 ...
                * ( log( ratio_h_T ) )^3 - 2.05546622 * 0.2 + ...
                1.088478007 * 0.2^2 ) / ( 1 + 0.03275693 * log( ...
                ratio_h_T ) - 0.0036447 * ( log( ratio_h_T ) )^2 - ...
                2.17156612 * 0.2 + 1.407458972 * 0.2^2 - 0.18634398 ...
                * 0.2^3 );
        else
            alpha_2(k,1) = alpha_2(k,1);
        end
    end

    % Calculation of the velocities

    V_1(k,1) = V_inf(k,1) / alpha_1(k,1);
    V_2(k,1) = V_inf(k,1) / alpha_2(k,1);
```

```
    Re(k,1) = L_pp * V_1(k,1) / nu; % Reynolds number
    C_f(k,1) = 0.075 / ( log10( Re(k,1) ) - 2 )^2; % Frictional resistance
    % coefficient

    % Equation for obtain data for residuary resistent coefficient
    % obtained by Harvald graphic and improved by Georgakaki and Sorenson

    Fr_L(k,1) = V_2(k,1) / sqrt( g * L_pp ); %Length Froude number
    if Fr_L(k,1) <= 0.15 % C_r is constant
        E(k,1) = ( A_0 + 1.5 * 0.15^( 1.8 ) + A_1 * 0.15^( N_1 ) ) * ...
            ( 0.98 + 2.5 / ( ratio_L_Nabla_3 - 2 )^4 ) + ...
            ( ratio_L_Nabla_3 - 5 )^4 * ( 0.15 - 0.1 )^4;
        B_3(k,1) = ( 600 * ( 0.15 - 0.315 )^2 + 1 )^( 1.5 );
        G(k,1) = B_1 * B_2 / B_3(k,1);
        H(k,1) = exp( 80 * ( 0.15 - ( 0.04 + 0.59 * phi ) - ...
            ( 0.015 * ( ratio_L_Nabla_3 - 5 ) ) ) );
        K(k,1) = 180 * 0.15^( 3.7 ) * exp( 20 * phi - 16 );
        if ratio_B_T == 2.5
            C_r_25_10_3(k,1) = E(k,1) + G(k,1) + H(k,1) + K(k,1);
            C_r_10_3(k,1) = C_r_25_10_3(k,1);
            C_r(k,1) = C_r_10_3(k,1) / 10^3; % Residuary resistance coef.
        else
            C_r_25_10_3(k,1) = E(k,1) + G(k,1) + H(k,1) + K(k,1);
            C_r_10_3(k,1) = C_r_25_10_3(k,1) + 0.16 * ( ratio_B_T - 2.5 );
            C_r(k,1) = C_r_10_3(k,1) / 10^3; % Residuary resistance coef.
        end
    else % C_r is a function.
        E(k,1) = ( A_0 + 1.5 * Fr_L(k,1)^( 1.8 ) + A_1 * Fr_L(k,1)^(...
            N_1 ) ) * ( 0.98 + 2.5 / ( ratio_L_Nabla_3 - 2 )^4 ) + ...
            ( ratio_L_Nabla_3 - 5 )^4 * ( Fr_L(k,1) - 0.1 )^4;
        B_3(k,1) = ( 600 * ( Fr_L(k,1) - 0.315 )^2 + 1 )^( 1.5 );
        G(k,1) = B_1 * B_2 / B_3(k,1);
        H(k,1) = exp( 80 * ( Fr_L(k,1) - ( 0.04 + 0.59 * phi ) - ...
            ( 0.015 * ( ratio_L_Nabla_3 - 5 ) ) ) );
        K(k,1) = 180 * Fr_L(k,1)^( 3.7 ) * exp( 20 * phi - 16 );
        if ratio_B_T == 2.5
            C_r_25_10_3(k,1) = E(k,1) + G(k,1) + H(k,1) + K(k,1);
            C_r_10_3(k,1) = C_r_25_10_3(k,1);
            C_r(k,1) = C_r_10_3(k,1) / 10^3; % Residuary resistance coef.
        else
            C_r_25_10_3(k,1) = E(k,1) + G(k,1) + H(k,1) + K(k,1);
            C_r_10_3(k,1) = C_r_25_10_3(k,1) + 0.16 * ( ratio_B_T - 2.5 );
            C_r(k,1) = C_r_10_3(k,1) / 10^3; % Residuary resistance coef.
        end
    end

    R_f(k,1) = 1 / 2 * rho * S * C_f(k,1) * ( V_1(k,1) )^2;
    R_r(k,1) = 1 / 2 * rho * S * ( C_r(k,1) * ( 1/ V_V_1 )^2 + ...
        Delta_C_r ) * ( V_2(k,1) )^2;
    R_t(k,1) = R_f(k,1) + R_r(k,1);
end

alphas = [ Fr_h alpha_1 alpha_2 ];
V = [ V_inf V_1 V_2 ];
```

```
%% Displaying in command window
disp('Evaluation of resistance of inland vessel 2700 TDW using method of Karpov and
    Arjuskov')
disp('---------------------------------------------------------------------------------')

disp('Scale')
disp(Scale)

disp('Length of waterline - L_pp (m)')
disp(L_pp)

disp('Beam - B (m)')
disp(B)

disp('Draft - T (m)')
disp(T)

disp('Wetted surface of the hull - S (m^2)')
disp(S)

disp('Displacement - Nabla (m^3)')
disp(Nabla)

disp('Midship section area - A_ms (m^2)')
disp(A_ms)

disp('Towing tank width - B_0 (m)')
disp(B_0)

disp('Midship section area coefficient - beta')
disp(beta)

disp('Prismatic coefficient - phi')
disp(phi)

disp('Ratio between model length and volume displacement - L_pp / Nabla^3')
disp(ratio_L_Nabla_3)

disp('Ratio between model beam and draft - B / T')
disp(ratio_B_T)

disp('Ratio between Midship section area and depth - sqrt(A_ms) / h')
disp(ratio_A_ms_h)

disp('Ratio between depth and draft - h / T')
disp(ratio_h_T)

disp('Ratio between beam and width - B / B_0')
disp(ratio_B_B_0)

disp('Changes in residual resistance coefficient - Delta C_r')
disp(Delta_C_r)

```

```
disp('Velocities - V / V_1')
disp(V_V_1)

disp('Alphas diagrams by Karvop (m/s)')
disp('      Fr_h      alpha^*     alpha^**')
disp(alphas)

disp('Velocity (m/s)')
disp('      V_inf       V_1        V_2')
disp(V)

%% Graphics

set (0,'defaulttextinterpreter','Latex');

figure('Name','Alpha* diagram by Karpov')
plot(Fr_h,alpha_1)
grid on
xlabel('$Fr_h ( \upsilon_{ \infty } )$')
ylabel('$\alpha^*$')

figure('Name','Alpha** diagram by Karpov')
plot(Fr_h,alpha_2)
grid on
xlabel('$Fr_h ( \upsilon_{ \infty } )$')
ylabel('$\alpha^{**}$')

figure('Name','Alpha* and Alpha** diagram by Karpov')
subplot(1,2,1);
plot(Fr_h,alpha_1)
title('$\alpha^*$')
grid on
xlabel('$Fr_h ( \upsilon_{ \infty } )$')
ylabel('$\alpha^*$')
subplot(1,2,2);
plot(Fr_h,alpha_2)
title('$\alpha^{**}$')
grid on
axis([-inf 0.6 0.9 1 ])
xlabel('$Fr_h ( \upsilon_{ \infty } )$')
ylabel('$\alpha^{**}$')

figure('Name','Frictional resistance coefficient')
plot(Re,C_f)
grid on
xlabel('$Re ( \upsilon_1 )$')
ylabel('$C_f$')

figure('Name','Residual resistance coefficient')
plot(Fr_L,C_r_10_3)
grid on
xlabel('$Fr_L ( \upsilon_2 )$')
ylabel('$10^3 C_r$')
```

```
figure('Name','Resistance coefficients')
subplot(1,2,1);
plot(Re,C_f)
title('$C_f$')
grid on
xlabel('$Re ( \upsilon_1 )$')
ylabel('$C_f$')
subplot(1,2,2);
plot(Fr_L,C_r_10_3)
title('$C_r$')
grid on
xlabel('$Fr_L ( \upsilon_2 )$')
ylabel('$10^3 C_r$')

figure('Name','Total resistance')
plot(V_inf,R_t,V_inf,R_f)
grid on
xlabel('$\upsilon$ (m/s)')
ylabel('$R_t$ (N)')
legend({'$R_t$','$R_f$'},...
    'Interpreter','latex','Location','northwest')

figure('Name','Total resistance')
plot(Fr_L,R_t)
grid on
xlabel('$Fr_L$')
ylabel('$R_t$ (N)')

%% Save variables
V_C2_Karpov_Arjuskov = V_inf;
R_t_C2_Karpov_Arjuskov = R_t;

save('V_C2_Karpov_Arjuskov.mat','V_C2_Karpov_Arjuskov')
save('R_t_C2_Karpov_Arjuskov.mat','R_t_C2_Karpov_Arjuskov')
```

C.3 Total prism layer calculation

```
%% Total prism layer calculation applying to STAR-CCM+
% In this algorithm is calculated the total prism layer.
% Reynolds number, frictional resistance coefficient, y+, scale factor and
% number of layers are taken account.

%%
clc % Clear command window
clear % Clear all variables
close all % Close all open windows

%% Calculation of the hull thickness distance

% Reynolds number and frictional resistance coefficient
L = 4.193 ; % Length of the inland vessel model
u = 0.576 ; % Velocity
```

```
nu = 0.96895 * 10^( - 6 ) ; %Kinematic viscosity

Re = u * L / nu ; % Reynolds number
C_f = 0.075 / ( log10( Re ) - 2 )^2 ; % Frictional resistance coefficient

y_plus = 1; %Choosing y+

% Calculate first boundary layer length
y = y_plus * L / ( Re * sqrt( C_f / 2 ) ) ;
SF = 1.44; %Scale Factor
n_l = 10; %Number of layers
A = zeros(n_l,1); % Create matrix zeros of every length of number of layers

% Total tickness prism layer calculation
for n_L = 1:n_l % Number of layers looping from first to last layer
    if n_L == 1 % Condition if the prism layer is equal to the first
        A(n_L,:) = y ;
    else % Condition if the prism layer is different to the first
        A(n_L,:) = A(n_L-1,:) * SF;
    end
end

Y = sum(A); %Total tickness prism layer

%% Flat-Plate boundary layer on bottom for volume of domain
L_ref = 6.76; %Wall bottom length ( m )
rho = 997; %Density of the water ( kg / m^3 )

Re_x = u * L_ref / nu; %Reynolds number of wall bottom
C_f_x = 0.026 / Re_x^( 1 / 7); %Frictional coefficient of wall bottom
tau_wall = C_f_x * rho * u^2 / 2; %Wall shear stress (Pa)
u_frict = sqrt( tau_wall / rho ); %Frictional velocity of the wall

y_plus_bottom = 30; % y+ of the wall bottom
y_bottom = y_plus_bottom * nu / u_frict; %Distance of the wall bottom thickness
n_l_bottom = 4; %Number of layers on bottom
SF_bottom = 1.2; %Scale factor
B = zeros(n_l_bottom,1);%Create matrix zeros of every length of number of layers

% Total tickness prism layer calculation
for n_L_bottom = 1:n_l_bottom
    if n_L_bottom == 1
        B(n_L_bottom,:) = y_bottom;
    else
        B(n_L_bottom,:) = B(n_L_bottom-1,:) * SF_bottom;
    end
end

Y_bottom = sum(B); %Total tickness prism layer

%% Displaying results
disp('Calculation of Boundary layer of 2700 TDW')
disp('----------------------------------------------------------------')
disp('Calculation for hull')
```

```

disp('Reynolds number')
disp(Re)

disp('Frictional resistance coefficient')
disp(C_f)

disp('y+')
disp(y_plus)

disp('First layer tickness (m)')
disp(y)

disp('Number of layers')
disp(n_l)

disp('Scale factor')
disp(SF)

disp('Tickness layers (m)')
disp(A)

disp('Total tickness (m)')
disp(Y)

disp('---------------------------------------------------------------------------')
disp('Calculation for IPT towing tank bottom boundary')

disp('Reynolds number')
disp(Re_x)

disp('Frictional resistance coefficient')
disp(C_f_x)

disp('Wall shear stress (Pa)')
disp(tau_wall)

disp('Frictional velocity of the wall (m/s)')
disp(u_frict)

disp('y+')
disp(y_plus_bottom)

disp('First layer tickness (m)')
disp(y_bottom)

disp('Number of layers')
disp(n_l_bottom)

disp('Scale factor')
disp(SF_bottom)

disp('Tickness layers (m)')
disp(B)
```

```
disp('Total tickness (m)')
disp(Y_bottom)
```